Design, Construction and Testing of an Adaptive Pendulum Tuned Mass Damper

By

Richard Lourenco

A thesis

presented to the University of Waterloo

in fulfillment of the

thesis requirement for the degree of

Master of Applied Science

in

Mechanical Engineering

Waterloo, Ontario, Canada, 2011

Author’s Declaration

I hereby declare that I am the sole author of this thesis. This is a true copy of the thesis, including any required final revisions, as accepted by my examiners.

I understand that my thesis may be made electronically available to the public.

Abstract

The objective of this thesis is to describe the design, construction, implementation and performance of a prototype adaptive pendulum tuned mass damper (APTMD). Furthermore the thesis aims at demonstrating the performance improvements obtained when the tuned mass damper (TMD) parameters are optimized. The study considers the effect of adjusting the APTMD tuned frequency and damping ratio on a two storey test structure subjected to broadband and narrowband excitation.

An analytical model of the APTMD for a single-degree-of-freedom (SDOF) structure is used to demonstrate the performance improvements when the APTMD parameters are optimized. The optimized model considers the effects of adjusting the frequency ratio, damping ratio, and mass ratio of the combined system to reduce the maximum deflection when the structure is subjected to a harmonic excitation force. The analytical model is used to simulate the optimal performance of the APTMD system.

The experimental APTMD is capable of identifying the structural vibration modes in real time and tuning to the desired mode. The structural vibration modes are identified by calculating the windowed power spectral density of the structure's acceleration, followed by peak-picking algorithm to identify the modal frequencies. Tuning is performed by moving the pivot location of the pendulum arm via a tuning frame along a set of rails. The design also allows for changes in the external dampening force. An adjustable damper is attached to the pendulum mass to allow for control of the APTMD damping ratio.

A prototype of the APTMD is built and tested in a modal testing setup. The test structure is a two-storey model of a building structure. The structure is excited using a shaker fixed to the lower storey of the structure. The performance of the APTMD under broadband and narrowband excitation is examined for various tuning and damping parameters. The performance of the APTMD system under optimally tuned and detuned conditions is investigated.

The results of the experimental studies demonstrate the importance of optimizing the TMD tuned frequency and damping ratio to reduce structural vibrations. Since the APTMD is designed to

autonomously update both parameters, it is an effective tool in mitigating structural vibrations where user interaction is either difficult or expensive. Further study on the performance of a prototype APTMD applied to a large scale structure is required before implementation on full-scale structures.

Acknowledgements

I would like to thank my supervisors, Dr. Sriram Narasimhan and Dr. Serhiy Yarusevych for their technical guidance through my M.A.Sc studies.

To the technical staff at the University of Waterloo, specifically Juan and George who operate the materials shop, and Quoi and John who supervise the engineering machine shop. Your assistance was vital in the fabrication of the prototypes.

In addition I would like to express my appreciation to the members of my workgroup, specifically Aaron Roffel and Sina Kheirkhah.

I would like to thank my parents who sacrificed their time and efforts to support me along the way. Thank you to my friends who kept me sane.

Finally, thank you to the Ontario Centers for Excellence and National Sciences and Engineering Research Council of Canada (NSERC) for providing the financial support. I would also like to thank Rowan Williams Davies & Irwin and Greater Toronto Airports Authority for their financial support.

Dedication

To Dr. Sriram Narasimhan who offered his technical experience on a daily basis, a smile, and the news every Monday and Friday.

Table of Contents

List of Figures

List of Tables

Nomenclature

ATMD	active tuned mass damper
APTMD	active pendulum tuned mass damper
b	structure viscous damping coefficient [N/(m/s)]
c	pendulum friction torque coefficient [N/(rad/ms)]
d	pendulum external damper viscous damping coefficient [N/(m/s)]
FFT	Fast Fourier Transform
FRF	frequency response function
$F(t)$	structure excitation force [N]
F_0	magnitude structure excitation force [N]
F_S	sampling frequency [Hz]
k	structure stiffness constant [N/m]
M	structure mass [kg]
m	pendulum mass [kg]
$\bar{m}$	mass ratio [kg]
L	pendulum length [m]
PPS	pulses-per-second
PSD	power spectral density
PTMD	pendulum tuned mass damper
RMS	root mean square
SATMD	semi-active tuned mass damper
SDOF	single-degree-of-freedom
$S(f)$	power spectral density estimate
TMD	tuned mass damper
X	structure displacement amplification factor
$x(t)$	structure horizontal displacement [m]
$\dot{x}(t)$	structure horizontal velocity [m]
$\ddot{x}(t)$	structure horizontal acceleration [m]
Y	pendulum mass displacement amplification factor

$y(t)$	pendulum mass horizontal displacement [m]
$\dot{y}(t)$	pendulum mass horizontal displacement [m]
$\ddot{y}(t)$	pendulum mass horizontal acceleration [m]
α	excitation frequency ratio
β	tuned frequency ratio
δ_1	phase difference [rad]
$\theta(t)$	pendulum angular displacement [rad]
$\dot{\theta}(t)$	pendulum angular velocity [$\mathrm{rad/s}$]
$\ddot{\theta}(t)$	pendulum angular acceleration [$\mathrm{rad/s^2}$]
ξ	structure damping ratio
ξ_d	PTMD damping ratio
ξ_e	effective PTMD damping ratio
ω	structure natural frequency [rad/s]
ω_d	PTMD natural frequency [rad/s]
Δ	histogram bin width [Hz]
ΔE	dissipation energy [J]
Ω	excitation frequency [Hz]

Chapter 1: Introduction

1.1 Background and Motivation

Urbanization, coupled with modern design and construction technologies, has resulted in taller and lighter structures. As an example, the world's tallest man-made structure the Burj Kalifa tower stands a remarkable 828 m from its base with an estimated weight in excess of 110,000 tonnes (Baker et al. 2007). One of the trade-offs of building to larger heights is the susceptibility to vibration due to the inherent flexibility of the structure. When excited by environmental dynamic loads, such as wind, this could result in large amplitude motion at the top of the structure.

There are two significant negative effects from structural vibrations on building structures (Sain et al. 2007). The first effect is the long term fatigue to structures due to the periodic dynamic loading. It is well established that the leading cause of material failure in building structures is due to fatigue. Building materials, such as metals, subjected to periodic loadings can develop fractures (Sain at al. 2007). The presence of a fracture jeopardizes the structural integrity, and may inevitably lead to structural failure. Although the likelihood of failure in modern building structures is very low, the deterioration from fatigue affects the structural stiffness. A weakened structure will exhibit less structural stiffness which will result in larger amplitudes at the top of the structure when the structure is excited. Coincidentally, larger top floor displacement amplitudes yield greater stress on the structure. Hence the deterioration rate of the structural members will increase over time (Foreman et al. 1967). To account for damage caused by structural vibrations, the structure will require maintenance or reconstruction; both of which represent significant financial costs.

The second effect is the human perception from the induced motion. Humans are very perceptive to even minor vibrations. Sensitive people can perceive accelerations as low as 0.05g (Kareem et al. 2007). Between 0.1g and 0.25g structural motions may affect an individual's ability to work, and over the long term it may lead to motion sickness (Kareem et al. 2007). Considering that the stress and strain from top-floor deflections are unlikely to lead to structural failure in modern buildings, serviceability considerations focus on the human perception and ability to perform the

individual's tasks effectively, rather than the strength of a structure. Buildings are, after all, built for humans to occupy, be it a living space or a work space.

The desire then is to mitigate structural vibrations in building structures. The control of structural vibrations can be achieved by various methods (Mendis et al. 2007). The amplitude and frequency of structural vibrations can be manipulated by modifying the structural mass, stiffness, shape and damping. In the case of wind induced vibrations, changing the geometry of the structure can reduce the aerodynamic forces; hence, lowering the amplitude of structural vibrations. Adding additional bracing will also stiffen the structure and reduce building sway (Mendis et al. 2007). Alternatively, the addition of passive or active stabilizing forces on the structure from an external dampening device can also be implemented to mitigate the effect of structural vibrations (Gerges and Vickery 2005). One such example is the tuned mass dampener (TMD). TMDs operate by providing additional dampening to the building structure. They are advantageous over conventional design methods-especially for taller lighter construction since they are economical and can be implemented as an add-on to existing or new structures. Real structures may employ a combination of vibration suppression methods. An example of such a structure is the Taipei 101, the second tallest man-made structure in the world. The skyscraper, which is shown in Figure 1, stands 508 m above ground level in a region which experiences strong winds, ground vibrations, and typhoons (Tamboli et al. 2008). Design elements of the structure include three TMDs, one of which is a pendulum TMD and the largest TMD in the world at 660 tonnes (Tamboli et al. 2008). The architectural design of the structure also incorporates saw-tooth corners which reduce the effect of vortex-shedding, a major contributor to building sway.

A TMD, or harmonic absorber, is a passive system (although variants include active elements) which can be modelled with a mass, a spring, and a damper. The TMD is tuned to a ratio of the structures natural frequency (or another modal frequency). When the structure is excited at the tuned frequency, the damper resonates out-of-phase with the point of connection to the structure (Setareh at al. 2006). Vibration energy is dissipated from the structure via dissipative elements (dampers) that are a part of the TMD system. Although there are several different implementations to the TMD design, the four most common types of TMDs used are translational TMDs, pendulum TMDs (PTMD), semi-active TMDs (SATMD), and active TMDs

(ATMD) (Conner 2003). The concept of the TMD is not by any measure novel, and its performance is well documented (e.g., Gerges 2003, Chang 2010, and Mendis 2007). It was first developed by Herman Frahm in 1909 to reduce the vibration at the hull of ships (Conner 2003). Today it is commonly used in buildings, automobiles, and virtually any system where vibration suppression is desired.

(a) (b)

Figure 1: (a) Taipei 101 (Powell 2007) (b) Taipei 101 PTMD (du Plessis, 2010)

Despite its widespread use, conventional TMD designs have several major drawbacks. Specifically the performance of any passive TMD is reliant on the selected modal frequency of the structure (e.g. Clark 1988, Chang et al. 2010, and Setareh 2002). This frequency is generally attained using one of two methods (Roffel et al. 2011). The first is to model the response of the structure. The projected mass and stiffness of the structure can be estimated from its architectural drawings and an estimate of the harmonic modes of the structure is developed. This method is referred to as forecasting (Roffel et al. 2011). However, the major drawback is that the model provides only a rough approximation of the structural response, and the discrepancies between the estimated and actual (as-built) modal properties of the structure may deteriorate the performance of the TMDs significantly (Roffel et al. 2011).

The emergence of more sophisticated vibration measurement systems has led to the development of the second method, which involves the determination of the desired tuning frequency during its installation (Roffel et al. 2011). With this method vibration measurements of the structure are recorded and used to determine its major harmonic modes. The test is performed with the TMD damper restrained and is followed by a pull test, where the TMD mass is pulled to one side and released. This method is considerably more accurate than forecasting. However, the added complexity of providing structural vibration measurements and analysis is an additional cost in both time and money. Furthermore, due to changes in the operating environment the TMD may become detuned (Roffel at al. 2011). Examples of these changes include structural deterioration, additional construction of the structure, or any additional dynamic loading via machine or vehicle. To remedy these shortcomings SATMD or multiple TMD systems have been developed (Setareh, 2007, Nagarajaiah, 2007, and Lin, 2001). These systems account for small variations in the structural stiffness. Although these systems are certainly more robust against detuning, they still require periodic maintenance.

1.2 Objectives and Scope

The main objectives of this thesis are the following:

- Demonstrate the importance of properly tuning TMD parameters to reduce the amplitude of vibration for an excited structure
- Describe the design, construction, implementation and performance of a prototype adaptive pendulum tuned mass damper (APTMD). The prototype is designed to identify and update PTMD tuning parameters autonomously.

The scope of this work will be limited by the TMD tuning parameters, the selected test structure, and the excitation force applied to the test structure. The TMD tuning parameters considered will be the natural frequency and damping ratio of the APTMD. The natural frequency is adjusted by changing the length of the pendulum. The damping ratio is adjusted by changing the damping coefficient of an external damper applied to the pendulum mass. To evaluate the performance dependence of TMD parameters, a single-degree-of-freedom (SDOF) structure model will be used. Furthermore, a two-storey test structure is constructed to evaluate the performance of the

prototype APTMD. Both the SDOF model and two-storey test structure is an ideal representation of a real structure. The simplified structures are excited by narrow or broadband harmonic excitation forces to demonstrate the autonomous tuning capabilities of the APTMD.

1.3 Preface

The thesis is organized as follows:

Chapter 2 contains a literature review of TMD designs and their implementation. This chapter will focus primarily on passive, active, and semi-active TMD designs and draw performance comparisons of different design variants.

Chapter 3 provides an analytical model of a PTMD attached to a SDOF structure. An analytical model of the combined structure-PTMD system is derived. The effects of adjusting the PTMD tuned frequency ratio, PTMD damping ratio, and mass ratio on the simulated SDOF structure are observed. An optimal PTMD system based on the experiment setup is obtained.

Chapter 4 provides a detailed description of the test structure and testing apparatus. The design of a prototype APTMD is presented. The design consists of the dampening assembly which is necessary to achieve the parameter adjustments necessary to counteract the changes in the structure and environmental conditions. A description of how the APTMD is automated for the experiments is provided.

In Chapter 5 the performance of the prototype APTMD is analyzed and observations are provided. Experiments are conducted on the APTMD using broadband and narrowband excitations.

In Chapter 6 conclusions are made based on the design and performance of the APTMD design. Future work on a full scale prototype is discussed.

Chapter 2: Literature Review

2.1 Operating Principle of TMD Systems

A TMD system is a structural control device used to reduce the amplitude of structural and mechanical vibrations in buildings and mechanical systems. Their use in structures is primarily to prevent discomfort of the structure's occupants and, in some cases, to augment the fatigue life (Kareem et al. 2007). There are several different topologies of TMD systems. The simplest topology is the passive TMD which contains a mass, a spring, and a dissipative energy device such as a damper (Conner 2003). When the TMD is tuned close to the structural mode of interest, the TMD will resonate out-of-phase with the structure, and the resulting vibration energy will be dissipated by the damper to the environment as heat. The selection of TMD system parameters to match the damper frequency with the natural frequency of the connecting structure is the act of 'tuning' the TMD system. Therefore, by properly tuning the TMD to the fundamental excitation modes of the attached structure, the TMD damper will dissipate a significant amount of structural vibration.

The result of tuning a TMD to a structure's dominant modal frequency is a reduction in energy at the tuned frequency. Away from the peak frequency, the response may increase, effectively turning a single lightly damped mode into two coupled and highly damped modes (Conner 2003). The use of TMD systems is particularly useful in structures such as tall buildings or suspension bridges, where resonant conditions coincide with external excitation frequencies.

The design of a TMD system is generally constructed as an optimization problem (Conner 2003). Optimization is the determination of system parameters which maximize the performance based on a performance criterion (also known as an objective function). The desire is to develop closed form expressions relating the damping ratio, mass ratio (ratio of the TMD mass to the structural mass), and tuned frequency ratio (ratio of the tuned frequency and the structure`s natural frequency). The performance criterion is selected based on a desirable response level for the structure (for example the roof acceleration) when it is excited. Practical considerations must be given with regard to the selection of the mass ratio. For large scale structures, the structural mass can exceed 100,000 tonnes (Tamboli et al. 2008). Since the mass ratio is generally within a

fraction of the total structure mass, the ability to contain such a mass within the structure becomes a practical concern (Conner 2003). As a result, mass ratios of TMD assemblies for large building structures typically fall below 1%.

The development and utilization of different TMD system topologies is to overcome the inherent performance limitations of passive TMD systems. The performance limitations may be based on the robustness to changes in the structural stiffness, the spatial limitations within the structure, or the cost and lifespan of the TMD system. The subsequent sections within this chapter focus on different system topologies.

2.2 Passive TMD Systems

Passive systems are characterized by the absence of an external source of energy. As a result overall system stability is usually not a concern. A passive TMD system is any TMD topology which does not contain any active element, such as an actuator. As a result these systems are entirely mechanical.

A limitation shared by all passive TMD systems is its lack of robustness to detuning conditions (Setareh et al. 2006). Outside of the narrow tuned frequency band of the TMD, the effectiveness of the TMD at reducing structural vibration is diminished. Even small deviations from the optimal tuning frequency can deteriorate the performance significantly. As a result the effectiveness of a passive TMD system is reliant on the accuracy of its initial tuning, and whether there is any structural detuning subsequently (Roffel et al. 2011).

Despite this significant limitation, passive TMD systems are still used because they are relatively inexpensive systems, which perform well when properly tuned (Kareem et al. 2007). Furthermore the absence of an external actuator or energy source means that there are no additional operational costs once the system is installed. The two most common types of passive tuned mass dampers are translational TMDs and PTMDs (Conner 2003).

2.2.1 Translational TMD Systems

Translational TMD can be either unidirectional or bidirectional systems (Conner 2003). In unidirectional systems the motion of the TMD mass is restricted to a single direction, often by placing the mass on a set of rails or roller bearings, as depicted in Figure 2. In bidirectional systems, the mass can move along both coordinate axes. In either topology a set of springs and dampers are placed between the TMD mass and the supporting structure which is fixed to the structure.

Translational TMD systems have been implemented in large scale structures for over 40 years (Kareem et al. 2007). Examples of structures containing translation TMD systems include the Washington National Airport Tower, the John Hancock Tower, and the Chiba Port Tower.

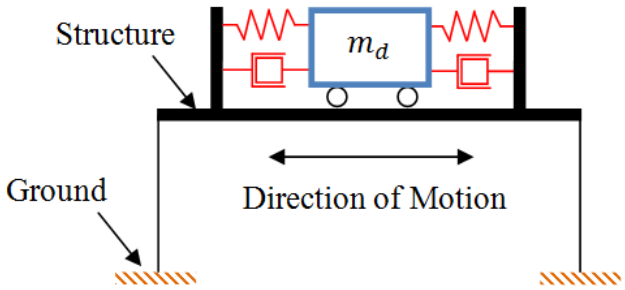

Figure 2: Schematic of a unidirectional translational TMD

2.2.2 PTMD Systems

PTMDs replace the translational spring and damper system with a pendulum, which consists of a mass supported by a cable which pivots about a point, as illustrated in Figure 3. They are commonly modelled as a simple pendulum. For small angular oscillations they will behave similarly to a translational TMD and can be modelled identically with an equivalent stiffness and equivalent damping ratio. Hence, the design methodology for both the translational TMD system and PTMD systems are identical (Conner 2003).

A major motivating factor for using a PTMD system over an equivalent translational TMD system is the absence of any bearings to support the TMD mass (Conner et al. 2003). The bearing support structure used in the translational TMD assembly is expensive and susceptible to wear over the lifespan of the TMD system. As a result PTMD designs can be less expensive to

manufacture and last longer. Nearly 50% of structures in Japan that use TMD systems utilize PTMD systems (Kareem et al. 2007). Examples include Crystal Tower in Osaka, Higashimyama Sky Tower in Nagoya, and Taipei 101 in Taipei (Conner 2003).

Studies on the use of PTMD systems generally focus on the optimization of PTMD design parameters to reduce excessive lateral deflections in structures. Gerges and Vickery (2003) utilized a non-linear wire rope spring PTMD system in an experimental case study, concluding that their performance approaches optimal linear TMD designs while providing smaller relative displacements for lower mass ratios. Setareh et al. (2006) presented optimization algorithms for a PTMD system induced by pedestrian loading.

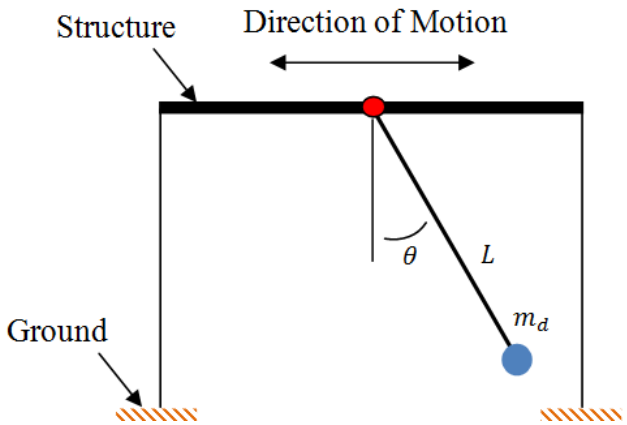

Figure 3: Schematic of a PTMD

2.3 ATMD Systems

Active systems contain an external energy source, often in the form of an actuator. In comparison to passive systems, which operate without an energy source and utilize an open loop control topology, active systems utilize sensors to measure system conditions and employ a closed loop control topology.

An ATMD system, as shown in Figure 4, contains an actuator which drives the motion of either the TMD mass or an auxiliary mass connected to the TMD mass. By actively controlling the motion of an external mass, the ATMD can control the forces exerted on the structure. There are two advantages in this design. First, the performance of an ATMD system will outperform an equivalent passive TMD under detuning conditions, since any detuning is compensated by

feedback control (e.g. Nishimura et al. 1992, Nagashima 2001). Secondly, an ATMD system is capable of optimizing its transient performance. This is particularly useful for impact loads, such as earthquake loads (Conner 2003). As a result ATMD systems have been implemented to reduce the lateral response of structures when induced by earthquake loads. For, example the Kyobashi Seiwa Building in Tokyo, Japan contains two ATMDs to mitigate structural vibration induced by frequent earthquakes (Spencer and Sain 1997). The installed system reduces the lateral displacement by approximately 67%.

Several studies have been performed on the use and performance of ATMDs. These studies generally focus on an optimal control algorithm used to improve the ATMDs performance. Li et al. (2010) successfully applied an ATMD model to control the torsional and translational response of a 2-DOF asymmetric structure model. Nishimura et al. (1992) compared the performance of an ATMD using a set of optimized parameter equations to a passive TMD system, observing an 80% improvement at the peak frequency. Nagashima (2001) presented an optimal displacement feedback control law for an ATMD system on a SDOF system.

Although ATMDs can outperform their passive counterparts, they have some drawbacks. The added design, manufacturing, and instrumentation complexity results in significantly higher financial costs over passive systems. Furthermore, the addition of an actuator significantly increases the energy requirements of the system. To reduce energy demands, active systems can be converted into hybrid systems (Conner 2003). In hybrid systems the ATMD acts as a passive system under typical loading conditions. Once the structure reaches a certain threshold, the active system is turned on. An example of a hybrid system is the Ando Nishikicho Building in Tokyo, Japan, which uses a hybrid system containing an 18 tonne passive TMD and two auxiliary actuated masses weighing a combined 3.6 tonnes (Conner 2003). A conceptual diagram of the system is shown in Figure 5.

2.4 SATMD Systems

ATMD systems provide improved vibration suppression performance at the cost of added complexity, maintenance, and energy requirements (Conner 2003). As a result, active systems are usually employed in structures that are exposed to significant dynamic loading. Passive TMD

systems are fairly simple systems which provide excellent vibration suppression when accurately tuned and when the structure is excited by narrowband dynamic loading (Setareh 2006). Their lack of robustness to multiple-frequency narrowband excitations and structural detuning limit their performance.

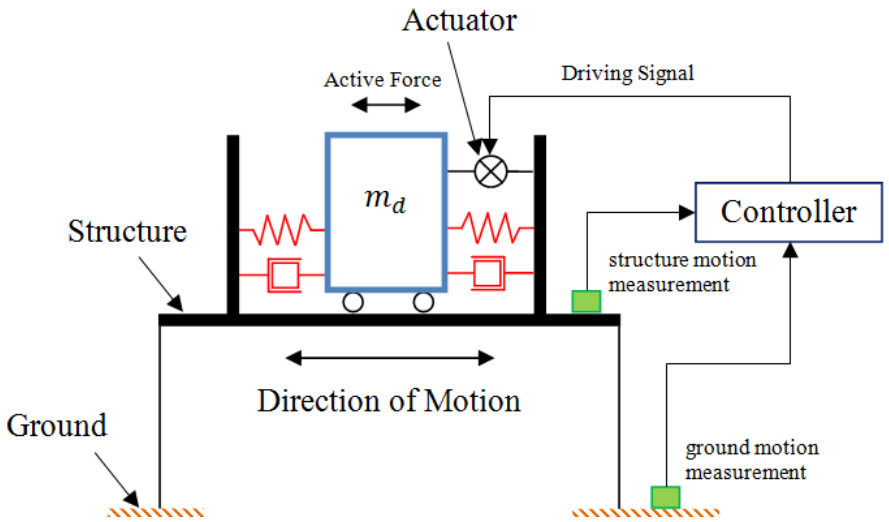

Figure 4: Schematic of an ATMD

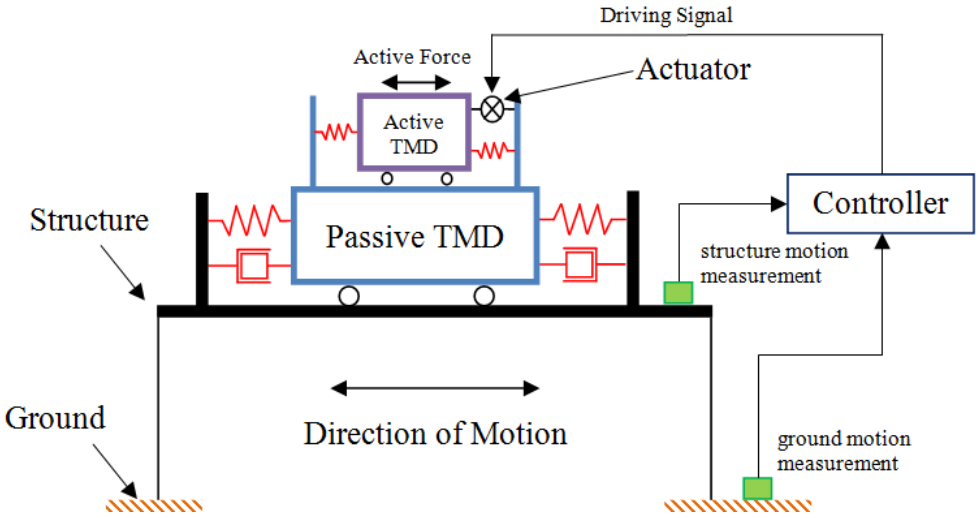

Figure 5: Schematic of a hybrid ATMD

SATMD systems combine the advantages of both passive and active systems. These systems provide active control of either the stiffness or dampening components of the TMD system, instead of driving the system itself. The power requirements to control these components are orders of magnitude lower than the power required to drive the TMD mass for active systems (e.g. Lin et al. 2010, Nagarajaiah and Varadarajan 2005, and Chey et al. 2010). Since SATMDs

do not supply mechanical energy to the structure they are considered passive systems. Hence, they preserve system stability. By providing active control of the TMD components at lower energy costs, they provide improved performance over passive TMD systems while mitigating the negative attributes of ATMD systems.

There are numerous methods of providing active control to TMD components. Nagarajaiah et al. (2005, 2007) utilized a semi-active variable stiffness TMD for the suppression of wind induced vibrations for a building model. The TMD system, shown in Figure 6, allows for adjustment in stiffness via the motion of a linear actuator. Setareh et al. (2002, 2007) proposed dampening control for a PTMD via a magneto rheological damper, as illustrated in Figure 7. The magneto rheological damper is a magnetically responsive fluid containing magnetisable particles, which in the presence of a magnetic field will affect the fluid's viscosity. Chey et al. (2007, 2010) conducted an analytical study of a SATMD using a resettable device in the form of a non-linear pneumatic spring. The conclusions common to each of these studies is that the semi-active design outperforms the equivalent passive design while providing superior performance for detuned testing conditions.

2.5 Multiple TMD Systems

Multiple TMD systems, as depicted in Figure 8, use multiple TMDs to reduce structural vibrations. Instead of using a single large mass tuned to the structures natural frequency, a multiple TMD uses several smaller TMD systems (Chen et al. 2001). Multiple TMD systems are innately passive systems; however their design allows them to be more robust to detuning conditions than traditional passive TMD designs.

In structures with limited space the use of several smaller TMD masses can allow for greater mass ratios (Sun et al. 1992). For example, if one large TMD system (tuned to the structures natural frequency) is divided into several smaller TMD systems (also tuned to the structures natural frequency) with an equivalent mass to the original TMD system, then both systems will have an equivalent dynamic response (Sun et al. 1992).

Generally, multiple TMD designs contain individual TMD systems tuned to different frequencies. There are two approaches to this implementation. The first is to utilize multiple

TMD systems tuned to multiple structural modal frequencies. This is a commonly used approach in real structures. For example, the antennae sitting atop the Canadian National Tower contains two twenty tonne pendulum type dampers tuned to the structure`s second and fourth vibration modes (Conner 2003). The second approach is to utilize multiple TMD systems tuned

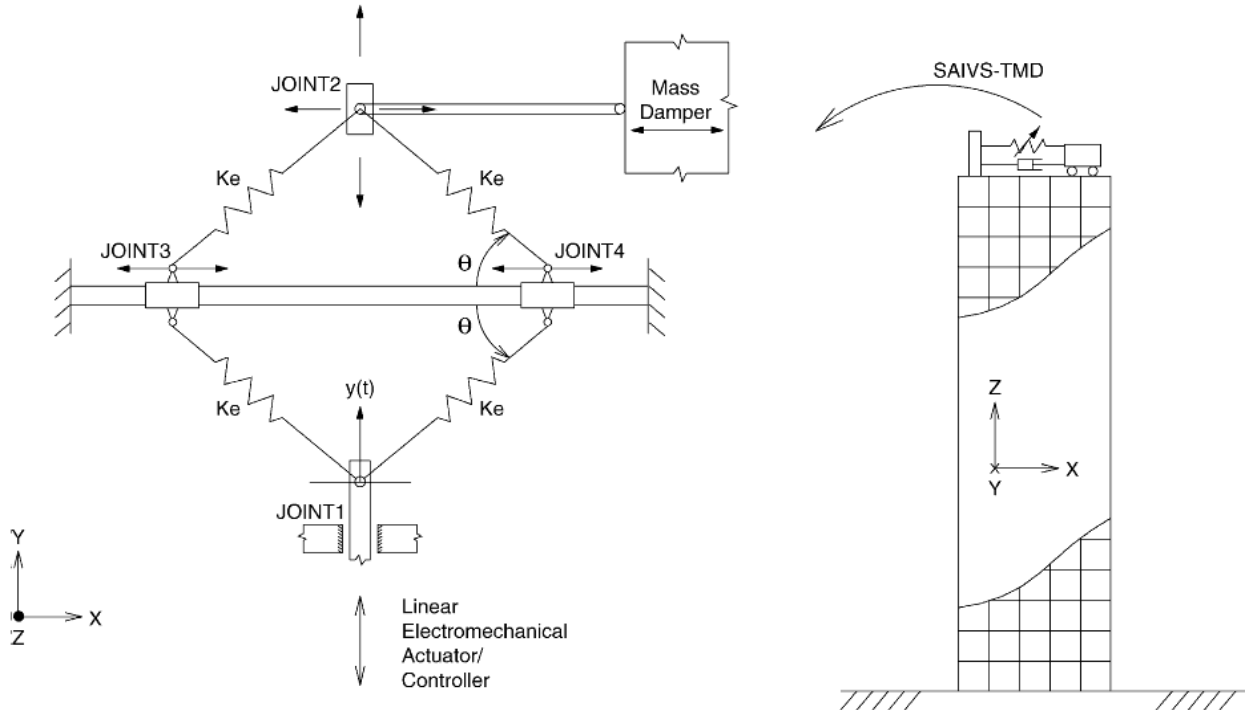

Figure 6: Semi-active variable stiffness TMD system (Nagarajaiah 2005 and 2007)

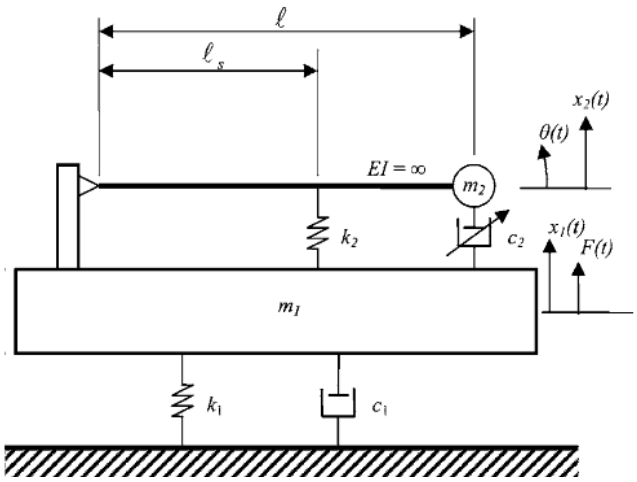

Figure 7: Semi-active pendulum TMD system using a magneto rheological damper (Setareh 2003 and 2007)

to frequencies distributed around the structure's natural frequency. Igusa and Xu (1994) demonstrated that the optimal approach is to distribute the tuned frequencies of the individual

TMD systems about the natural frequency. They concluded that the optimized designed multiple TMD system is more robust and effective than the equivalent mass optimized single TMD system. Lin and Cheng (2001) evaluated the use of an optimized multiple TMD system to reduce the buffeting response and increase the critical wind speed of long spanning bridges. The results show that multiple TMD systems, once optimized, perform better and are more robust against wide frequency bandwidth wind excitation than the equivalent mass optimized passive TMD system. Chen et al. (2001) made similar observations for structures induced by seismic loading.

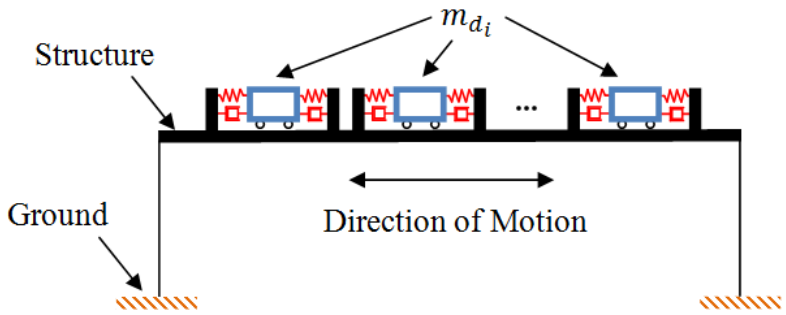

Figure 8: Schematic of multiple TMD

2.6 TMD Systems and Sources of Dynamic Loading

Structural vibrations are induced by dynamic loading. The majority of dynamic loads are induced by environment, machines, vehicles, or blasts (Tedesco 1999). Environmentally induced loading is common to all structures. Examples of environmentally induced dynamic loads on a structure are wind loads, wave loads, and earthquake loads. Machine induced loads are often harmonic and periodic. An example of machine loading includes the dynamic loads from a turbine in a power generation plant. Vehicular induced loading is common in bridges and airports where pedestrians, cars and planes frequent. They can be characterised by periodic loading, where the exciting frequency is dependent on the rate of traffic. Blast induced loading can be represented by a large build-up and release of fluid pressure. They are relatively rare considering they are the result of explosions.

TMDs are used primarily to reduce structural vibration from wind induced loads in tall building structures and long spanning bridges (e.g., Nagarajaiah and Sonmez 2007, and Brownjohn et al. 2010). The building response from wind loading tends to excite the translational and torsional

modes, as dictated by its along-wind and cross-wind loading (Mendis et al. 2007). Along-wind loads primarily consist of turbulence induced by wind gusts. Cross-wind loadings are primarily the result of vortex shedding; a periodic cross-wind loading which can create resonant conditions if it coincides with the structures natural frequencies. As a result, in some structures, these cross-wind loads tend to excite the structure continuously at specific structural natural frequencies.

Earthquake loads are often impulsive and can excite a wider range of structural natural frequencies (Chen and Wu 2001). Earthquake loads can vary significantly. The time required for sufficient energy to propagate to the TMD to allow for energy dissipation may be greater than the duration of ground vibrations. Furthermore earthquake loads may excite higher structural modes. The use of a single passive TMD system is often insufficient in suppressing structural motion due to earthquake loads (Clark 1988). Chen and Wu (2001) modeled a multiple TMD system with 30 dampers on a six storey building and subjects the structure to historic acceleration data from 13 earthquakes. By using a multiple TMD system at optimal placements within the structure, Chen observed a reduction in acceleration ranging from 10% to 25% over a traditional TMD system. The variation in performance, as Chan observed, is due to the width of the band of excited frequencies and the duration of the seismic activity. Similar results are reported by Lin et al. (2010) and Chey et al. (2007, 2010) in the application of SATMD systems for seismic activity.

The use of TMDs to suppress machine induced vibration is limited. Generally vibration suppression can be achieved internally within the machine itself. For example, TMDs are commonly inserted in production cars to control torsional vibration on the crankshaft pulley. Both production cars and racing cars utilize TMDs on their suspension systems to reduce the amplitude of vibration of the suspension and improve the down force of the vehicle. However the implementation of TMD systems on structures for machine induced loading is rare. One explanation is that human perception to higher frequency vibration at low accelerations is not as significant. Furthermore structural vibration modes are often lower than the frequency at which machines operate at. Chang et al. (2010) explored the use of a vertical TMD system on a two floor structure excited by a shaker motor. When the shaker motor excited the structure at its fundamental frequency of 23 Hz the floor vibration amplitudes were reduced by as much as 50%.

TMD systems have been implemented on structures to reduce floor vibrations from pedestrian motion. Excessive floor vibrations are a common occurrence in high pedestrian traffic areas such as workspaces, malls, airports, and museums. The cause of these floor vibrations is generally due to the floor structure being excited at or near its natural frequency by human movements (Setareh and Hanson 1992). Other contributing factors include the reduction in floor mass and stiffness and the use of longer beams for the floor joists. TMDs represent a practical solution for excessive floor vibrations since they are external to the floor system. Adding additional bracing to floor joints is impractical and expensive. Furthermore TMD systems are relatively compact and can fit within floor joists, as shown in Figure 9. Setareh et al. (2002, 2006, and 2007) presented two different TMD designs to mitigate floor vibrations: a PTMD system and a SATMD. The use of a TMD was found to reduce floor vibrations by up to 70%. In the case of the PTMD system the results are contingent on two conditions: the PTMD remaining tuned and a narrowband excitation force. Both conditions are difficult to verify since the excitation range from pedestrian motion will vary and adding or subtracting mass from the floor will adjust the floor's natural frequency (Setareh et al. 2006). Carpineto et al. (2010) also explored the use of a multiple TMD system to reduce excessive vibration for the Singapore Suspension Footbridge. The bridge vibration, which is caused by the synchronization of lateral footfall forces, saw reductions in vertical acceleration as high as 80 % at its mid and quarter span sections.

The use of TMD systems is not applicable to blast loads since the response to blast loads is entirely transient. Instead building designs for blast loads are primarily focused on enhancing the structural strength.

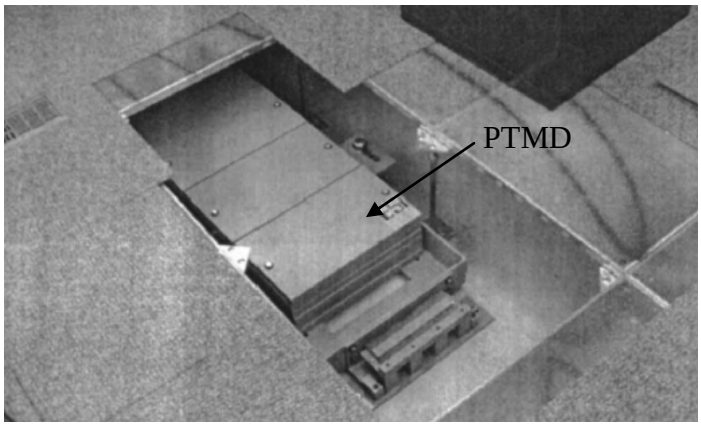

Figure 9: PTMD hidden below raised floor (Setareh, 2006)

Chapter 3: Pendulum Tuned Mass Damper Model

The analytical model to be presented is an idealized version of the real implementation of a PTMD system. The motivation is to illustrate the effect of a PTMD on the motion of a structure when it is excited. Additionally, the implementation of the analytical PTMD model will demonstrate the PTMD performance when: (i) the frequency of the PTMD moves away from the structure's natural frequency, (ii) when the PTMD damping is adjusted, and (iii) when the PTMD mass to structure's mass ratio is changed.

3.1 Analytical PTMD and SDOF Structure Model

3.1.1 Structure Model

The structure model is a SDOF model with a discrete lumped mass represented by M. The motion of the mass is defined by the displacement coordinate $x(t)$. Attached to the mass is an ideal spring with constant stiffness k. The energy contained in the system is dissipated with a viscous damper having a damping coefficient b. The structure is excited by a time varying force $F(t)$. A schematic of the structure model is shown in Figure 10.

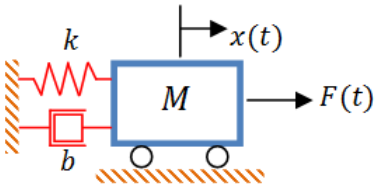

Figure 10: SDOF structure schematic

To formulate the equations of motion for the system, D'Alembert's principle of dynamic equilibrium is employed. D'Alembert's principle states that the sum of the differences of the forces acting on a system and the time derivative of the momentum of the system itself is equivalent to zero at all times (Tedesco at al. 1999). The time derivative of the momentum of the system is simply an application of Newton's second law, and for the proposed system is equivalent to the product of the mass and acceleration. A free body diagram of the structure

model is shown in Figure 11. The dynamic equation of motion for the structure model is given by Eq. 3-1.

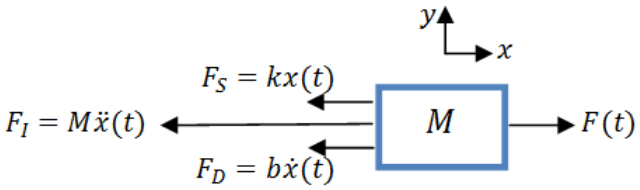

Figure 11: Free body diagram of SDOF structure model

$$\ddot{x}(t) + \frac{b}{M}\dot{x}(t) + \frac{k}{M}x(t) = \frac{1}{M}F(t) \qquad \textbf{(3- 1)}$$

It is clear that the motion of the structure is related to the external forcing function $F(t)$. Since TMD designs are dependent on the frequency spectrum of the external loading, the external forcing function is assumed to be periodic. To evaluate the frequency response of the structure model, the Laplace transform is applied to Eq. 3-1. The resultant expression is the transfer function model of the system (Eq. 3-2).

$$G(s) = \frac{X(s)}{F(s)} = \frac{\frac{1}{M}}{s^2 + \frac{b}{M}s + \frac{k}{M}} = \frac{\frac{1}{M}}{s^2 + 2\xi\omega s + \omega^2} \qquad \textbf{(3- 2)}$$

where

$$\xi = \frac{b}{b_{cr}} = \frac{b}{2\sqrt{kM}} \qquad \omega = \sqrt{\frac{k}{M}}$$

Note that system coefficients k and b are replaced with ξ and ω, which represent the structure's damping ratio and natural frequency.

A Bode plot is used to visualize the spectral response of the structure. The selected values for the physical parameters are shown in Table 1. These values are based on the experimental test structure, which will be discussed in detail in the subsequent chapter. Refer to Appendix A for the identification methodology used to identify these values. The resultant natural frequency and damping ratio is 1.855 Hz and 0.024 respectively. A Bode magnitude plot of the transfer function is shown in Figure 12. It is clear that the greatest gain occurs at 1.856 Hz. This is the damped natural frequency of the SDOF structure model. Observe that the response outside of the narrow

frequency band surrounding the damped natural frequency is orders of magnitude less than the response in the resonant region. Typical real structures fall within this range of frequency and damping; and, although their response is not as simple as the response identified for a SDOF structure model, they can exhibit large deflections when excited within small frequency bands. As a result TMD effectiveness is heavily reliant on its tuned frequency.

M	$32.10\ kg$
k	$3713\ N/m$
b	$15.28\ \mathrm{N/(m/s)}$

Table 1: Physical parameters of a SDOF structure

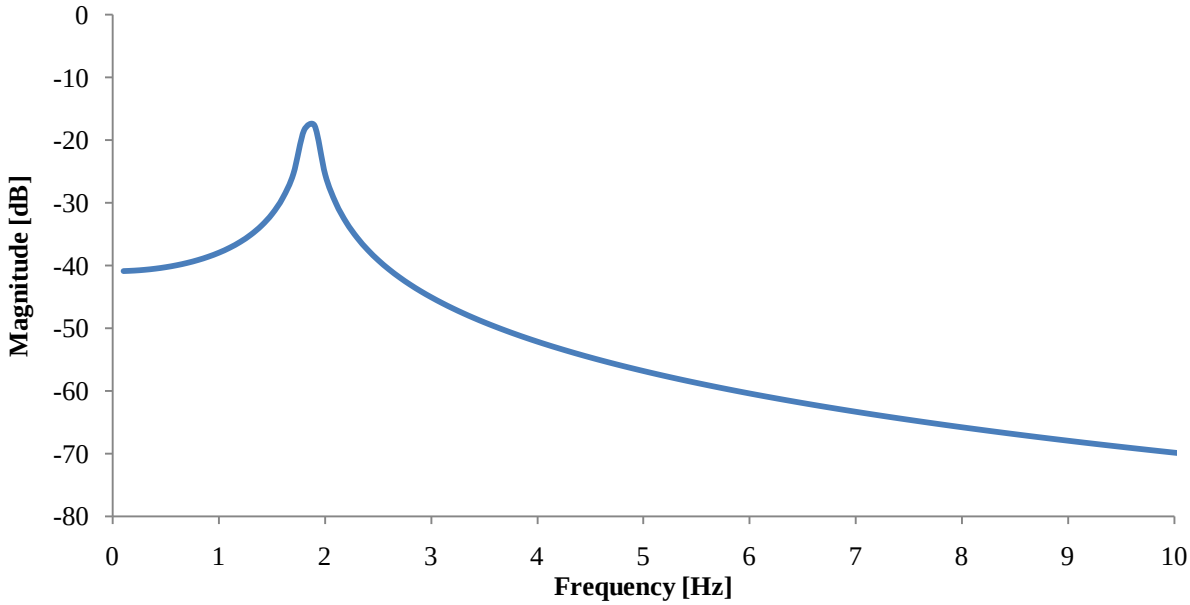

Figure 12: Bode magnitude plot of the SDOF structure transfer function model

3.1.2 PTMD Model

The PTMD system can be modelled as a simple pendulum with a point mass m supported by a massless rod of length L (Figure 13). The rod pivots about a single point. The pendulum friction constant is represented by coefficient c. The damper connecting the pendulum mass and the structure is represented by a viscous damper with damping coefficient d. The damper is restricted to move horizontally.

D'Alembert's principle is used to evaluate the equations of motion for the PTMD model. A free body diagram of the pendulum mass is shown in Figure 14. Note that there is a reaction force T representing the tension in the massless rod. Furthermore there is a pendulum friction torque equal to the cross product of the friction force vector and the moment arm vector. Hence the direction of the friction force on the pendulum mass is perpendicular to the moment arm in the direction opposing the motion of the pendulum mass. The equation of motion for the PTMD model is given by Eq. 3-3.

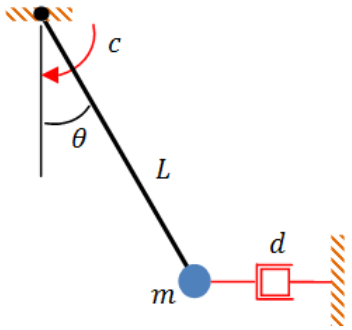

Figure 13: PTMD schematic

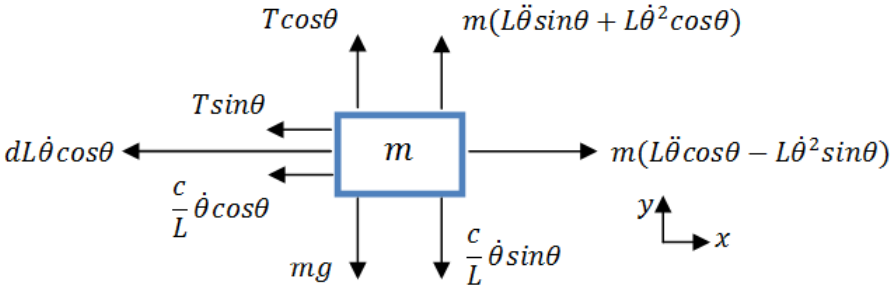

Figure 14: Free body diagram of PTMD model

$$\ddot{\theta}(t) = -\frac{1}{mL}\left(\frac{c}{L} + dLcos^2\theta(t)\right)\dot{\theta}(t) - \frac{g}{L}\sin\theta(t) \qquad \textbf{(3- 3)}$$

The equation of motion of the PTMD model is a non-linear expression. Under typical loading conditions, the angular rotation of the pendulum mass will perturb slightly about the stable equilibrium point. As such the non-linear equation of motion can be linearized by observing that the non linear terms $\cos\theta(t)$ and $sin\theta(t)$ can be approximated to 1 and $\theta(t)$ about the equilibrium point. The linearized equation of motion for the PTMD model is given by Eq. 3-4.

$$\ddot{\theta}(t) = -\frac{1}{mL}\left(\frac{c}{L} + dL\right)\dot{\theta}(t) - \frac{g}{L}\theta(t) \qquad \textbf{(3- 4)}$$

The output of the model is the free response. To evaluate the free response of the PTMD model the Laplace transform is applied to Eq. 3-4. The resultant expression is shown in Eq. 3-5. Note that the terms $\theta(0)$ and $\dot{\theta}(0)$ are the initial angular displacement and angular velocity of the pendulum mass. The free response in the time domain is obtained by evaluating the inverse Laplace transform of Eq. 3-5, and is represented in Eq. 3-6.

$$\theta(s) = \frac{\left(s + \frac{1}{mL}\left(\frac{c}{L} + dL\right)\right)\theta(0)}{s^2 + \frac{1}{mL}\left(\frac{c}{L} + dL\right)s + \frac{g}{L}} = \frac{(s + 2\xi_d\omega_d)\theta(0) + \dot{\theta}(0)}{s^2 + 2\xi_d\omega_d s + {\omega_d}^2} \quad \textbf{(3- 5)}$$

where

$$\xi_d = \frac{\left(\frac{c}{L} + dL\right)}{2m\sqrt{gL}} \qquad \omega_d = \sqrt{\frac{g}{L}}$$

$$\theta(t) = \theta(0)e^{-\xi_d\omega_d t}\left(cos\omega_{dn}t + \frac{\xi_d}{\sqrt{1 - {\xi_d}^2}}sin\omega_{dn}t\right) + \frac{\dot{\theta}(0)}{\omega_d}e^{-\xi_d\omega_d t}sin\omega_{dn}t \quad \textbf{(3- 6)}$$

where

$$\omega_{dn} = \omega_d\sqrt{1 - {\xi_d}^2} = \frac{1}{2mL}\sqrt{4m^2gL - \left(\frac{c}{L} + dL\right)^2}$$

Note that system coefficients are replaced with ξ_d, ω_d, and ω_{dn} which represent the pendulum damping ratio, natural frequency, and damped natural frequency.

Given that the system will be under damped, the pendulum mass will oscillate at its damped natural frequency. Simulations for the PTMD model are performed based on model parameters shown in Table 2. These parameters are based on the prototype APTMD-adaptive pendulum system which will be presented in greater detail in the following chapter. For the simulations, the pendulum is assumed to have no initial angular velocity and an initial angular displacement of 5°. The simulated free response of the pendulum model is shown in Figure 15. The free response of the pendulum mass is an exponentially decaying sinusoid. The rate of decay is relative to the damping ratio. For the simulation the damping ratio is 0.1046. Reducing the damping coefficient will reduce the damping ratio and decay rate of the pendulum mass free response. The simulated free response oscillates at 1.847 Hz which is equivalent to the damped natural frequency.

m	1.470 kg
c	0.0072 Nms
g	9.800 m/s^2
L	0.072 m
d	2.2 Ns/m

Table 2: Physical parameters of PTMD

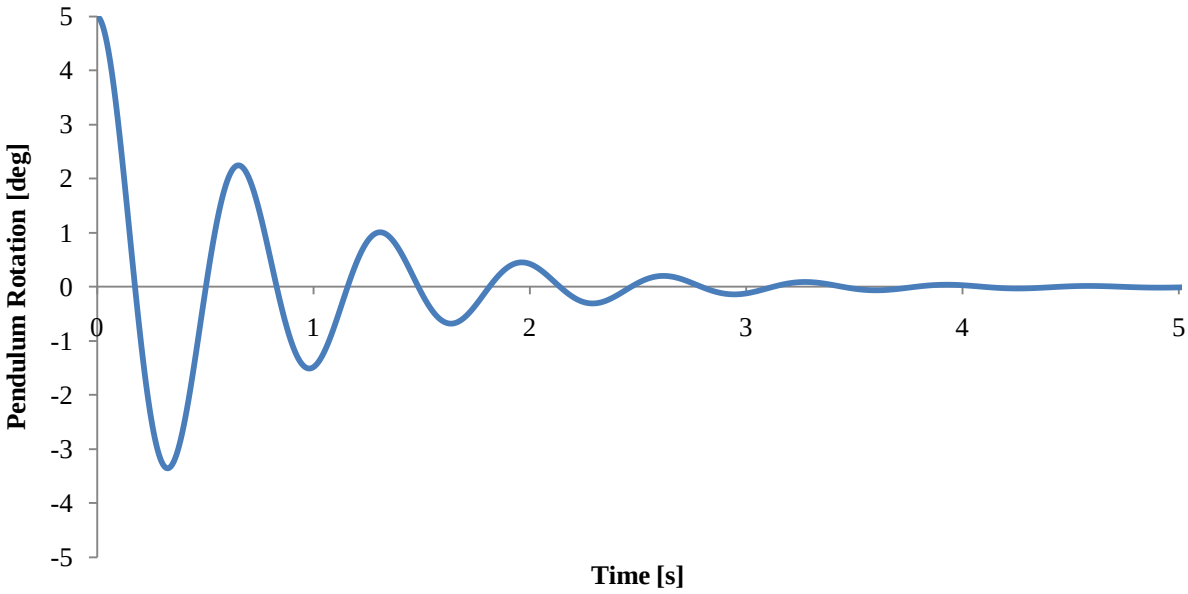

Figure 15: Simulated free response of PTMD model

3.1.2 Combined Structure and PTMD Model

The combined structure and PTMD model consists of the PTMD model mounted to the structure. A schematic of the PTMD model and the connected structure is shown in Figure 16. The resultant model contains the dynamics of the individual structure and PTMD models and the coupling dynamics between the two models.

Euler-Lagrange method (Tedesco et al. 1999) is used to evaluate the equations of motion for the combined SDOF structure and PTMD system. The system is written in terms of two generalized coordinates: the horizontal position of the mass and the rotation of the pendulum mass. The generalized coordinates are summarized in Eq. 3-7.

$$z_1 = x(t) \qquad z_2 = \theta(t) \tag{3- 6}$$

The Lagrangian is the summation of the kinetic energy minus the summation of the potential energy for the structure mass and the pendulum mass. The kinetic energy for both the structure mass and the pendulum mass is shown in Eq. 3-8. The sources of potential energy are from the conservative forces in the system: the stiffness of the structure and the gravitational potential of the pendulum mass. The potential energy of the system is shown in Eq. 3-9. The Lagrangian for this system is shown in Eq. 3-10.

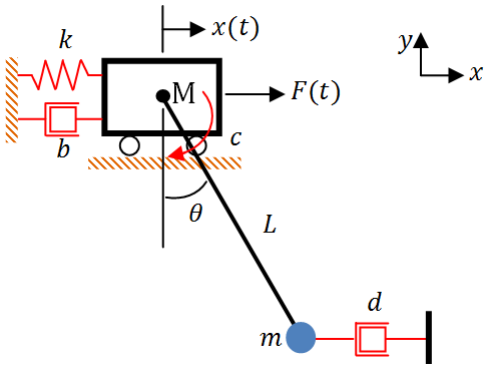

Figure 16: SDOF Structure and Pendulum TMD Schematic

$$T = \frac{1}{2}M\dot{z_1}^2 + \frac{1}{2}m((\dot{z_1} + L\dot{z_2}cosz_2)^2 + (L\dot{z_2}sinz_2)^2) \quad \textbf{(3- 8)}$$

$$V = \frac{1}{2}kz_1^2 + mgL(1 - cosz_2) \quad \textbf{(3- 9)}$$

$$L = T - V = \frac{1}{2}M\dot{z_1}^2 + \frac{1}{2}m\left(\dot{z_1}^2 + 2\dot{z_1}L\dot{z_2}cosz_2 + L^2\dot{z_2}^2\right) - \frac{1}{2}kz_1^2 - mgL(1 - cosz_2) \quad \textbf{(3- 10)}$$

There are four non-conservative forces which must be considered: the three viscous dampers and the external load. The work done by non-conservative forces on the structure is given by Eq. 3-11. The work done by non-conservative forces on the pendulum mass (Eq. 3-12) is the sum of the work done by the viscous damping force at the pendulum pivot and the viscous damping force of the damper.

$$Q_1 = F(t) - b\dot{z_1} \quad \textbf{(3- 11)}$$

$$Q_2 = -c\dot{z_2} - dL^2\dot{z_2}cos^2z_2 \quad \textbf{(3- 12)}$$

The generalized Euler-Lagrange equation is represented in Eq. 3-13 (Tedesco et al. 1999). Application of the Euler-Lagrange equation for this system results in two non-linear equations of motion (Eq. 3-14). The state space representation of the system is shown in Eq. 3-15.

$$\frac{d}{dt}\left(\frac{\partial \mathcal{L}}{\partial \dot{z}_i}\right) - \frac{\partial \mathcal{L}}{\partial z_i} = Q_i \qquad i = 1,2,\ldots,n \tag{3- 13}$$

$$\begin{gathered}(M+m)\ddot{z}_1 + mL\ddot{z}_2 cosz_2 = F(t) - kz_1 - b\dot{z}_1 + mL\dot{z}_2{}^2 sinz_2 \\ \ddot{z}_1 cosz_2 + L\ddot{z}_2 = -gsinz_2 - \frac{1}{m}\left(\frac{c}{L} + dLcos^2 z_2\right)\dot{z}_2\end{gathered} \tag{3- 14}$$

$$\dot{x} = \begin{bmatrix} x_2 \\ \dfrac{u + mgcosx_3 sinx_3 + cosx_3\left(\frac{c}{L} + dLcos^2 x_3\right)x_4 - kx_1 - bx_2 + mLx_4{}^2 sinx_3}{M + m(1 - cos^2 x_3)} \\ x_4 \\ \dfrac{-\frac{(M+m)}{m}\left(\frac{c}{L} + dLcos^2 x_3\right)x_4 - (M+m)gsinx_3 - cosx_3(mLx_4{}^2 sinx_3 + u - kx_1 + bx_2)}{L(M + m(1 - cos^2 x_3))} \end{bmatrix} \tag{3- 15}$$

where

$$x = \begin{bmatrix} x_1 \\ x_2 \\ x_3 \\ x_4 \end{bmatrix} = \begin{bmatrix} z_1 \\ \dot{z}_1 \\ z_2 \\ \dot{z}_2 \end{bmatrix} = \begin{bmatrix} x \\ \dot{x} \\ \theta \\ \dot{\theta} \end{bmatrix} \qquad u = F(t)$$

$$\dot{x} = f(x,u) = \begin{bmatrix} f_1(x,u) \\ f_2(x,u) \\ f_3(x,u) \\ f_4(x,u) \end{bmatrix}$$

The equations of motion for the structure and PTMD system are non-linear. In order to observe the frequency response of the system the equations of motion must be linearized about an operating point. The operating point will be the equilibrium point of the system, as defined in Eq. 3-16. Specifically, the structure will be stationary if the position of the pendulum mass is at 0 radians and π radians while the structure is at rest. The latter case is when the pendulum mass is inverted and is not applicable for the given system. The perturbed state variables are shown in Eq. 3-17. The formulation of the linearized system is shown in Eq. 3-18. Note that the linearized system will only provide an accurate measure of the frequency response for small perturbations of the state variables around the operating point. For structural vibrations this is a valid assumption.

$$\begin{bmatrix} x_1(0) \\ x_2(0) \\ x_3(0) \\ x_4(0) \end{bmatrix} = \begin{bmatrix} 0 \\ 0 \\ 0 \\ 0 \end{bmatrix}, \begin{bmatrix} 0 \\ 0 \\ \pi \\ 0 \end{bmatrix} \qquad u(0) = 0 \tag{3- 16}$$

$$\Delta x = \begin{bmatrix} \Delta x_1 \\ \Delta x_2 \\ \Delta x_3 \\ \Delta x_4 \end{bmatrix} = \begin{bmatrix} x_1 - x_{1_0} \\ x_2 - x_{2_0} \\ x_3 - x_{3_0} \\ x_4 - x_{4_0} \end{bmatrix} = \begin{bmatrix} x_1 \\ x_2 \\ x_3 \\ x_4 \end{bmatrix} \qquad \Delta u = u - u_0 = u \tag{3- 17}$$

$$\begin{bmatrix} \Delta \dot{x}_1 \\ \Delta \dot{x}_2 \\ \Delta \dot{x}_3 \\ \Delta \dot{x}_4 \end{bmatrix} = \begin{bmatrix} 0 & 1 & 0 & 0 \\ -\frac{k}{M} & -\frac{b}{M} & \frac{mg}{M} & \frac{\frac{c}{L} + dL}{M} \\ 0 & 0 & 0 & 1 \\ \frac{k}{ML} & \frac{b}{ML} & -\frac{(M+m)g}{ML} & -\frac{\frac{(M+m)}{m}\left(\frac{c}{L} + dL\right)}{ML} \end{bmatrix} \begin{bmatrix} \Delta x_1 \\ \Delta x_2 \\ \Delta x_3 \\ \Delta x_4 \end{bmatrix} + \begin{bmatrix} 0 \\ \frac{1}{M} \\ 0 \\ -\frac{1}{ML} \end{bmatrix} \Delta u \tag{3- 18}$$

3.2 PTMD Performance

3.2.1 Solution to the Analytical Combined PTMD and Structure Model

The desire is to demonstrate the PTMD performance due to changes in the mass of the pendulum, the pendulum damping, and the tuned frequency of the PTMD. To evaluate these changes, the closed form solution of Eq. 3-18 will be expressed in terms of the damping ratio of the structure and PTMD, the mass ratio, the excitation frequency ratios, and the tuned frequency ratio. The expressions for these variables are represented in Table 3.

The linearized equations of motion expressed in terms of the horizontal displacements of the structure and pendulum masses are shown in Eq. 3-19. By expressing the motion of the pendulum mass in terms of its horizontal displacement instead of its rotational displacement, the system is converted into an equivalent translational TMD system, as illustrated in Figure 17. This representation is beneficial since spatial constraints are generally described in terms of horizontal and vertical dimensions.

$\bar{m}$	$\frac{m}{M}$	Mass ratio
ω	$\sqrt{\frac{k}{M}}$	Natural frequency of structure
ξ	$\frac{b}{2\omega M}$	Damping ratio of structure
ω_d	$\sqrt{\frac{g}{L}}$	Natural frequency of PTMD
ξ_d	$\frac{\frac{c}{L}+dL}{2\omega_d mL}$	Damping ratio of PTMD
α	$\frac{\Omega}{\omega}$	Structural excitation frequency ratio
β	$\frac{\omega_d}{\omega}$	Tuned frequency ratio

Table 3: PTMD model expressions

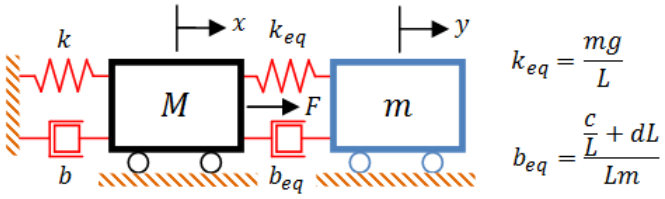

Figure 17: Equivalent translational TMD system

$$\ddot{x} + 2\xi\omega\dot{x} + \omega^2 x = 2\bar{m}\xi_d\omega_d\dot{y} + \bar{m}{\omega_d}^2 y - \frac{1}{M}F$$
$$\ddot{y} + 2(1+\bar{m})\xi_d\omega_d\dot{y} + (1+\bar{m}){\omega_d}^2 x = 2\xi\omega\dot{x} + \omega^2 x + \frac{1}{M}F \quad \textbf{(3- 19)}$$

where

$$y = L\theta \qquad \dot{y} = L\dot{\theta} \qquad \ddot{y} = L\ddot{\theta}$$

The solution to the linearized system expressed in Eq. 3-19 can be represented as a sum of homogenous and non-homogenous solutions. The homogenous solution, or the transient response, dies out after a finite time at a rate dependant on the internal dampening of the system (Franklin et al. 2009). The non-homogenous solution, or steady state response, persists as long as the input excitation is provided to the system. For passively controlled systems, the homogenous solution is generally ignored since the system is incapable of controlling the transient response (Tedesco et al. 1999). Furthermore, in vibration analysis engineers are generally interested in the structure's steady state response. Hence, the homogeneous solution will be ignored.

The excitation force is considered to be periodic with a frequency Ω and amplitude F_0 (Eq. 3-20). The solution to the linearized system is assumed to be in the form given by Eq. 3-21. It is determined by substituting the assumed response for the respective state variables into the equations of motion and algebraically determining the unknown coefficients. The closed-form solution for the horizontal displacement of the SDOF structure mass and the pendulum mass is given by Eq. 3-22. The displacement amplitudes are a function of the displacement amplification factors, X and Y, which are a function of the controllable PTMD parameters. Furthermore the phase angles, δ_1 and δ_2, between the input excitation and the horizontal displacement of the structure and pendulum mass are also a function of the controllable PTMD parameters.

$$F(t) = F_0 e^{i\Omega t} \tag{3- 20}$$

$$x(t) = A\cos(\Omega t) + B\sin(\Omega t) = X_0 e^{i(\Omega t+\delta_1-\delta_2)}$$
$$y(t) = C\cos(\Omega t) + D\sin(\Omega t) = Y_0 e^{i(\Omega t-\delta_2)} \tag{3- 21}$$

$$x(t) = \frac{F_0}{k}\mathrm{X}e^{i(\Omega t+\delta_1-\delta_2)} \qquad y(t) = \frac{F_0}{k}\mathrm{Y}e^{i(\Omega t-\delta_2)} \tag{3- 22}$$

where

$$\delta_1 = Tan^{-1}\left(\frac{2\xi_d\beta\alpha}{(\beta^2-\alpha^2)}\right)$$

$$\delta_2 = Tan^{-1}\left(\frac{2\left(\xi\alpha(\beta^2-\alpha^2)+\xi_d\beta\alpha\left(1-\alpha^2(1+\bar{m})\right)\right)}{-\beta^2\alpha^2\bar{m}+(1-\alpha^2)(\beta^2-\alpha^2)-4\xi\xi_d\beta\alpha^2}\right)$$

$$\mathrm{X} = \frac{\sqrt{(\beta^2-\alpha^2)^2+(2\xi_d\alpha\beta)^2}}{\sqrt{(-\beta^2\alpha^2\bar{m}+(1-\alpha^2)(\beta^2-\alpha^2)-4\xi\xi_d\beta\alpha^2)^2+4\left(\xi\alpha(\beta^2-\alpha^2)+\xi_d\beta\alpha\left(1-\alpha^2(1+\bar{m})\right)\right)^2}}$$

$$\mathrm{Y} = \frac{\alpha^2}{\sqrt{(-\beta^2\alpha^2\bar{m}+(1-\alpha^2)(\beta^2-\alpha^2)-4\xi\xi_d\beta\alpha^2)^2+4\left(\xi\alpha(\beta^2-\alpha^2)+\xi_d\beta\alpha\left(1-\alpha^2(1+\bar{m})\right)\right)^2}}$$

3.2.2 Phase Difference

The difference in phase between the motion of the structure and pendulum mass allows for the dissipation of vibration energy from the structure. The phase difference when the structure is excited at its natural frequency ($\alpha = 1$) is given by Eq. 3-23. By inspection, the maximum phase difference occurs when the PTMD is tuned to the natural frequency of the structure ($\beta = 1$). Under these conditions, there is a 90° difference in phase between the horizontal displacement of the pendulum and structural mass. The resultant inertial loading from the pendulum mass will

also be 90° out of phase. Alternatively, the minimum phase difference occurs when either the PTMD contains no damping ($\xi_d = 0$) or the PTMD is fully detuned ($\beta = 0$).

$$\delta_1(\alpha = 1) = Tan^{-1}\left(\frac{2\xi_d\beta}{(\beta^2 - 1)}\right) \quad \textbf{(3- 23)}$$

Robust TMD designs allow for improved performance under detuned conditions. Figure 18 and Figure 19 illustrate the difference in phase between the horizontal displacement of the pendulum and structural mass under changing PTMD damping levels as the PTMD goes from the fully detuned to tuned position. It is evident that the robustness to detuning conditions is heavily reliant on the PTMD damping ratio. However, for all damping ratios the performance drop-off below $\beta = 0.95$ is significant. Hence, the performance of the non-adaptive PTMD system is heavily reliant on whether it is accurately tuned.

As the excitation frequency moves away from the natural frequency of the structure, the effectiveness of the PTMD at dissipating vibration energy decreases. Figure 20 and Figure 21 illustrates the difference in phase between the horizontal displacement of the pendulum and structural mass under changing excitation frequency conditions as the PTMD goes from the fully detuned to tuned position. It is evident that the PTMD performance deteriorates as the excitation frequency moves away from the resonant condition.

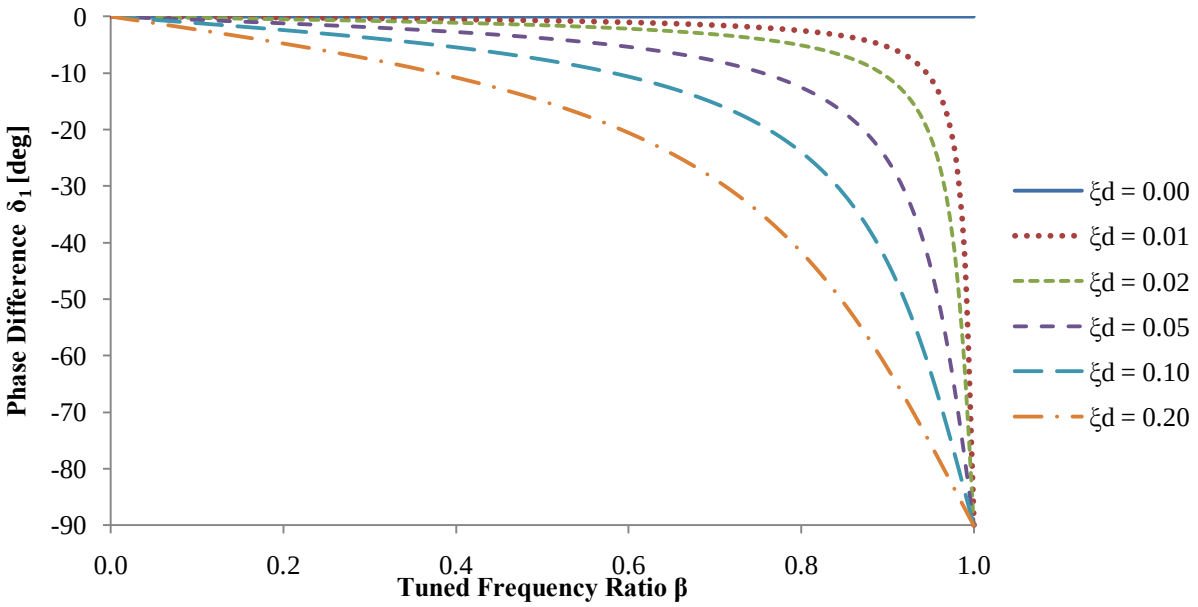

Figure 18: Phase difference vs. Tuned frequency ratio at resonant condition ($\alpha = 1$)

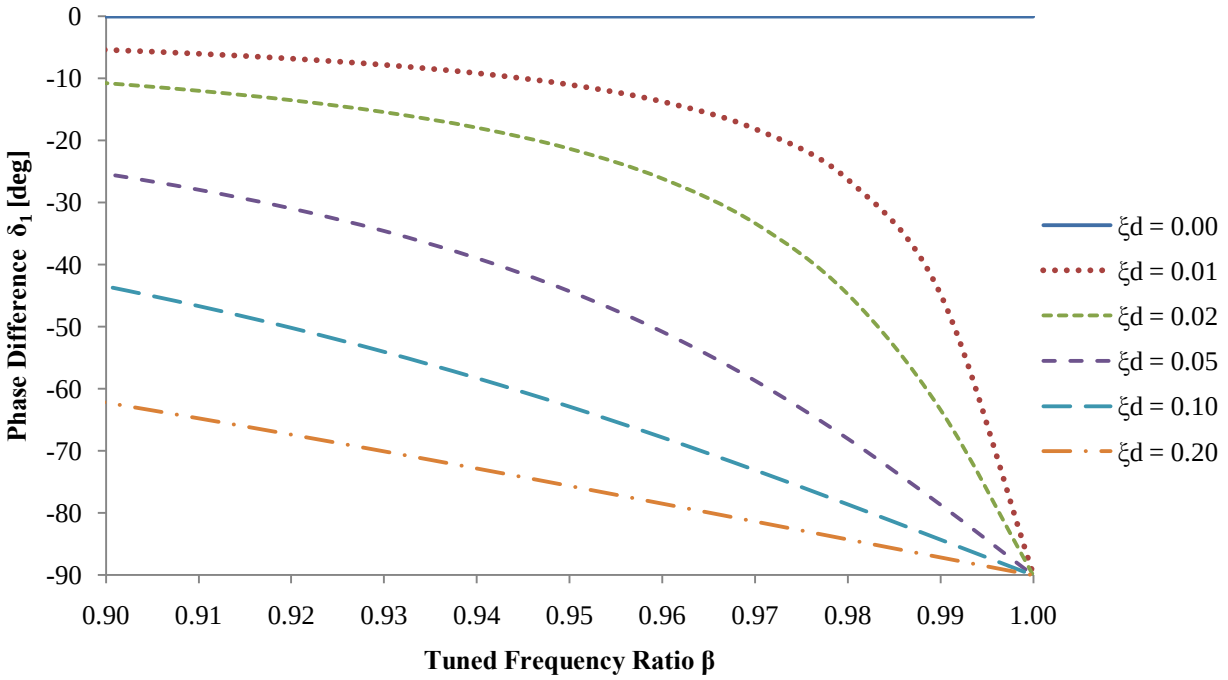

Figure 19: Phase difference vs. Tuned frequency ratio at resonant condition ($\alpha = 1$) above $\beta = 0.9$

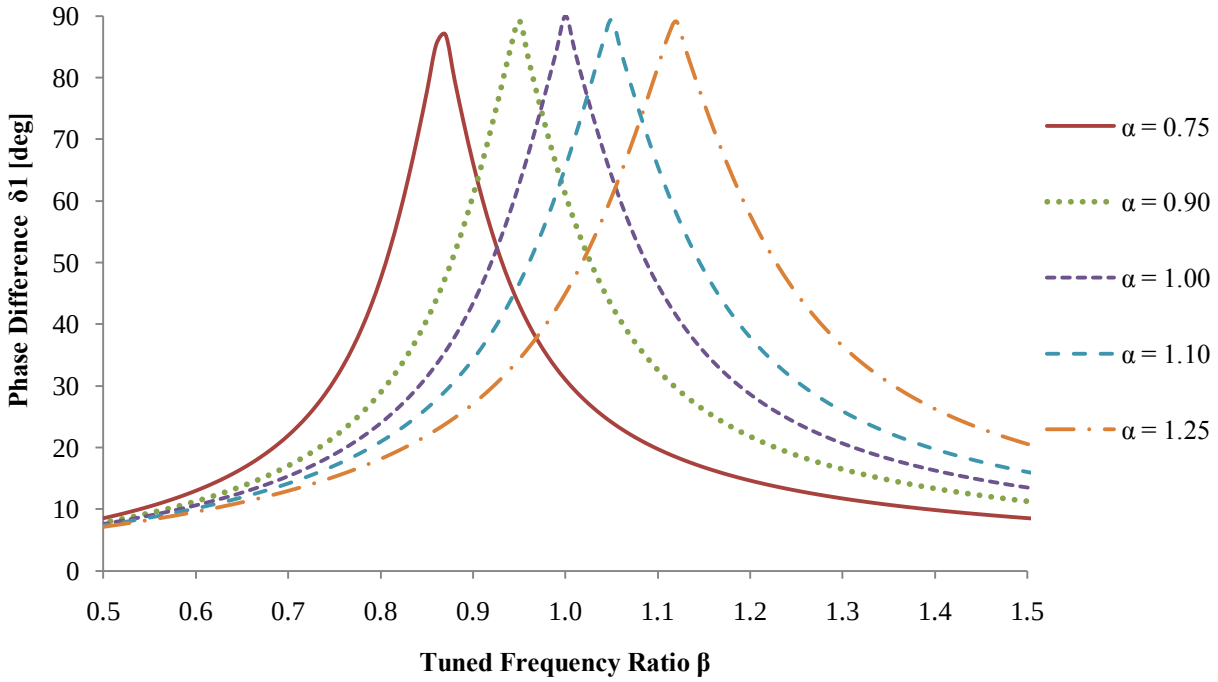

Figure 20: Phase difference vs. Tuned frequency ratio at multiple excitation frequencies for $\xi_d = 0.10$

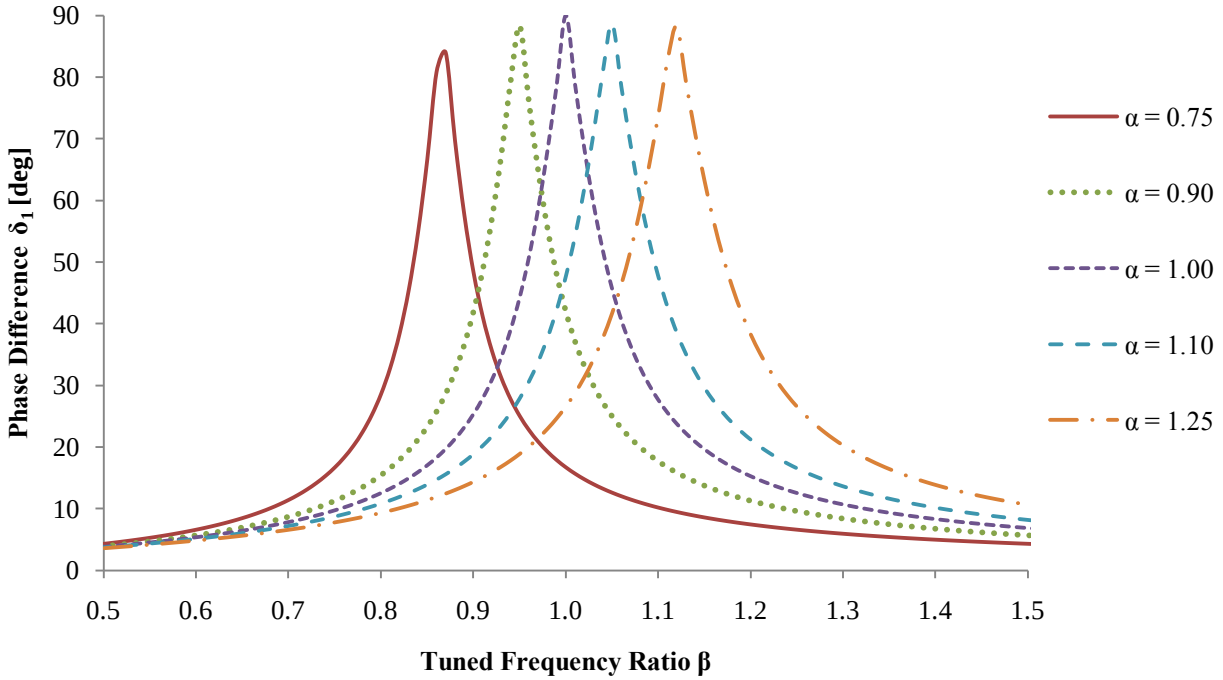

Figure 21: Phase difference vs. Tuned frequency ratio at multiple excitation frequencies for $\xi_d = 0.05$

3.2.3 Displacement Amplification Factors

The displacement amplification factors (Eq. 3-24) characterize the amplitude of vibration of the SDOF structure mass (denoted by X) and PTMD mass (denoted by Y) with respect to the controllable PTMD parameters. In the context of TMD design, the optimal PTMD performance parameters are obtained by minimizing the displacement amplification factor for the structure. Considerations must also be made to limit the displacement amplification factor of the PTMD mass due to spatial limitations in its installed condition.

$$X = \frac{\sqrt{(\beta^2-\alpha^2)^2+(2\xi_d\alpha\beta)^2}}{\sqrt{(-\beta^2\alpha^2\bar{m}+(1-\alpha^2)(\beta^2-\alpha^2)-4\xi\xi_d\beta\alpha^2)^2+4\left(\xi\alpha(\beta^2-\alpha^2)+\xi_d\beta\alpha\left(1-\alpha^2(1+\bar{m})\right)\right)^2}}$$

$$Y = \frac{\alpha^2}{\sqrt{(-\beta^2\alpha^2\bar{m}+(1-\alpha^2)(\beta^2-\alpha^2)-4\xi\xi_d\beta\alpha^2)^2+4\left(\xi\alpha(\beta^2-\alpha^2)+\xi_d\beta\alpha\left(1-\alpha^2(1+\bar{m})\right)\right)^2}} \quad \textbf{(3- 24)}$$

As an example, let the structure be excited at its natural frequency ($\alpha = 1$) and the PTMD tuned to the structures natural frequency ($\beta = 1$). In this case the displacement amplification factors is a function of the mass ratio, the damping ratio of the structure, and the damping ratio of the PTMD (Eq. 3-25). The damping ratio of the SDOF structure is assumed to be 0.024. This is

equivalent to the identified damping ratio of the experiment structure (refer to Appendix A). Figure 22 and Figure 23 illustrates the effects of changing the mass ratio and PTMD damping ratio on the displacement amplification factors for the given test configuration. Based on the simulated results it is clear that the greater the mass ratio, the smaller the amplitude of vibration for both the SDOF structure mass and the pendulum mass. This is apparent since a larger pendulum mass will result in a larger inertial damping force which opposes the motion of the structure when the PTMD is tuned. There is a physical limitation on the mass of the PTMD system, and as such the selected mass ratio is generally below 0.05 in real structures (Conner 2003). Additionally, decreasing the PTMD damping ratio will increase the damping to the structure while increasing the amplitude of motion of the PTMD mass. The physical limitations of the motion of the PTMD mass will limit the selection of the PTMD damping coefficient.

$$X = \frac{2\xi_d}{\sqrt{(\bar{m} + 4\xi\xi_d)^2 + 4(\xi_d\bar{m})^2}} \qquad Y = \frac{1}{\sqrt{(\bar{m} + 4\xi\xi_d)^2 + 4(\xi_d\bar{m})^2}} = \frac{1}{2\xi_d}X \qquad \textbf{(3- 25)}$$

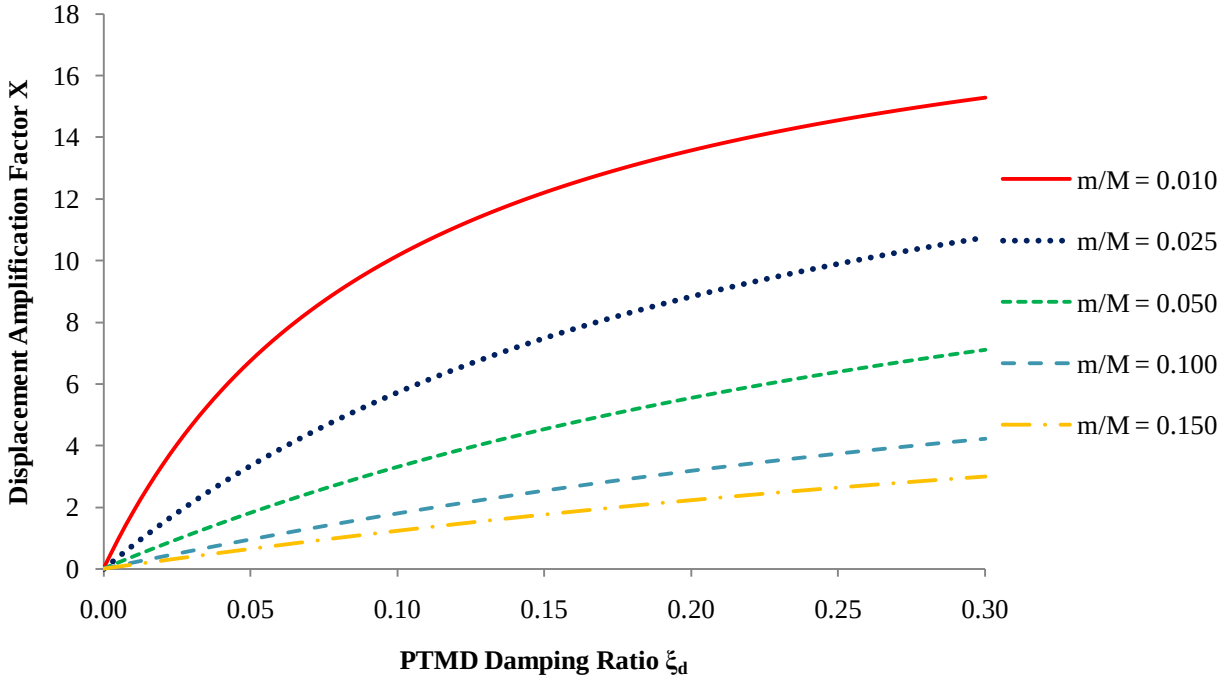

Figure 22: Displacement Amplification factor X vs. PTMD damping ratio for changing mass ratios

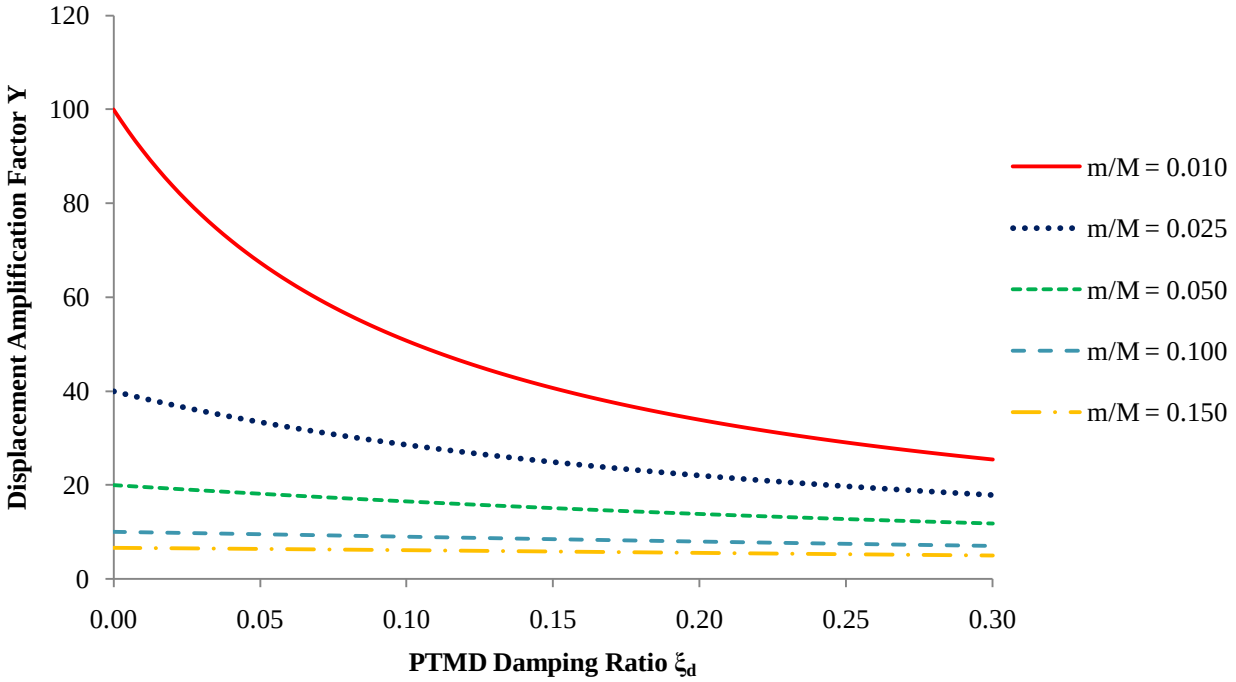

Figure 23: Displacement Amplification factor Y vs. PTMD damping ratio for changing mass ratios

The damping contribution of the PTMD system can be determined by comparing the response of the SDOF structure without the PTMD system to the response with the PTMD system. The response of the SDOF structure without the PTMD system is given by Eq. 3-26. The response of the same SDOF system when it is excited at its natural frequency is shown in Eq. 3-27. The equivalent damping ratio when the structure is excited at its natural frequency ($\alpha = 1$) and the PTMD is tuned to the structures natural frequency ($\beta = 1$) is shown in Eq. 3-28. Based on this expression it is evident that the amplitude of vibration of the SDOF structure decreases as the mass ratio increases, and increases as the PTMD damping ratio increases.

$$x(t) = \frac{F_0}{k}\frac{1}{\sqrt{(1-\alpha^2)^2 + 4(\xi\alpha)^2}} e^{i\left(\Omega t - Tan^{-1}\frac{2\xi\alpha}{1-\alpha^2}\right)} \quad \textbf{(3- 26)}$$

$$x(t) = \frac{F_0}{k}\frac{1}{2\xi} e^{i\left(\Omega t - \frac{\pi}{2}\right)} \quad \textbf{(3- 27)}$$

$$\xi_e = \frac{\bar{m}}{2}\sqrt{\left(\frac{1}{2\xi_d} + \frac{2\xi}{\bar{m}}\right)^2 + 1} \quad \textbf{(3- 28)}$$

where

$$x(t) = \frac{F_0}{k}\frac{1}{2\xi_e} e^{i(\Omega t + \delta_1 - \delta_2)}$$

The performance of the PTMD will be evaluated against detuned simulation conditions. The mass ratio will be fixed at 0.046. Once again the structure is excited at its natural frequency while the damping ratio of the SDOF structure is 0.024. Figure 24 shows the effects of changing the tuned frequency ratio on the structure's displacement amplification factor for several PTMD damping ratios. The results indicate that the amplitude of vibration is minimized when the PTMD is tuned to approximately 100% of the structure's natural frequency. Away from the tuned condition the amplitude increases significantly, where the rate of increase is inversely proportional to the PTMD damping ratio. Furthermore increasing the PTMD damping ratio decreases the overall damping of the structure, since the motion of the TMD is restricted. However, beyond certain detuned conditions (approximately 86% to 94% of the tuned frequency, depending on the level of damping) PTMDs with higher damping ratios outperform PTMDs with lower damping ratios. Figure 25 shows the effects of changing the tuned frequency ratio on the PTMD mass' displacement amplification factor for several PTMD damping ratios. The simulation indicates an inverse relationship between the amplitude of oscillation of the pendulum mass and the PTMD damping ratio. As a result, the selection of a lower PTMD damping ratio must account for larger horizontal displacements of the pendulum mass.

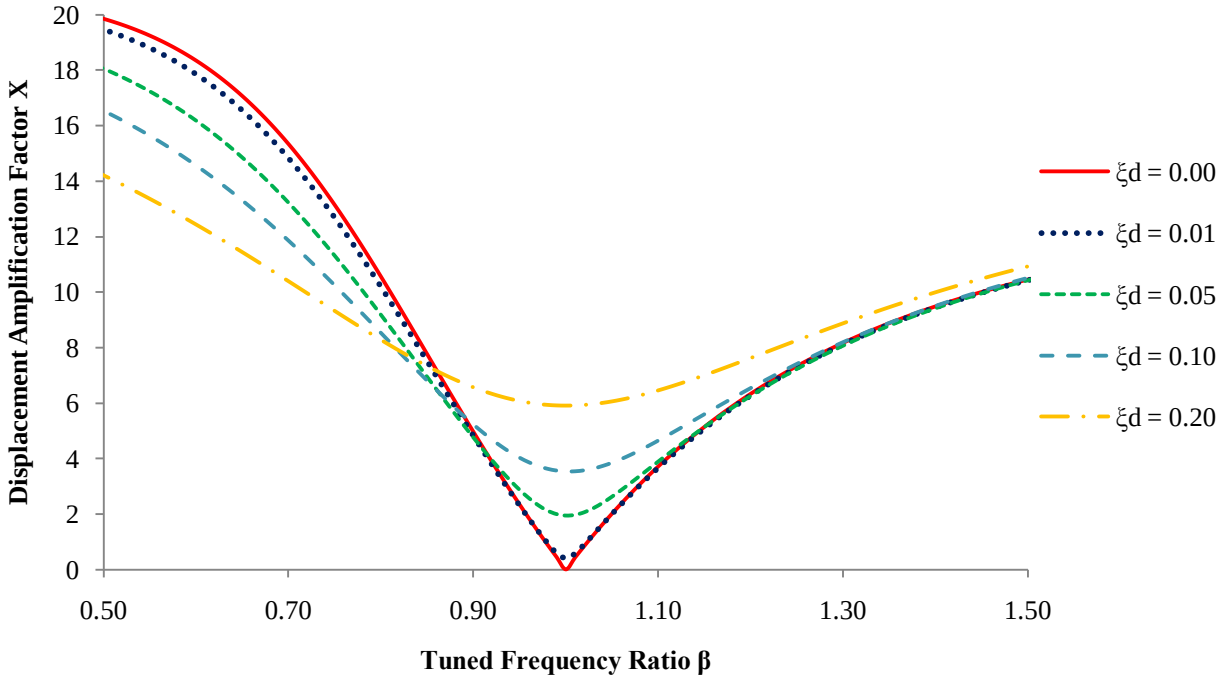

Figure 24: Displacement amplification factor X vs. Tuned frequency ratio for changing PTMD damping ratios

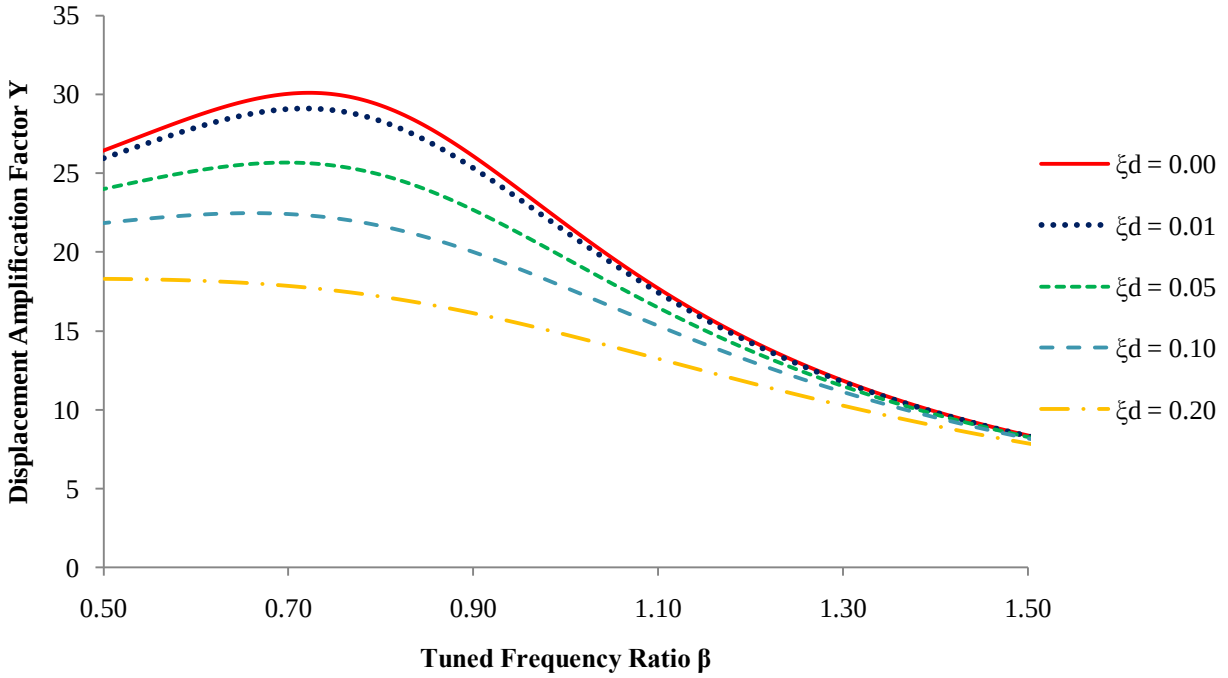

Figure 25: Displacement amplification factor Y vs. Tuned frequency ratio for changing PTMD damping ratios

Finally, the performance of the PTMD system will be evaluated for a changing excitation frequency. Let the PTMD be tuned to the structure's natural frequency ($\beta = 1$). The mass ratio is assumed to be 0.046 and the structure's damping ratio is 0.024. Figure 26 illustrates the effect of changing the structural excitation frequency ratio on the structure's displacement amplification factor for several PTMD damping ratios. The results show that the response is minimized when the structure is excited at its natural frequency. For the resonant condition, the minimum displacement occurs when the PTMD damping ratio is 0. However, when $\xi_a = 0$, there are two very large peaks in the structure's amplification factor symmetrically located about the resonant frequency. The effect of increasing the damping reduces these peaks while increasing the response at the resonant frequency. The peaks eventually merge if the PTMD damping ratio is increased to a sufficient level. In real applications, the structure is likely to be excited at a range of frequencies instead of a singular frequency. Therefore, the PTMD should minimize the response at its resonant frequency and at frequencies surrounding the resonant frequency.

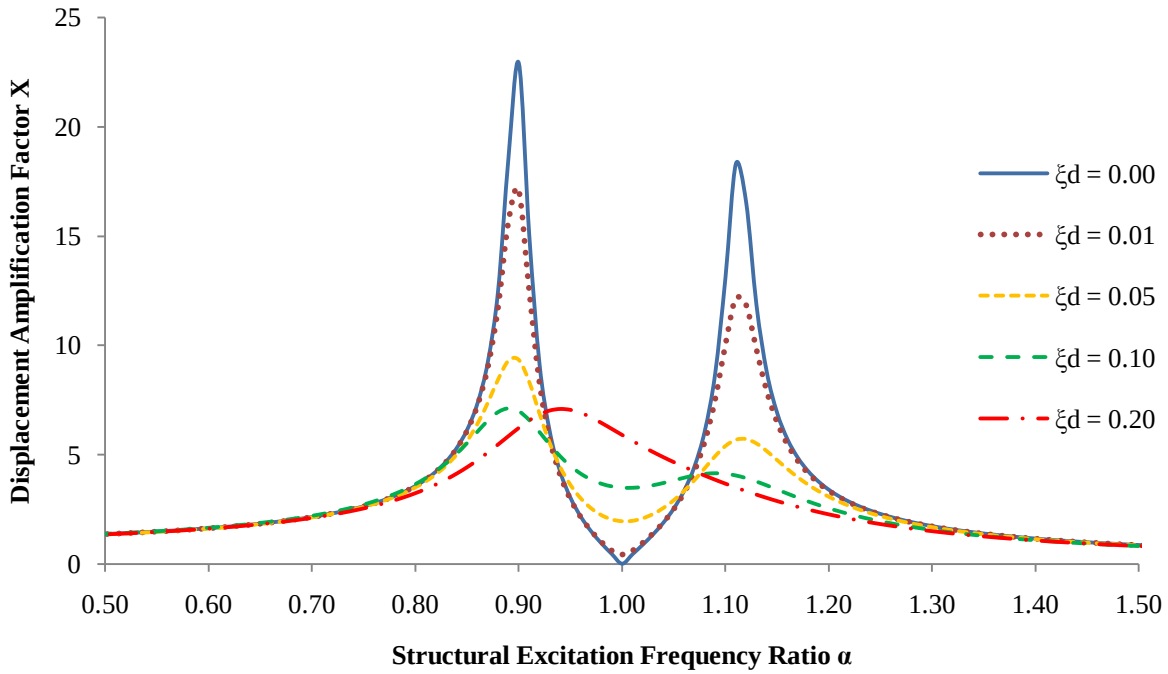

Figure 26: Displacement amplification factor X vs. Structural excitation frequency ratio for changing PTMD damping ratios

3.3 Evaluation of the Optimal PTMD System

The optimal PTMD system is the selection of optimal values for the controllable PTMD parameters based on pre-determined performance criteria. The performance criteria are a combination of system limitations used to evaluate different PTMD designs. Since the definition of performance criteria is open ended, there can be numerous different optimal designs. The performance criterion used here will be the minimization of horizontal displacement of the structure mass.

The simulation of different PTMD conditions confirms that the resonant response of the structure mass will approach zero as the PTMD dampening ratio approaches zero. However for frequencies away from the resonant conditions the response is significant. In practice, the bandwidth of the excitation frequency is likely to include a range of frequencies. Therefore, the minimization of horizontal displacement of the structure mass will be determined by comparing the maximum structure displacement amplification factor (X) for each set of controllable PTMD parameters (β, ξ_d, and $\bar{m}$) when the structure is excited by a periodic excitation with a structural excitation frequency ratio ranging from 0 to 2.

The evaluation algorithm used is an exhaustive search algorithm. The algorithm, which is discussed in Appendix B, calculates the maximum amplitude of X for a range of controllable PTMD parameter values defined in Table 4. The resolution of each parameter range is 0.001. The output of the algorithm is a square matrix containing the minimum peak amplitude of X and its corresponding β_{opt} for each possible combination of $\bar{m}$ and ξ_d within their respective value range. The optimal parameter set corresponds to the minimum value within the output matrix.

$\bar{m}$	0.0 to 0.3
ξ_d	0.0 to 0.2
β	0.75 to 1.25

Table 4: Controllable PTMD parameter value range

The results of the optimization algorithm are shown in Figure 27 and Figure 28. The optimal parameter values are $\bar{m}_{opt} = 0.3$, $\xi_{d\,opt} = 0.2$, and $\beta_{opt} = 0.774$. This is the boundary values for $\bar{m}$ and ξ_d. Beyond these boundary values the minimum peak X will drop even lower. However, mass ratios at this magnitude are unrealistic. Therefore the optimized PTMD system must have an upper bound on the mass ratio.

Figure 28 suggests that the optimal tuned frequency ratio is strongly influenced by the selected mass ratio. Figure 29 illustrates the relationship between the mass ratio and its corresponding optimal tuned frequency ratio for different PTMD damping ratios. This relationship can be represented by a polynomial function (i.e. linear or quadratic). Note that the curves converge for PTMD damping ratios above 0.03. This suggests that the optimal conditions become highly dependent on the mass ratio for PTMD damping ratios above 0.03.

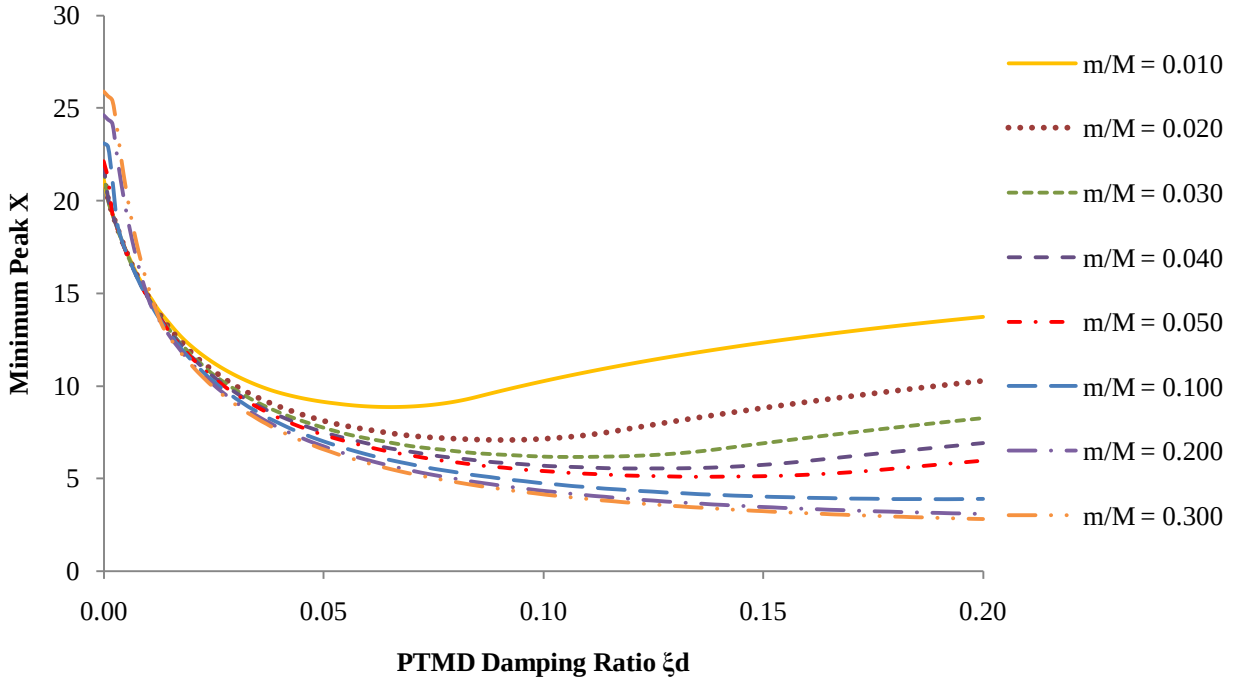

Figure 27: Minimum peak displacement amplification factor X vs. PTMD damping ratio for changing mass ratio

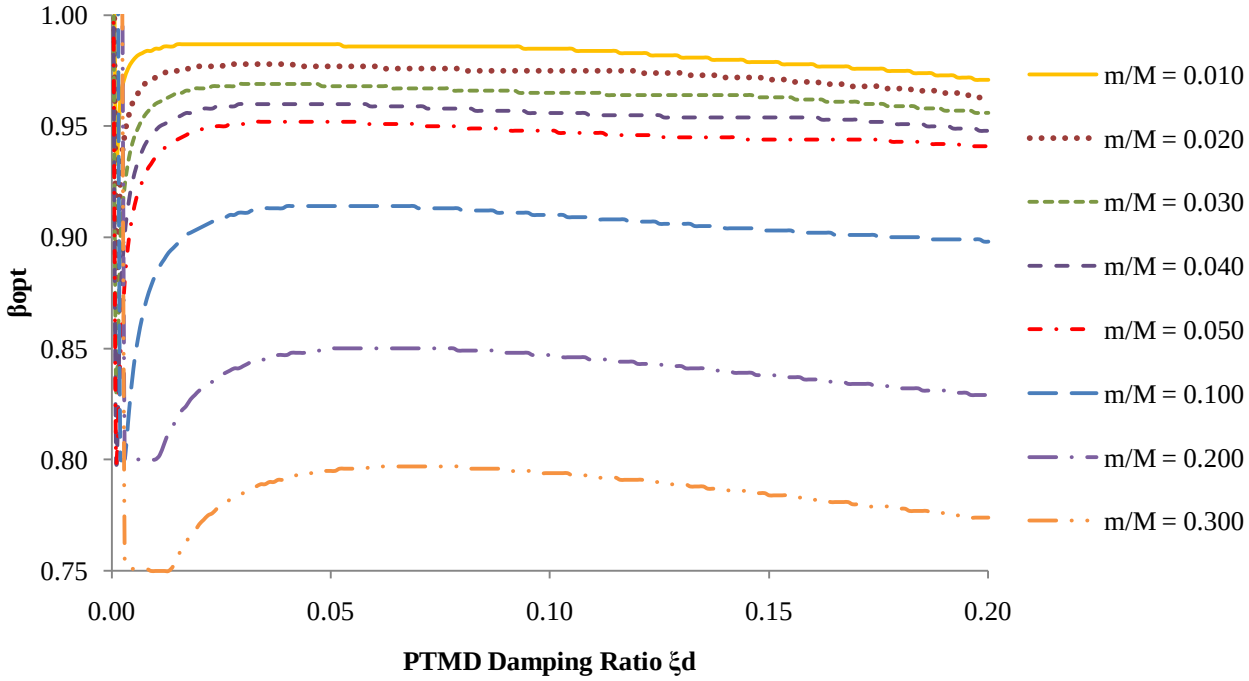

Figure 28: Optimal tuned frequency ratio vs. PTMD damping ratio for changing mass ratio

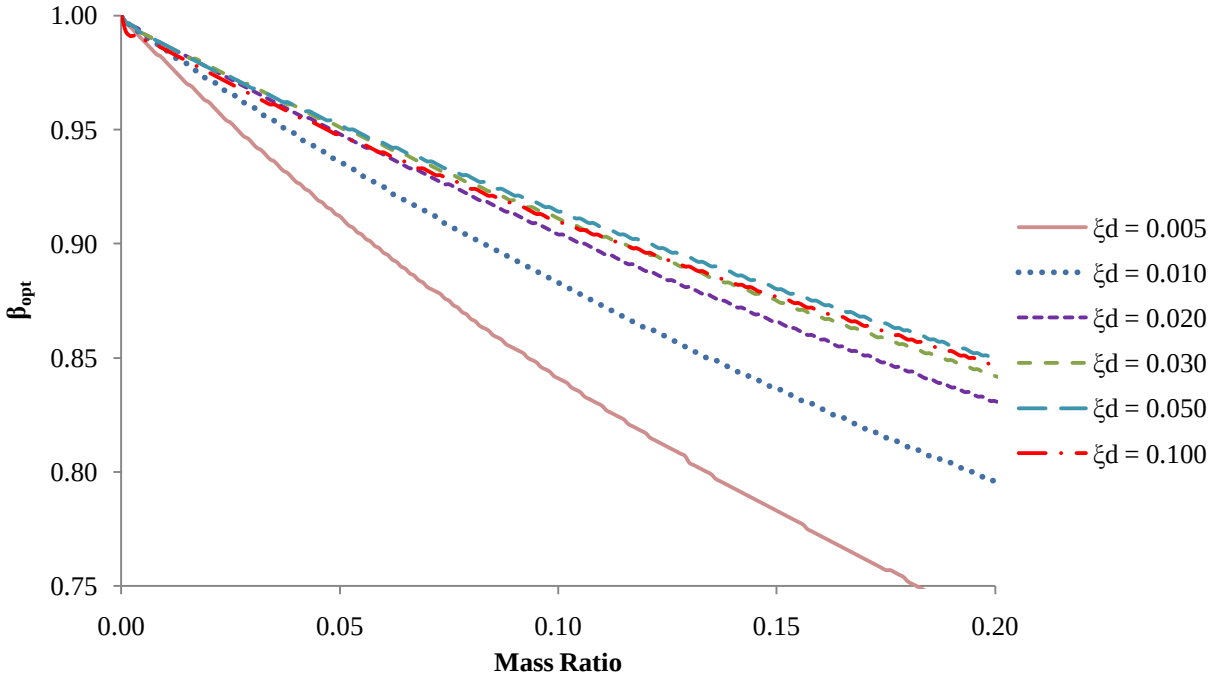

Figure 29: Optimal tuned frequency ratio vs. Mass ratio for changing PTMD damping ratio

The optimal PTMD system will have an upper bound mass ratio of 0.046, as determined by the constraints in the laboratory setup. The results of the optimization analysis given the upper bound constraint on the mass ratio are presented in Figure 30. The results indicate that near optimal results can be obtained when the PTMD damping ratio is between 0.085 and 0.185 and the PTMD tuned frequency ratio is between 0.925 and 0.975. It can be concluded that performance improvements are more heavily dependent on the PTMD tuned frequency ratio. The corresponding optimal parameter values are $\bar{m}_{opt} = 0.046$, $\xi_{d\ opt} = 0.130$, and $\beta_{opt} = 0.949$. Figure 31 and Figure 32 shows the structure's displacement amplification for the optimized system and several detuned systems under a wide spectrum of excitation frequencies. The optimized system does not minimize X when the structure is excited at its natural frequency. It does however minimize the peak displacement amplitude for both the structure mass and the pendulum mass.

Using the optimal non-dimensional PTMD parameters ($\beta_{opt}, \xi_{d\ opt}$, and $\bar{m}_{opt}$) and the expressions in Table 3; the optimal pendulum length (L_{opt}), pendulum mass (m_{opt}), and external dampening coefficient (d_{opt}) can be determined. The optimal dimensional PTMD parameters are shown in Table 5.

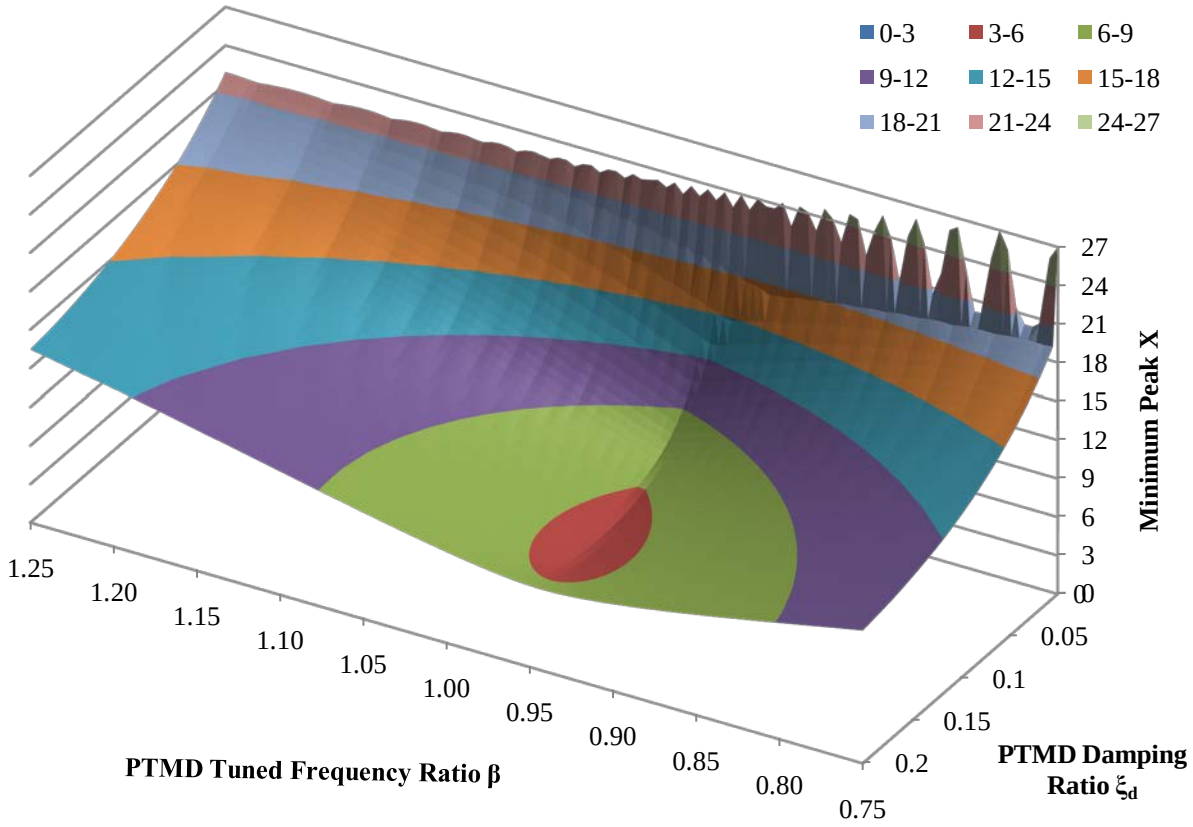

Figure 30: Minimum peak displacement amplification factor X vs. β and ξ_d for $\bar{m} = 0.046$

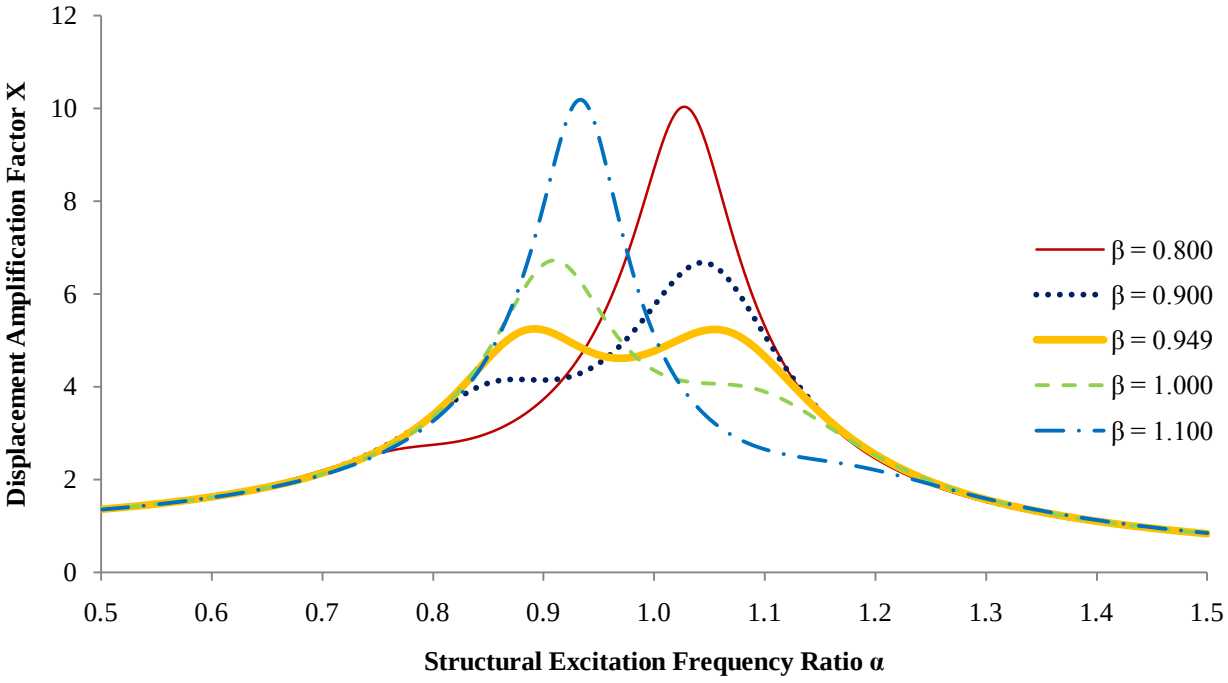

Figure 31: Displacement amplification factor X vs. Structural excitation frequency ratio for multiple tuned frequency ratios

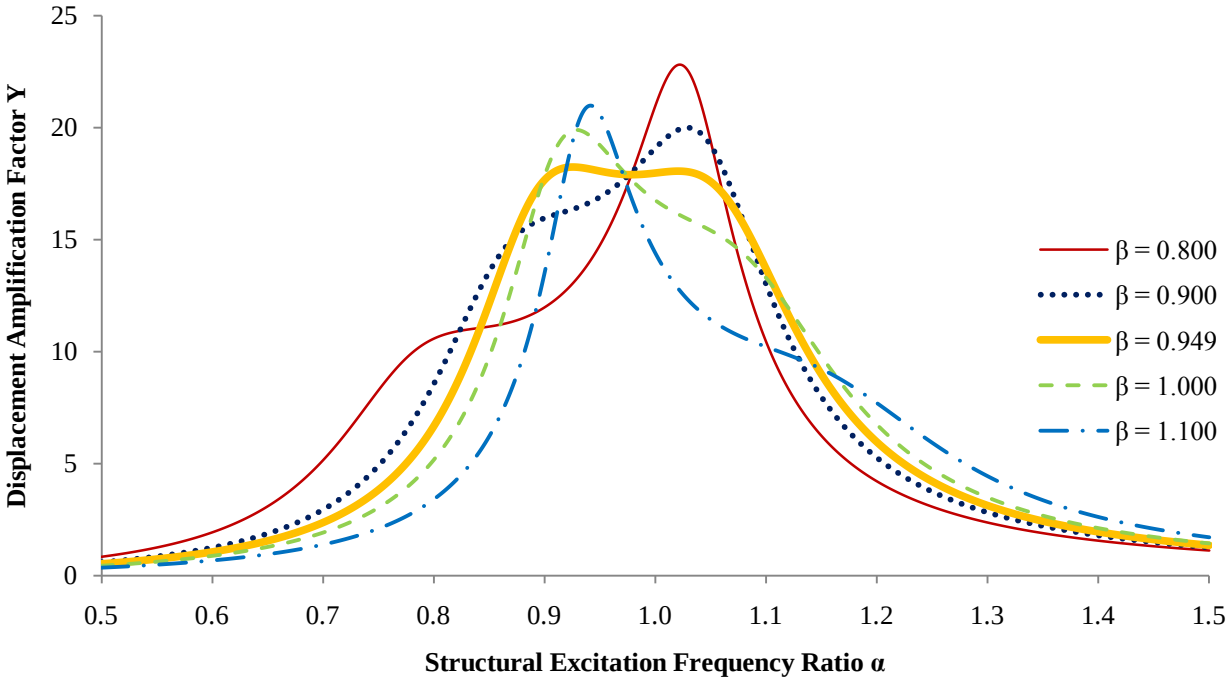

Figure 32: Displacement amplification factor Y vs. Structural excitation frequency ratio for multiple tuned frequency ratios

L_{opt}	80.14 mm
m_{opt}	1.47 kg
d_{opt}	0.00312 N/(mm/s)

Table 5: Optimal dimensional PTMD parameters

Figure 33 compares the response of the structure with and without the optimal PTMD system when the structure is subjected to an excitation force with amplitude of 2.5 Newton at a frequency equivalent to the structure's natural frequency. The simulated response shows a 77.06% decrease in the deflection of the structure when the optimal PTMD is applied. Note that there is an 84.9° difference in phase between the pendulum mass and structure mass.

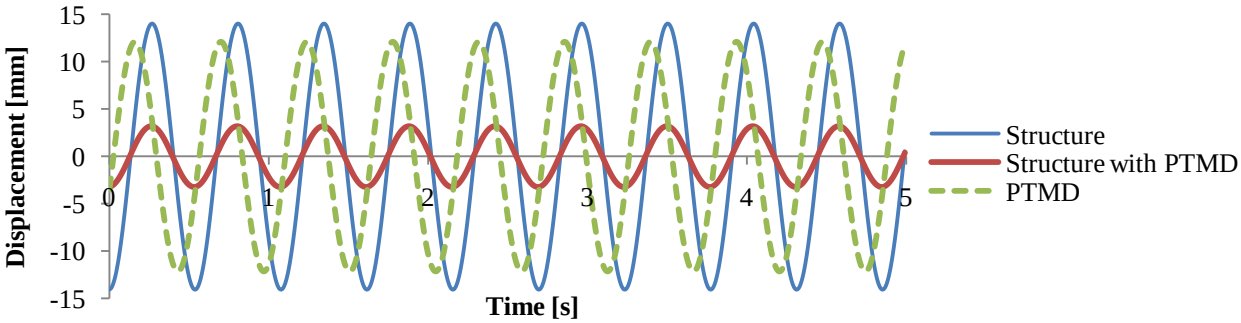

Figure 33: Structure and PTMD response to input excitation

Chapter 4: Experimental Setup

The experimental setup consists of a prototype APTMD mounted onto a test structure. The test structure is then subjected to an input excitation force. Measurement devices are used to measure the structure's response to the excitation. Based on the structure's response, the prototype APTMD can adjust its tuning parameters. The successive sections of this chapter describe the design and capabilities of the prototype APTMD and the test structure.

4.1 Two-Storey Building Structure and Apparatus

The two-story building structure test setup is similar to conventional modal testing apparatus. The setup, as depicted in Figure 34, consists of a signal generator, excitation mechanism, sensing mechanism, test structure, and post-processing analysis tools. The testing process is as follows: the signal generator provides a control signal for the excitation mechanism to excite the two-storey test structure. Acceleration sensors mounted to the structure measure the structure's response. Finally, post-processing analysis identifies the corresponding Frequency Response Function (FRF). Adaptive compensation of the TMD parameters is based on the identified dominant modal frequencies of the structural system.

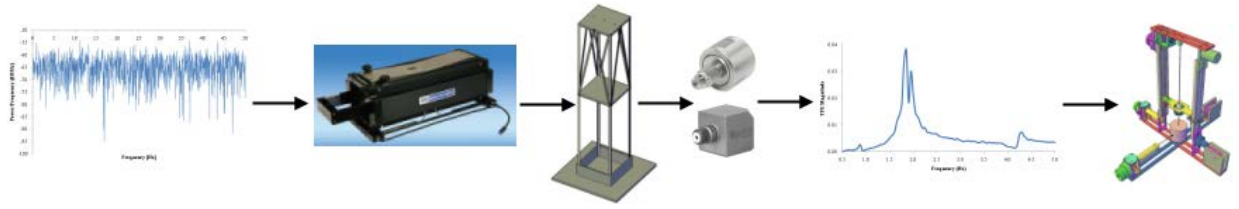

(a) (b) (c) (d) (e) (f)

Figure 34: Modal testing setup containing (a) signal generator, (b) excitation mechanism, (c) test structure, (d) sensing mechanism, (e) FRF, and (e) APTMD

4.1.1 Two-Storey Building Structure

The two-storey test structure consists of two floor masses supported by beams and columns. Each floor mass has a weight of 140 N and is constructed from a solid slab of cold-rolled steel. The vertical L-shaped support beams are constructed from 6061 aluminum alloy with a flange width and thickness of 1.27 cm and 0.16 cm, respectively. The vertical separation of each floor is

68.58 cm. Additional truss members constructed from 6061 aluminum alloy are braced between the upper two floors to reduce the torsional moment at the top floor. A 0.635 cm neoprene mat inserted between the base and the floor is used to dampen any undesirable vibrations which may be transmitted to the test structure. A three-dimensional conceptual drawing of the two-storey building structure is shown in Figure 34. Refer to Appendix D for additional drawings.

The selection of a two-storey structure allows for the ability to excite multiple structural masses. When excited under general dynamic loading, the overall response of the structure will be a combination of several lateral and torsional modes. The existence of several frequencies will introduce complexity in the estimation process, which will be described later. This is reflective of the spectral identification for real structures.

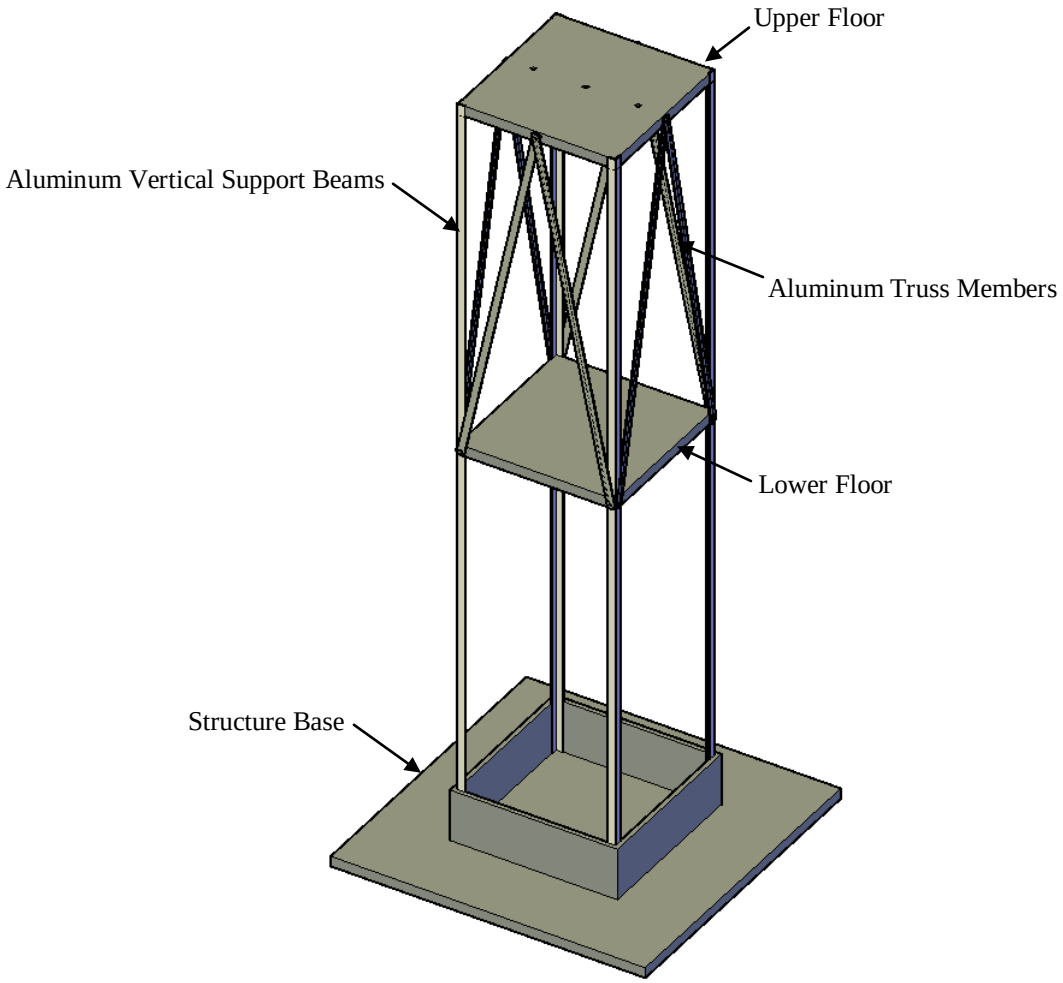

Figure 35: Two-storey building structure

4.1.2 Excitation Mechanism

A shaker is used as the excitation mechanism for the two-story building structure test set-up. The selected shaker is an APS 113-AB shaker. The maximum output force supplied by the shaker is 133 N with a frequency range of 0 Hz to 200 Hz. Refer to Appendix C for a complete datasheet. Shakers are traditionally used for modal testing because they are simple to implement and allow for various input excitation signals. The shaker is rigidly attached to a stand which sits on the floor. A 0.635 cm neoprene mat inserted between the floor and the stand absorbs the vibration induced by the motion of the shaker armature mass.

A major issue in modal testing is the manner of attachment of the shaker to the test structure. There is an inherent structure-shaker interaction, where the structure imposes its own dynamic behaviour on the shaker armature mass and vice versa. A result of such an interaction is a force drop-off that occurs at and around the structure`s natural frequency (Varoto and de Oliveira 2002).

The attachment between the structure and shaker must transmit the shaker excitation force to the structure in the direction of motion of the shaker armature mass, while limiting motions that are not representative of actual conditions. In the presence of an excitation, the torsional response of the structure will cause it to twist about the vertical axis, while it responds in both transverse directions. A rigid attachment limits the natural twisting and orthogonal (to the line of action) responses.

A stinger is used to attach the shaker to the structure. A stinger is a flexible rod that allows for axial force transmission while allowing for any twisting and transverse misalignment between its two ends. The stinger used in the test setup is a 3 mm diameter threaded steel rod with a length of 178 mm. Due to its flexibility, the stinger will act as a mechanical fuse in case of any excessive force from the shaker. Figure 36 illustrates how the stinger attaches the structure to the shaker. Note that the force transducer is rigidly attached to the structure. This allows the force transducer to measure the input force to the structure without having to account for the dynamics of the stinger. A three-dimensional conceptual drawing of the two-storey building structure with the shaker is shown in Figure 37.

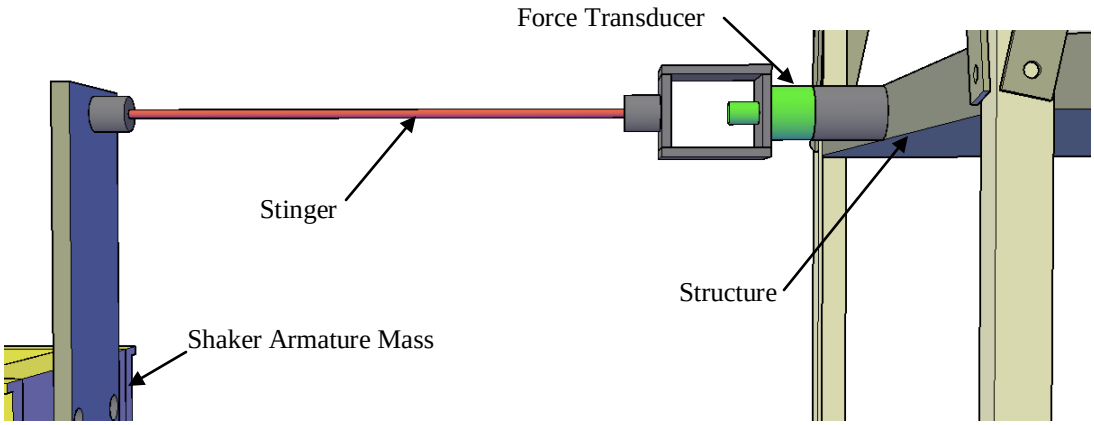

Figure 36: 3D perspective of stinger assembly

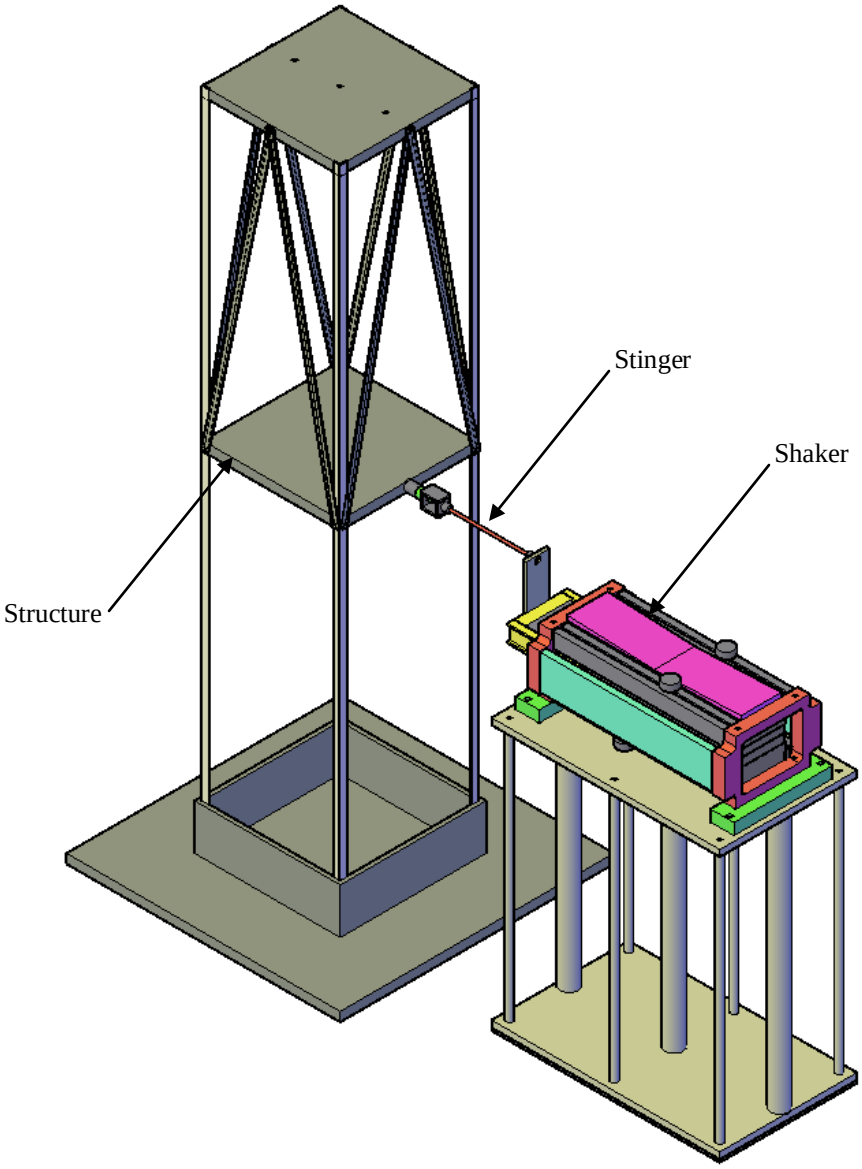

Figure 37: Two-storey building structure excited by shaker

4.1.3 Signal Generation, Identification and Sensing Mechanism

Both the signal generation and identification algorithms are handled using a dSPACE 1104 Digital Signal Processing (DSP) control and data acquisition board. The dSPACE 1104 board contains eight 16-bit digital-to-analog output channels, eight 16-bit analog-to-digital input channels, and 48 digital input/output channels, all of which operate between 0 to 10 volts. Two on-board processors and built in memory allow the dSPACE 1104 board to operate as an independent system, allowing for real-time measurements and identification. A PCI interface allows for the dSPACE 1104 board to operate with MATLAB Simulink software. As a result, the signal generation, identification, and TMD parameter control are implemented with Simulink objects.

Accelerometers mounted in orthogonal directions on each floor of the two story test structure are used to measure the structural response to the input excitation. The accelerometers, which are manufactured by PCB Piezoelectronics (model 333B40), measure the floor acceleration along a single direction. The selected accelerometers have a frequency range between 0.5 Hz and 3000 Hz with sensitivity of approximately 500 mV/g. Refer to Appendix C for the complete datasheet on the accelerometers used in the experiment. The measured accelerometer signals are fed into a four channel ICP-sensor signal conditioner. The signal conditioner, manufactured by PCB Piezoelectronics (model 442C04) yields four alternating current (AC) coupled output signals with an adjustable voltage gain of 1, 10, or 100 times the original output voltage. Simply, the signal conditioner outputs a voltage signal compatible with standard readout instruments. The output signals are fed into the dSPACE analog input ports where they are calibrated to output the floor acceleration. Note that each accelerometer is calibrated based on its factory calibrated settings.

A force transducer is used to measure the input excitation force to the structure. The selected force transducer is a piezoelectric force sensor manufactured by Dytran (model 1050V1). The selected force transducer has a sensitivity of 463.8mV/LbF and can measure compression and tension loads along a single axis. Refer to Appendix C for the complete datasheet. The measured force transducer signal is fed into a single channel signal conditioner manufactured by Dytran

(model 4110C). The output signal is then fed into a dSPACE analog input port, where it is calibrated based on factory settings to output the input force.

4.2 Prototype Design

The prototype APTMD is shown in Figure 37. The prototype consists of a 1.47 kg suspended mass, two damping assemblies mounted orthogonally to the suspended mass, and a tuning assembly. Refer to Appendix D and E for additional drawings and images. The damping assembly adjusts the damping ratio of the APTMD by changing the viscous damping coefficient of the damper mounted to the pendulum mass. The tuning assembly tunes the APTMD to the lowest modal frequency by identifying the dominant frequencies in the structure response and adjusting the pendulum arm length accordingly. Detailed discussions of both assemblies are provided in the subsequent sections.

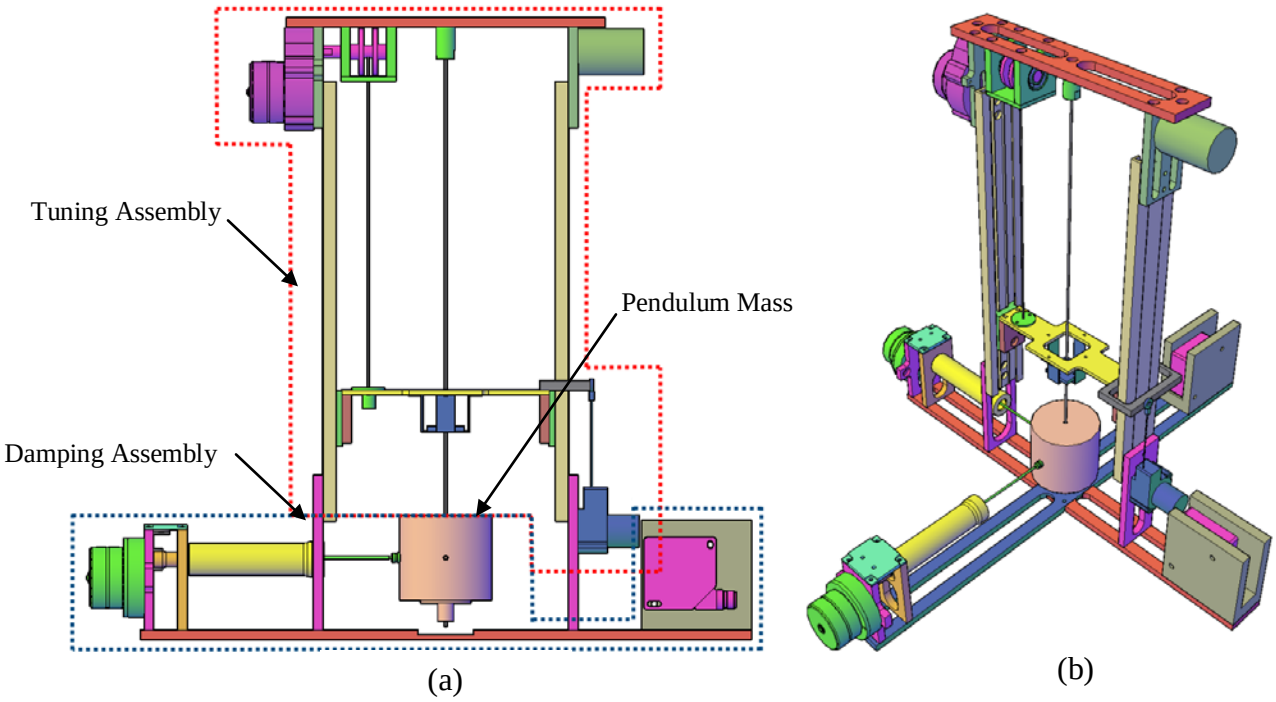

Figure 38: Prototype APTMD (a) side perspective (b) 3D perspective

4.2.1 Damping Assembly

A key component in the APTMD system is the damping assembly. This consists of an external damper connected to the suspended pendulum mass. The mechanical energy of the suspended mass is dissipated through this air damper. The level of damping in the damper is adjustable via a valve. The details of the assembly are described next.

A controllable external damper requires an adjustable damping device and a mechanism to adjust it. The selected external damper is an Airpot 2K160 air damper. The air damper contains an adjustable valve, capable of adjusting the damping coefficient between 0 to 880 N/(m/s) with a maximum pull and push load of 18 N and 13 N, respectively. Refer to Appendix C for the complete datasheet. Two dashpots are utilized. The air dampers are mounted parallel and perpendicular to the direction of excitation provided by the shaker. A ball joint on each air damper allows the air damper to be rigidly attached to the pendulum mass while permitting the pendulum mass to move freely.

The components of the damper assembly are shown in Figure 39. The main components of the damper assembly include an adjustable air damper, a stepper motor, which turns the adjustable air damper valve, and a Hall Effect sensor to measure the rotational position of the valve. The stepper motor used in the design is a 12V geared bi-polar stepper motor manufactured by Portescap and is capable of providing 0.211 Nm of torque at a rated speed of 240 PPS. The selected Hall-Effect sensor is a miniature mount Hall-Effect sensor manufactured by Hamlin. Refer to Appendix C for the complete datasheet for the selected stepper motor and Hall Effect sensor. The Hall Effect sensor measures the flux induced by a changing magnetic field. Using two miniature earth magnets mounted ½ revolution apart on the coupler, the Hall-Effect sensor acts as an optical encoder which, when calibrated, can be used to determine the rotation of the air damper valve.

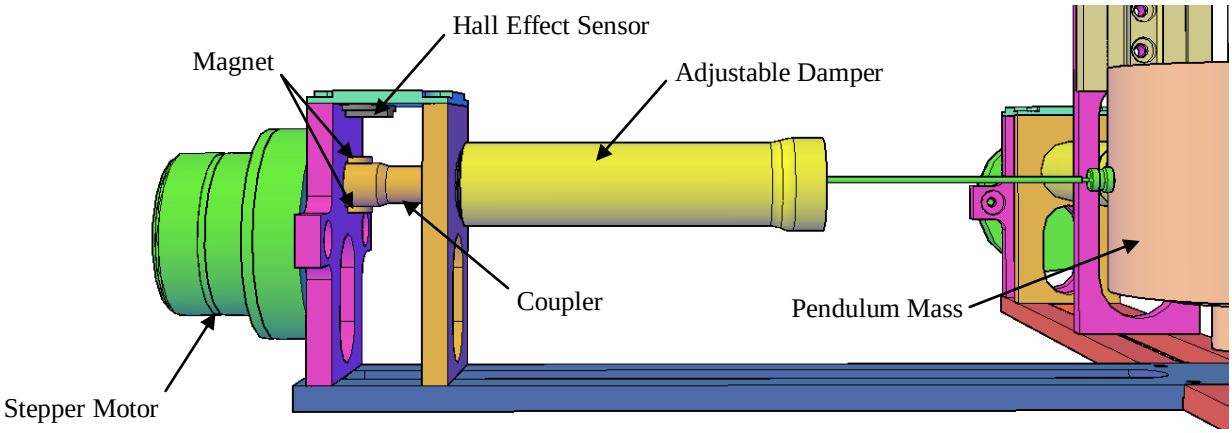

Figure 39: 3D perspective of damper control assembly

4.2.1.1 Stepper Motor Control

The geared bidirectional stepper motor contains a 12 tooth central rotor surrounded by four stator coils with an external gear ratio of 10:1. To actuate the stepper motor the coils are energized in a 'full-step drive' sequence which is shown in Table 6. This method energizes two coils at each time step, providing additional torque at the expense of doubling the electrical current requirements. To move the rotor in the opposite direction, the sequence is reversed.

	Time Sequence			
Coil	**T**	**T+1**	**T+2**	**T+3**
1A	High	High	Low	Low
1B	Low	Low	High	High
2A	Low	High	High	Low
2B	High	Low	Low	High

Table 6: Full-Step drive

The stepper motor is interfaced to the dSPACE control board through an in-house built controller. The stepper motor control board can control up to three stepper motors and contains six digital inputs: three direction inputs and three step inputs. The direction input indicates the direction of rotation of the stepper motor. The step input indicates when the stepper motor advances a step. For example, if the digital step input goes from low to high (or high to low) and the direction is set high while the current rotor position is at *T+1*, the rotor will advance to *T+2*. Conversely, if the direction is set low the rotor will advance to *T*. To complete a revolution the

dSPACE control board must supply 480 step signals, or 240 pulses. The rotational speed of the stepper drive shaft is determined by the time delay between successive step signals.

4.2.1.2 Valve Position Control

Ideally the open loop control scheme used to actuate the stepper motors would be used to open and close the damper valves. By simply providing the correct number of pulses to the stepper controller input channels the stepper motor would rotate to the desired angle. However the open loop control scheme is prone to errors due to misstepping, which can only be corrected by manual recalibration.

Thus, a hysteresis controller is used to control the angular valve position of the dampers. A hysteresis controller is a feedback controller that switches between two states. For the purpose of controlling the angular valve position the two states are 'motor on' and 'motor off'. For the 'motor on' state the valve position controller outputs a pulse train to the step input of the stepper motor controller. Note that the rotational speed of the stepper motor is inversely proportional to the period of the pulse train (T), as per Eq. 4-1. For the 'motor off' state the valve position controller outputs low.

$$\omega_{motor} = \frac{\pi}{120T} \quad \textbf{(4- 1)}$$

Position feedback is provided by a Hall Effect sensor. The Hall Effect sensor signals high in the presence of a magnetic field, and low in the absence of a magnetic field. As a result the valve position controller can measure each half rotation of the damper valve. By defining a reference level and counting the level changes, the controller can determine when the adjustable valve is set to the desired position. This is referred to as a switch event. A switch event for a hysteresis controller is an event which triggers a switch between the two control states. When the valve is set to the desired position the state will transition from 'motor on' to 'motor off'. Alternatively when the desired valve position changes while the controller is at the 'motor off' state the controller will transition to the 'motor on' state. The state transitions are summarized in Figure 40.

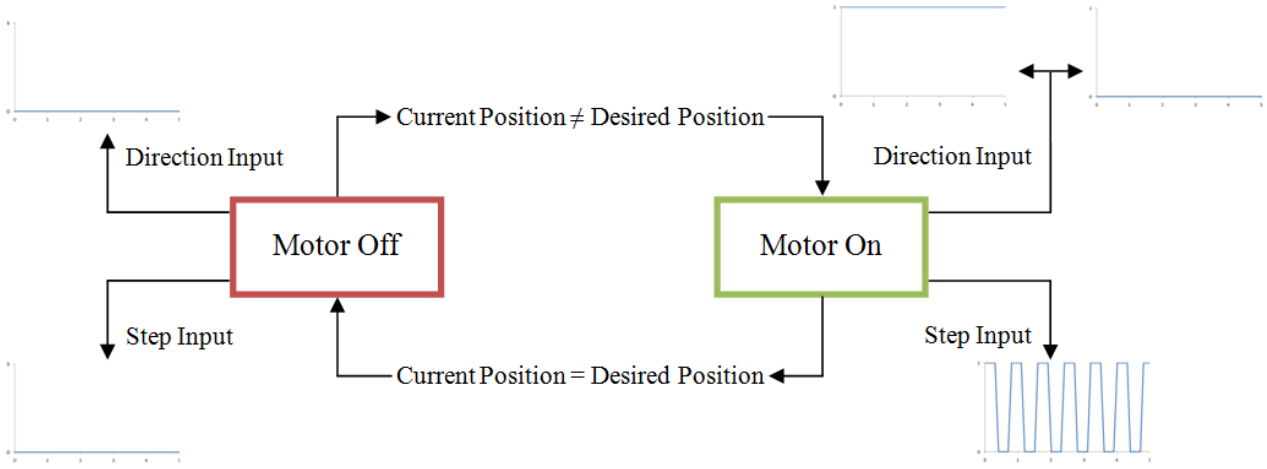

Figure 40: Valve position control state transition diagram

Eight valve positions have been defined for each damper. The first valve position is the closed valve position. At this position the damper exhibits the highest damping coefficient. Subsequent valve positions are half rotations in the counter clockwise direction from the closed valve position. The eighth valve position is the fully open valve position and exhibits the lowest damping coefficient.

4.2.1.3 Damper Calibration

The mathematical model proposed in Chapter 3 assumes that the damper is viscous. Viscous damping models are linear and time invariant. These models are preferred since they are simpler to solve analytically and simulate. However, real systems are never linear, and at best can be approximated by a linear system over a finite operating range. Alternatively, the model can utilize a non-linear function, such as Coulomb friction, to approximate the damping provided by the adjustable damper. Even for such cases, it is possible to compute an equivalent viscous damping coefficient. In any case, it is necessary to test the air dampers and determine its behaviour.

The equation of motion for a general second order mechanical system with viscous damping is given by Eq. 4-2. For a harmonic excitation force, the steady state response will be a harmonic function (Eq. 4-3). The energy dissipated per cycle by the viscous damper is given by Eq. 4-4. The dissipated energy is equivalent to the work done by the damper. The resultant equation for the damping coefficient is a function of the displacement and dissipation force (Eq. 4-5).

$$m\ddot{x} + c\dot{x} + kx = F(t) \quad \textbf{(4- 2)}$$

$$x_{ss}(t) = X sin\omega t \quad \textbf{(4- 3)}$$

$$\Delta E = \oint F_d dx = \int_0^{\frac{2\pi}{\omega}} c\dot{x}\frac{dx}{dt}dt = \int_0^{\frac{2\pi}{\omega}} c\dot{x}^2\, dt = \int_0^{\frac{2\pi}{\omega}} c(\omega X cos\omega t)^2\, dt = \pi c\omega X^2 \quad \textbf{(4- 4)}$$

$$c = \frac{\Delta E}{\pi\omega X^2} \quad \textbf{(4- 5)}$$

Given the displacement and dissipation force, Eq. 4-5 can be used to evaluate the equivalent viscous damping coefficient of the adjustable dampers for multiple valve positions. However the associated damper coefficient will only be accurate if the damper is viscous. To assess whether the damper is viscous the resultant damper response to an input harmonic driving force will be considered. If the response to a harmonic forcing function is harmonic then it can be concluded that the system can be modelled as linear for the given testing conditions. Furthermore if the measured force and displacement histories are approximately 90° out of phase, then it can be concluded that the damper dissipation force is proportional to the velocity and consequently the damper is viscous.

Each damper was calibrated offline. To calibrate the adjustable air dampers, one end was fixed while the other end was connected to the shaker. A load cell was mounted between the shaker and damping rod and was used to measure the damping force. The position of the damper piston was measured with a non-contact laser transducer. The laser transducer is manufactured by Hoskin and has a measurement range between 40 and 160 mm. Refer to Appendix C for the accompanying datasheet.

The calibration procedure was conducted for eight valve positions. For simplicity, the valve positions are referred to as Level 0 to Level 7, where Level 0 represents the highest damping resistance and Level 7 represents the lowest damping resistance. At each valve position the damper was excited by a harmonic excitation force with a frequency ranging from 110% to 80% (in 5% increments) of the identified natural frequency of the structure (1.855 Hz). The tests were conducted at a sampling rate of 100 Hz over a measurement period of 10 seconds.

Figure 41 presents the dissipation force and piston displacement relationship for multiple valve positions when the damper is excited by a 1.855 Hz harmonic motion. Not surprisingly the largest curves are obtained as the valve position approaches the closed position. The exception is the comparison between the Level 0 and Level 1 valve position, where the Level 1 valve position is larger. When the damper valve is sufficiently closed the damper will behave as a spring. This is likely due to the air stiffness within the damper barrel. The curves themselves are elliptical and the phase difference between the measured displacement and force for each curve is close to 90°. This indicates that the dissipation force is proportional to the velocity of the air damper piston.

The estimated damping coefficient for each forcing frequency is shown in Table 7. There is a significant difference in the estimated damping coefficients as the excitation frequency moves from 1.484 Hz (β = 0.80) to 2.041 Hz (β = 1.10). For valve position Level 0 to Level 3 the damping coefficient decreases as the frequency increases. For the remaining valve positions the change is minimal. This indicates that the damping coefficient may be a function of the excitation frequency. Based on the optimized damping conditions obtained in Chapter 3, the optimal valve position should be Level 7.

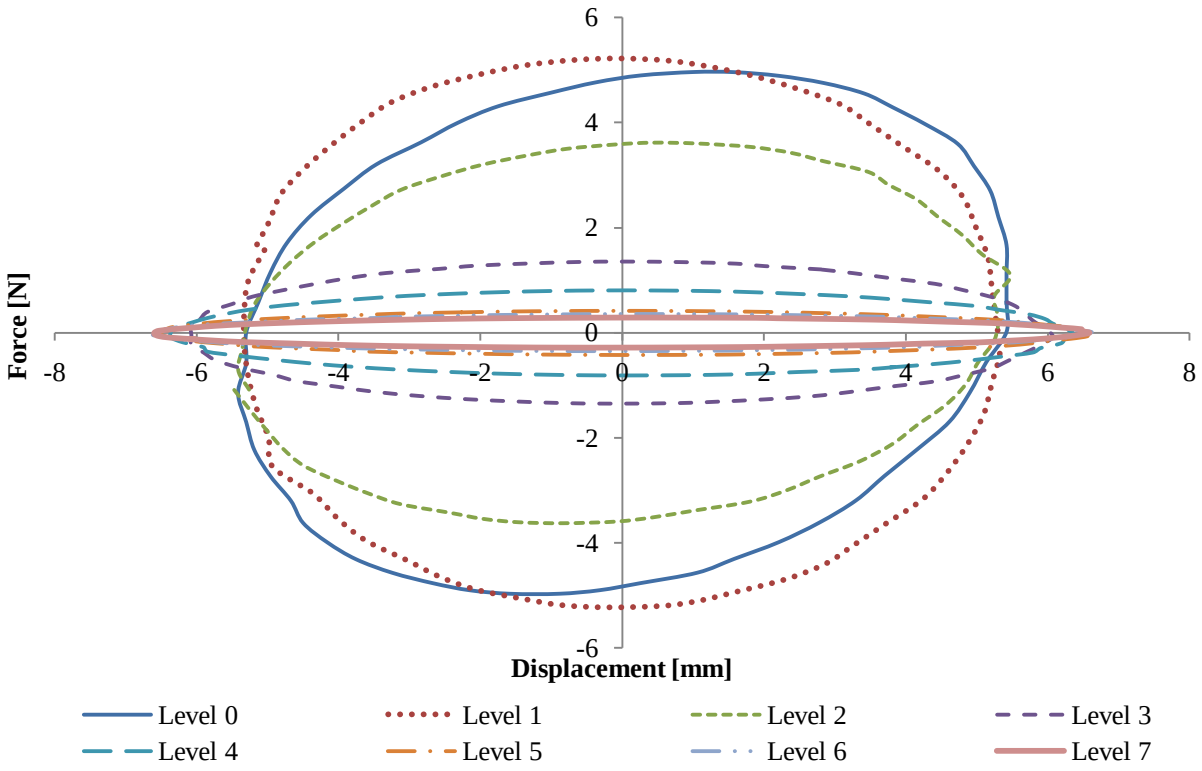

Figure 41: Force vs. Displacement for adjustable damper under harmonic excitation at β = 1.0 (1.855 Hz)

Damping Level	Damping Coefficient [N/(m/s)]						
	β = 0.80	**β = 0.85**	**β = 0.90**	**β = 0.95**	**β = 1.00**	**β = 1.05**	**β = 1.10**
0	100.8718	97.8889	90.3139	85.5516	77.5248	76.2397	74.1424
1	102.3564	96.8858	94.9011	87.6114	85.4827	77.8683	76.3010
2	63.9997	63.4529	60.9247	60.7181	55.2018	56.5266	54.4963
3	18.3446	18.3059	19.1065	18.9856	19.0367	18.8327	19.0924
4	10.6911	11.1312	11.0436	11.2715	10.8482	11.1761	11.1658
5	5.2860	5.3975	5.2983	5.5748	5.4565	5.5370	5.5550
6	4.3113	4.7303	4.6753	4.5160	4.4875	4.6414	4.6627
7	3.4464	3.4104	3.7545	3.8610	3.7229	4.0665	4.1103

Table 7: Estimated damping coefficients for multiple valve positions

4.2.1.4 Desired Valve Position Control

Two control schemes are employed to control the valve positions of the dampers. A manual control scheme adjusts the damper valve position to a position defined by the user. An automated control scheme adjusts the damper valve position based on the motion of the pendulum mass. Both control schemes utilize the same control mechanism (using a Hall-Effect sensor) to adjust the damper valve position.

The automated control scheme is implemented as follows. The motion of the pendulum mass is tracked using two non-contact laser sensors mounted orthogonally in the horizontal plane. Using the known geometry of the system, the algorithm defines a line representative of the damper rod. The intercept of the line with the front end of the air damper is calculated. The orthogonal motion of the damper rod is defined as the distance from the current intercept to the intercept of the damper rod at rest. Figure 41 provides a representation of the geometry used in the algorithm. As the distance increases the desired damping coefficient increases. The algorithm then commands the damper valve controller to tighten the valve, effectively increasing the damping coefficient. In effect, the algorithm is designed to mitigate the possibility of the rod impacting with the outer walls of the damper by increasing the damping coefficient. Impacting of the piston rod with the damper walls creates irregularities in the motion of the pendulum mass.

Figures 43 to 45 illustrate the damping control parameters for the direction perpendicular to the excitation direction. The results correspond to a test with the shaker input being a random

Gaussian distributed excitation signal. The displacement curve shown in Figure 43 represents the orthogonal motion of the damper rod. The algorithm analyses 5 second windows to determine if the orthogonal motion exceeds thresholds represented by the dashed lines on the diagram. The results indicate that the displacement exceeds 1 mm at approximately 2, 13, and 15 seconds. For the remaining windows the maximum displacement exceeds 0.5 mm. The corresponding damping levels are level 5 and 6 respectively, as shown in Figure 44. Each dampening level corresponds to a damper valve position. The new valve position is updated using the desired damping level. Figure 45 shows the Hall Effect sensor output as the stepper motor updates the damper valve position. Note that each transition from low to high represents a transition between damper valve positions.

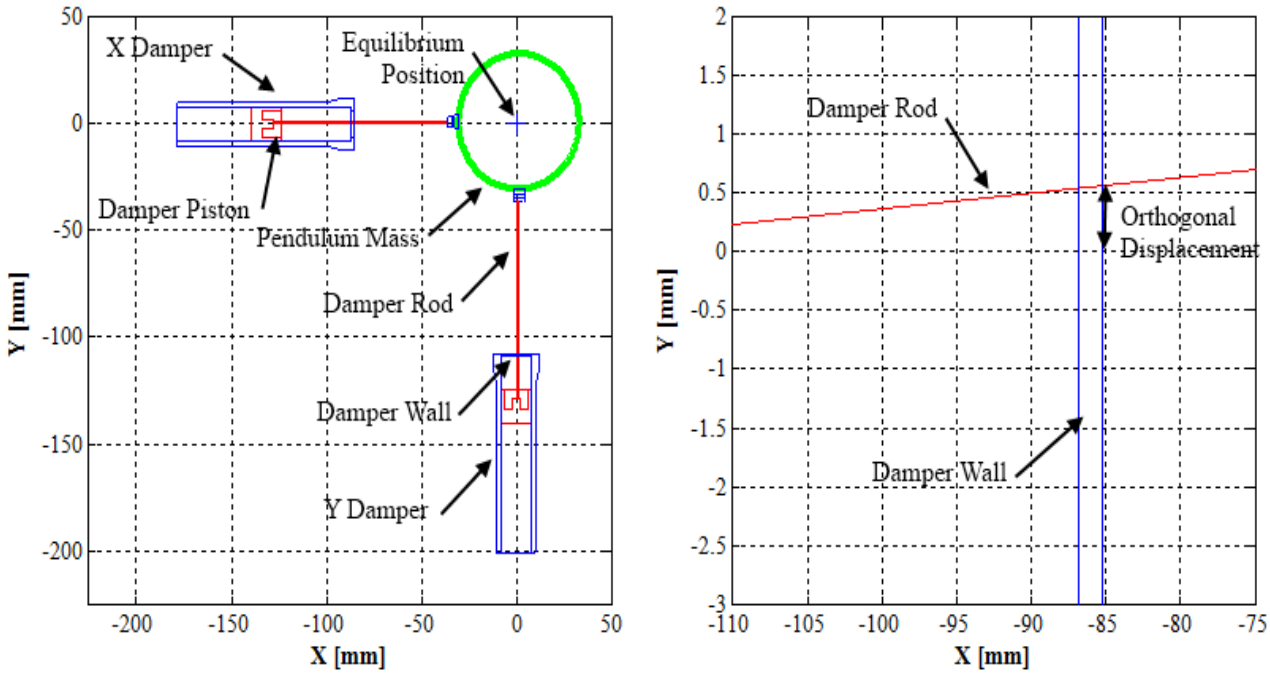

Figure 42: 2-Dimensional geometry of pendulum-damper motion

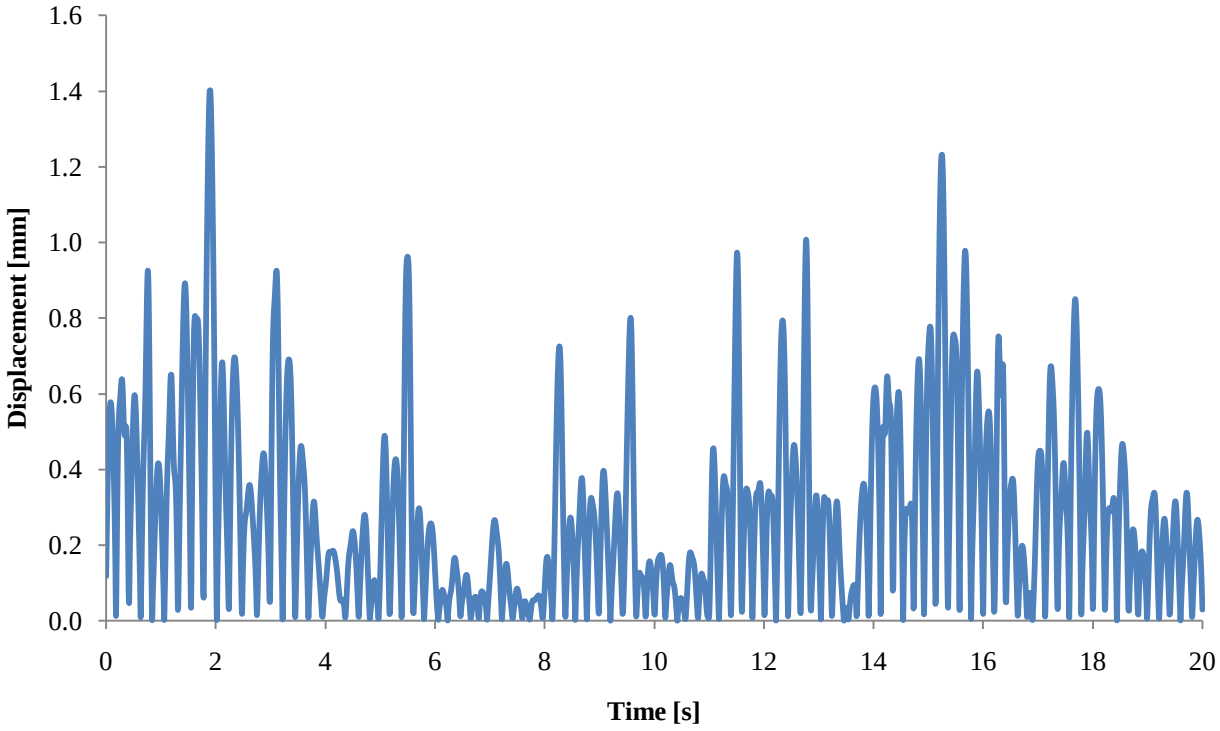

Figure 43: Orthogonal motion of the damper rod in the x-direction

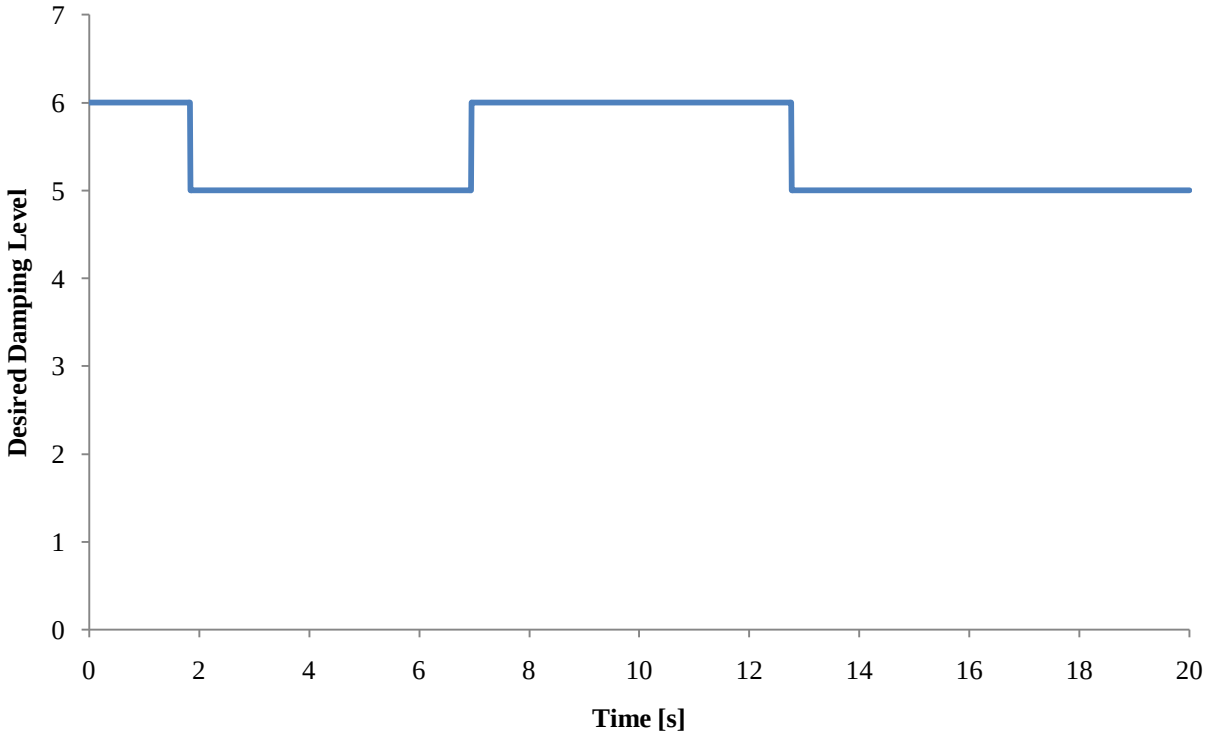

Figure 44: Desired damping level in the x-direction

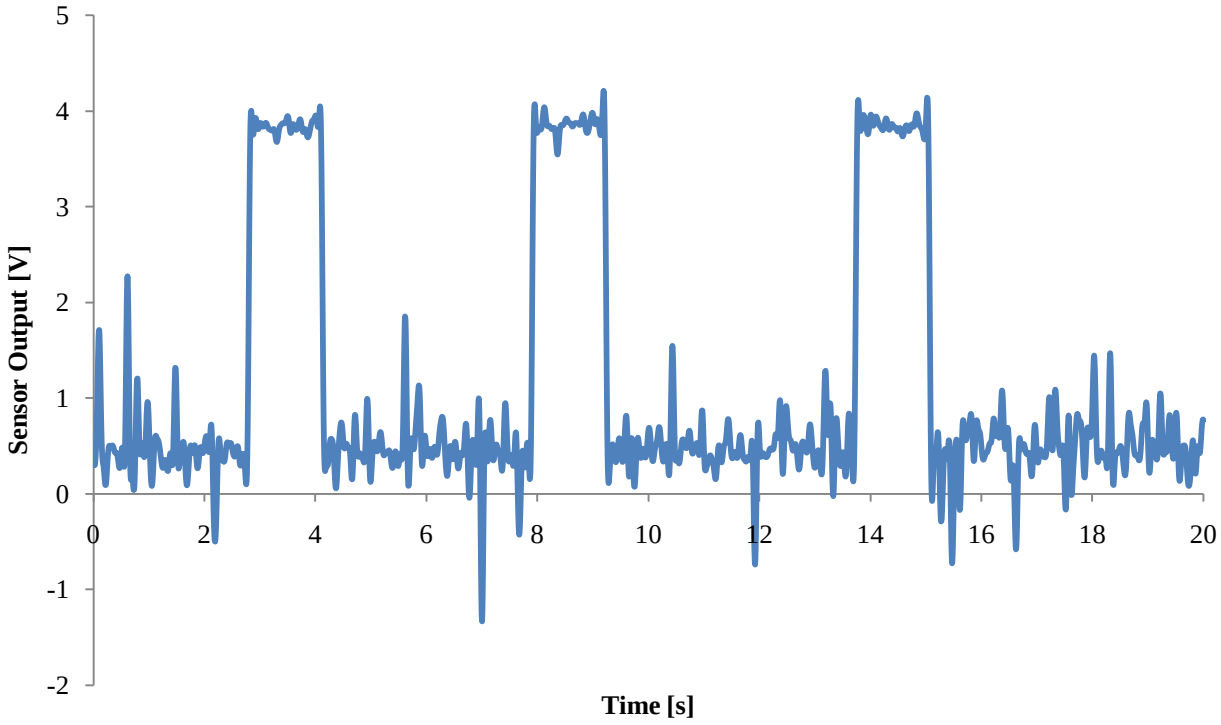

Figure 45: Hall Effect sensor output for damper in x-direction

4.2.2 Tuning Assembly

The tuning assembly adjusts the length of the pendulum to control the changes in the natural frequency of the APTMD. The design objective is to develop a system that is lightweight, low-cost, and low-maintenance. The design should also require minimum power, and capable of withstanding loads from the pendulum mass along with vibrations from the connected structure.

The proposed design, as presented in Figure 46, consists of a tuning frame mounted onto a pair of polytetrafluoroethylene (PTFE) lined guide blocks. Each guide block rides along a low profile, low friction anodized aluminum rail. PTFE is a soft material with a very low coefficient of friction. Combined with the anodized aluminum rail, the vertical motion of the guide block is smooth while allowing for misalignments caused by dynamic loading. The static load capacity of each rail is 698 N. This is well above the expected loading.

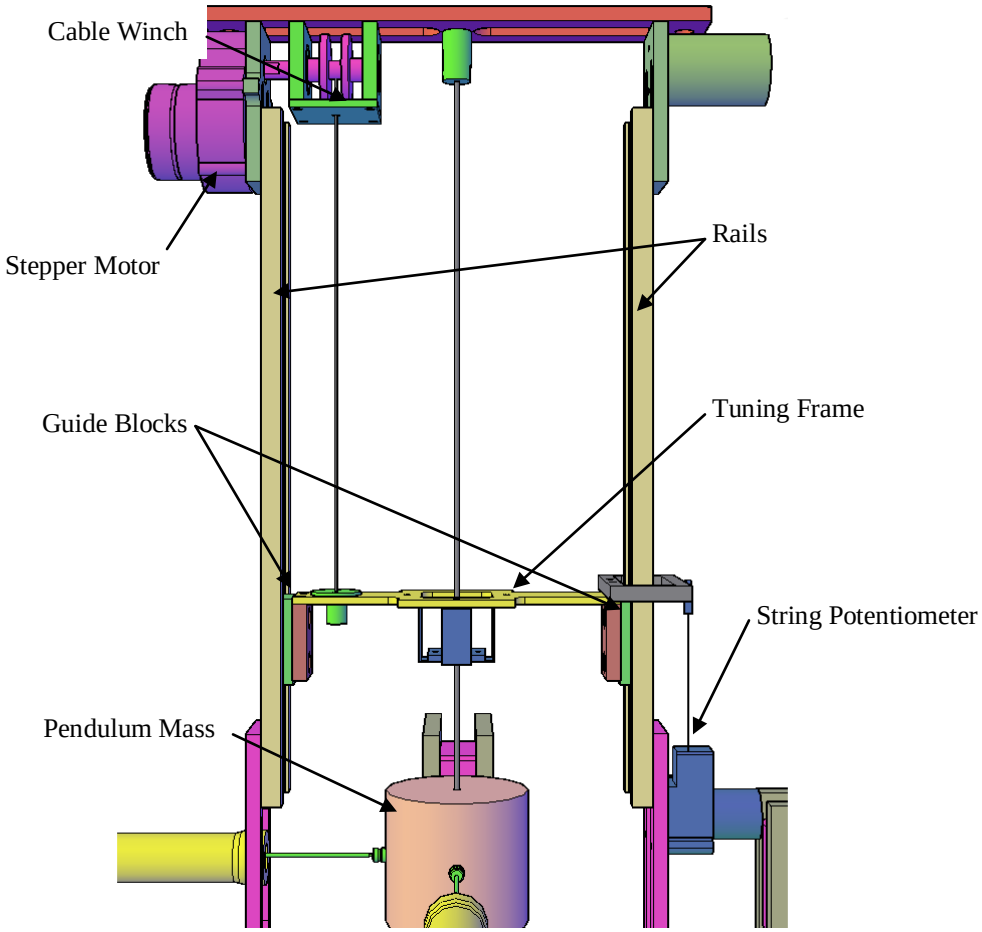

Figure 46: 3D perspective of tuning assembly

The tuning frame is hoisted vertically using a cable-winch assembly. A stepper motor is used to actuate the cable-winch. The selected stepper motor is a 5V geared bi-polar stepper motor manufactured by Portescap capable of providing 0.854 Nm of torque at a rated speed of 240 PPS. Refer to Appendix C for the complete datasheet. The minimum step angle of the stepper motor is 0.15°. Considering that the diameter of the attached spindle is 7.9375 mm, the resolution of the vertical position of the tuning frame is 0.0104 mm.

4.2.2.1 Vertical Position Control of Pendulum Arm Length

Vertical position control of the pendulum arm length is similar to the valve position control used in the damper assembly. A hysteresis controller is used to determine the output for the step output port, where the direction is based on the current and desired pendulum arm length. Feedback for the pendulum arm length is provided by a string potentiometer, which converts the

distance travelled by a reeled cable into an analog voltage. The selected string potentiometer is manufactured by Micro-Epsilon and has a measurement range of 0 to 150 mm. Refer to Appendix C for a complete datasheet.

The prototype APTMD can tune to frequencies between 1.208 Hz and 2.877 Hz. This frequency range is appropriate for the test structure. To accommodate a different structure, the frequency range would have to be adjusted. The lower frequency limit is based on the measurement range of the string potentiometer and the length of the rails. In order to tune to lower frequencies both the measurement length and the rail length must be increased. Alternatively the upper frequency limit is based on the height of the pendulum mass.

4.2.2.2 Identification of Modal Frequencies

The desired pendulum arm length (Eq. 4-6) is a function of the optimized tuned frequency ratio (β_{opt}) and the structural natural frequency (f_n). The optimized tuned frequency ratio can be determined offline after identifying the structural stiffness, damping, and mass ratio as discussed in Chapter 3. Hence adjusting the pendulum arm length in real time requires the identification of the structural natural frequency in real time.

$$L_{opt}\left(\beta_{opt}, f_n\right) = \frac{g}{\left(2\pi\beta f_n\right)^2} \quad \textbf{(4- 6)}$$

The first step is to identify the structural natural frequency. This is done by applying a time-varying power spectral density (PSD) estimate of the measured structure response obtained via the modified periodogram method (Matlab, 2007). The PSD estimate calculates the squared magnitude of the FFT computed over windowed segments of the input measurement and normalizes the spectral average by the sum of the squares of the window samples

The periodogram for a sequence of N measurements $(x_1, \ldots, x_N)$ given a sampling frequency F_s is given by Eq. 4-7. For the modified periodogram, the measurement sequence is weighted by a sequence of N windows $(w_1, \ldots, w_N)$ (Eq.4-8). The selected window is a symmetric Hanning window and is given by Eq. 4-9.

The modified periodogram uses an N-point FFT to compute the PSD. The selected FFT length is 2048 points. For a 100 Hz sampling rate, the resultant frequency resolution is 0.049 Hz. The selected number of spectral averages is four. Note that the FFT length is limited by the processing speed of the control board.

Each PSD estimate is calculated using a buffered (first-in-first-out) overlapping window containing successive measurements of the upper floor acceleration (parallel to the direction of excitation). The upper floor acceleration measurement is used since the upper floor exhibits the largest deflections. The selected buffer size is 2048 measurements, or 20.48 seconds given the 100 Hz sampling rate. This is equivalent to the FFT length of the PSD estimation to eliminate any spectral leakage.

$$S(f) = \frac{1}{F_s N}\left|\sum_{n=1}^{N} x_n e^{\frac{-2j\pi fn}{F_s}}\right|^2 \quad \textbf{(4- 7)}$$

$$S(f) = \frac{1}{F_s N}\left|\sum_{n=1}^{N} x_n w_n e^{\frac{-2j\pi fn}{F_s}}\right|^2 \Bigg/ \left(\frac{1}{N}\sum_{n=1}^{N}|w_n|^2\right) \quad \textbf{(4- 8)}$$

$$w(n) = \frac{1}{2}\left(1 - cos\left(2\pi\frac{n}{N}\right)\right), 1 \le n \le N \quad \textbf{(4- 9)}$$

To determine the modal frequencies, the PSD estimate is inserted into a peak identification algorithm. The algorithm first divides the PSD spectrum into ¼ Hz segments and locates the maxima within each section. This set of maxima and their corresponding frequencies is referred to as the segment maxima of the PSD. The algorithm then determines the set of local maxima within the set of segment maxima. A local maximum is defined as a location where neighbouring points have smaller magnitudes. The modal frequencies are a subset of the local maxima. The algorithm differentiates between modal frequencies and local maxima by comparing the set of local maxima to a threshold value. The threshold value is a weighted function of the average magnitude of the PSD over its entire frequency range and the average magnitude over a 1 Hz frequency range centred about the local maxima. If a local maximum exceeds its corresponding threshold value then it is defined as a modal frequency. Figure 47 illustrates how the peak identification algorithm determines modal frequencies from a PSD. The three modal frequencies

identified are local maxima whose magnitudes exceed their respective threshold values. Refer to Appendix F for the peak identification algorithm in its entirety.

The test structure is tuned to a ratio of the natural frequency. In most cases, the lowest modal frequency dominates the response. Therefore, the lowest modal frequency is used in this study. However since, the algorithm identifies multiple structural modes the prototype can easily be customized to tune to an alternative modal frequency.

It is expected that the PSD estimate and peak identification algorithm will yield small variations in the identified natural frequency between multiple time steps. To mitigate any variance, the identified natural frequency is inserted into a buffer containing the identified natural frequency for 500 sample periods (or 5 seconds) which is then inserted into the histogram identification algorithm. The histogram identification algorithm creates a histogram of the identified natural frequency buffer. The histogram contains the frequency of occurrence of any identified natural frequency which falls within the boundary of the bins. For a histogram of N bins, and a maximum and minimum input parameter value of M and m, the resultant bin width (Δ) and center location (c_{n+1}) is presented in Eq. 4-10. The output of the histogram identification algorithm is the natural frequency with the highest rate of occurrence within the buffer.

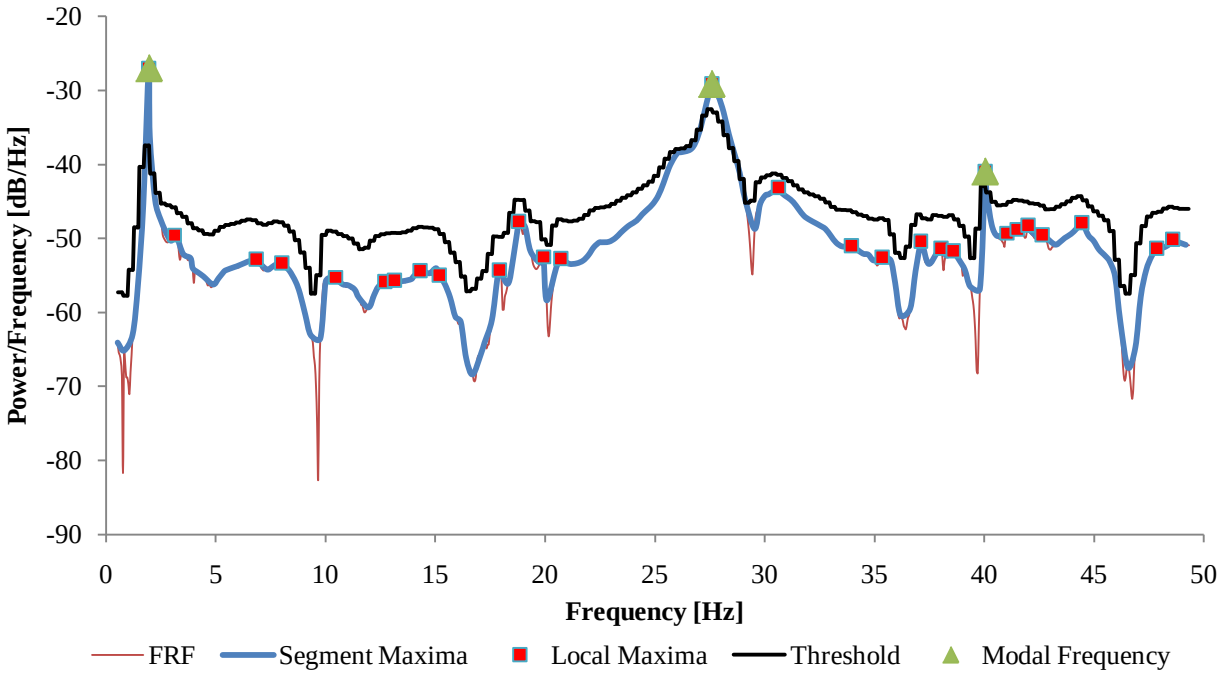

Figure 47: Peak frequency identification

$$\Delta = \frac{M - m}{N} \qquad c_{n+1} = m + \left(n + \frac{1}{2}\right)\Delta \tag{4- 10}$$

Figure 48 shows the identification method for a 25.48 second measurement period. The experiment is conducted by exciting the two-storey test structure with a random Gaussian distributed excitation. A total of 500 measurement windows are collected within the measurement period. For the 1st and 500th window the identified natural frequency is 2.2461 Hz and 2.0996 Hz respectively. The identified natural frequency based on the histogram identification at the end of the measurement window for the experimental test set-up is 2.244 Hz.

4.2.3 Experimental Automation Procedure

The experiment automation procedure is divided into three stages: identification, tuning, and analysis. In the identification, the modal frequencies of the structure are identified. Due to the coupling that exists between the pendulum and the structural mode, the pendulum mass must be restrained while the modal frequencies are identified. Restraining the pendulum mass is achieved by lowering the tuning frame onto the pendulum mass. At the restrained position, the pendulum mass will vibrate when the structure is excited. To further restrict motion, the valves in the adjustable air dampers are fully closed. With the pendulum mass at the restrained position and the adjustable dampers fully closed, the APTMD behaves as a rigid mass attached to the structure.

After identifying the structural natural frequency and the desired pendulum length, the tuning platform position is adjusted. This operation can take several minutes depending on the distance of travel. The rotational speed of the stepper motor actuating the tuning frame is purposely lowered to reduce any machine induced vibrations caused by the stepper motor. During the tuning stage the desired position is kept constant. Once the tuning frame reaches the desired position, it remains there for a discrete period of time. During this period any transient dynamic behaviour induced during the tuning stage is eliminated, after which measurements are taken for analysis. The position of the tuning frame during all three stages is summarized in Figure 49.

The automated program is developed within the Simulink programming environment using Simulink objects. The Simulink solver is configured to solve each iteration within the sampling period (0.01 seconds). Within each iteration, the program reads inputs, performs a modal

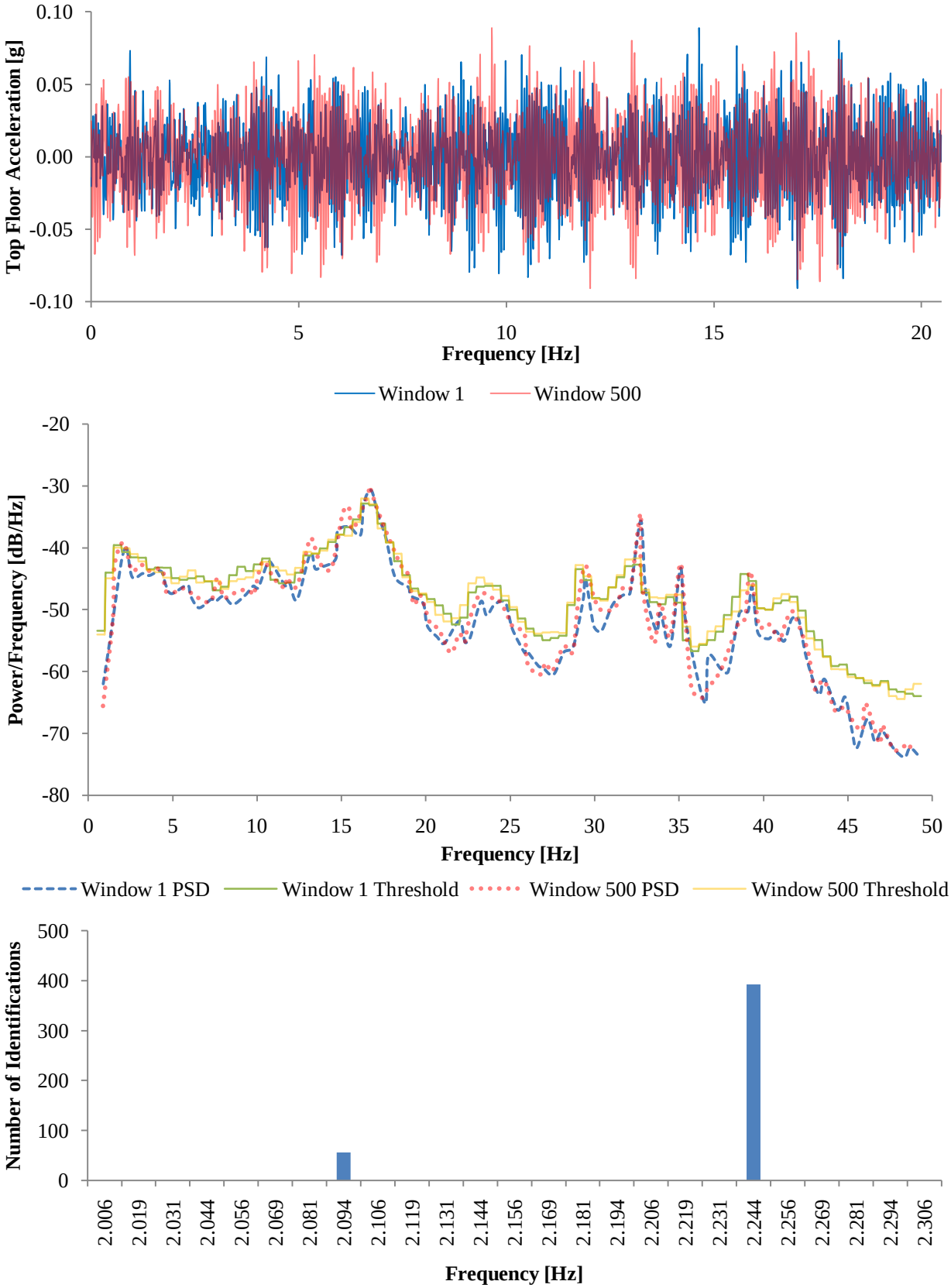

Figure 48: Identification of natural frequency

identification, updates the desired tuning and damping parameters, and updates the outputs. The program is downloaded into the dSPACE controller board for real-time operation. Since the control board must solve each iteration within a sampling period there is an upper limit for program parameters such as buffer size and FFT resolution. Limitations on program parameters are based on the performance limitations of the dSPACE control board.

Real-time interfacing with the APTMD is executed using the Control Desk software. The Control Desk software allows for the creation of custom user interfaces which can measure input and outputs, and any other program variable contained within dSPACE memory. It also allows for manual control of all APTMD tuning parameters.

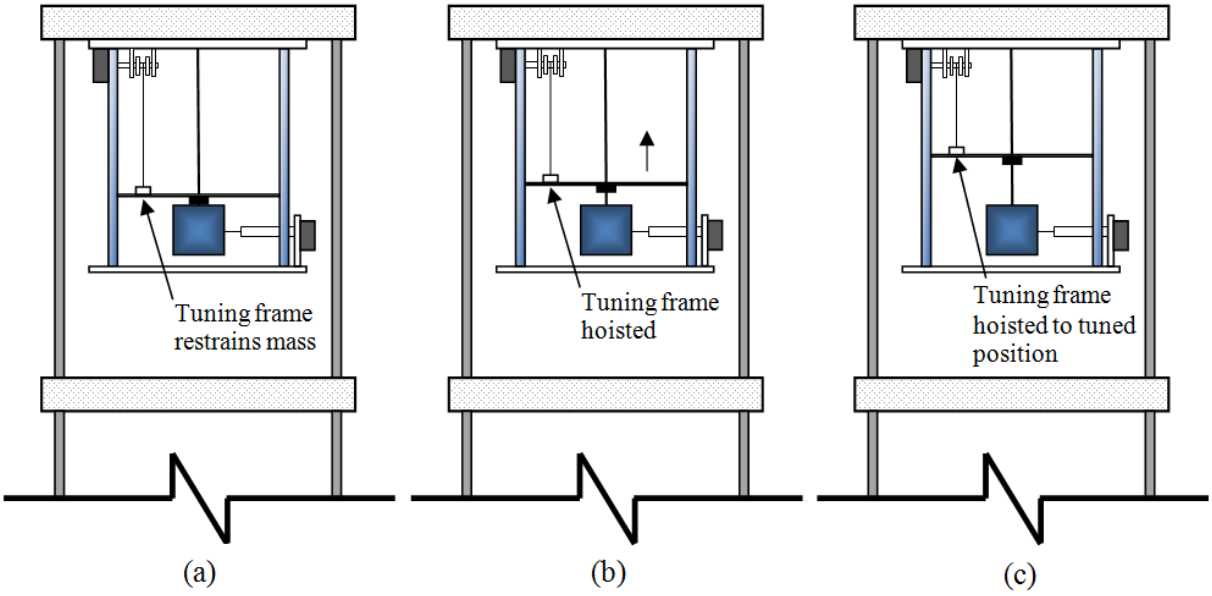

Figure 49: (a) Frame lowered to restrain mass during identification, (b) frame moves towards tuned position during tuning, and (c) frame at tuned position for analysis

Chapter 5: Experimental Results

Experiments were performed on the experimental setup described in Chapter 4 to evaluate the performance of the APTMD. Three different experiments were conducted. The first experiment was performed to identify the test structure's lowest natural frequency by subjecting the test structure to an impact test. The remaining two experiments examine the performance of the APTMD under broadband and narrowband excitations for various tuning and damping parameters.

5.1 Free Vibration Tests and Identification Results

Free vibration tests using impact excitation was performed to identify modal frequencies. In real structures a modal analysis involves analysing multiple structural vibration modes in order to determine if they will be excited by any external forces (Conner 2003). However the prototype APTMD is designed to tune to the lowest modal frequency. Therefore, for the two-storey experimental structure the emphasis will be to identify the lowest modal frequency, referred to as the natural frequency of the structure.

The impact test was performed by striking the lower floor of the structure with an impact hammer. The impact hammer contains a piezoelectric element which measures the force exerted on the structure. The force exerted on the middle floor can be characterized by large peak amplitude sustained over a small period of time. This is an approximation to an impulse forcing function which is defined as having infinitely large peak amplitude sustained over an infinitesimally small period of time. The impulse response produces the structure's free response, since the excitation is not sustained. From the transient response the structure's dynamics can be derived in a relatively straight-forward manner (Johannson 1993).

Figure 50 shows the measured top floor acceleration in the direction of the impact force. The corresponding impact force is shown in Figure 51. The free response of the structure is a decaying sinusoidal function which oscillates at the damped natural frequency of the structure. Given that the damping ratio of the structure is very small, it is reasonable to approximate the natural frequency with the damped natural frequency. Note that the duration of the impact force

is 0.03 seconds with an impulse of 0.83 Ns. This verifies that the impact test provides a good approximation of an impulse response for the structure.

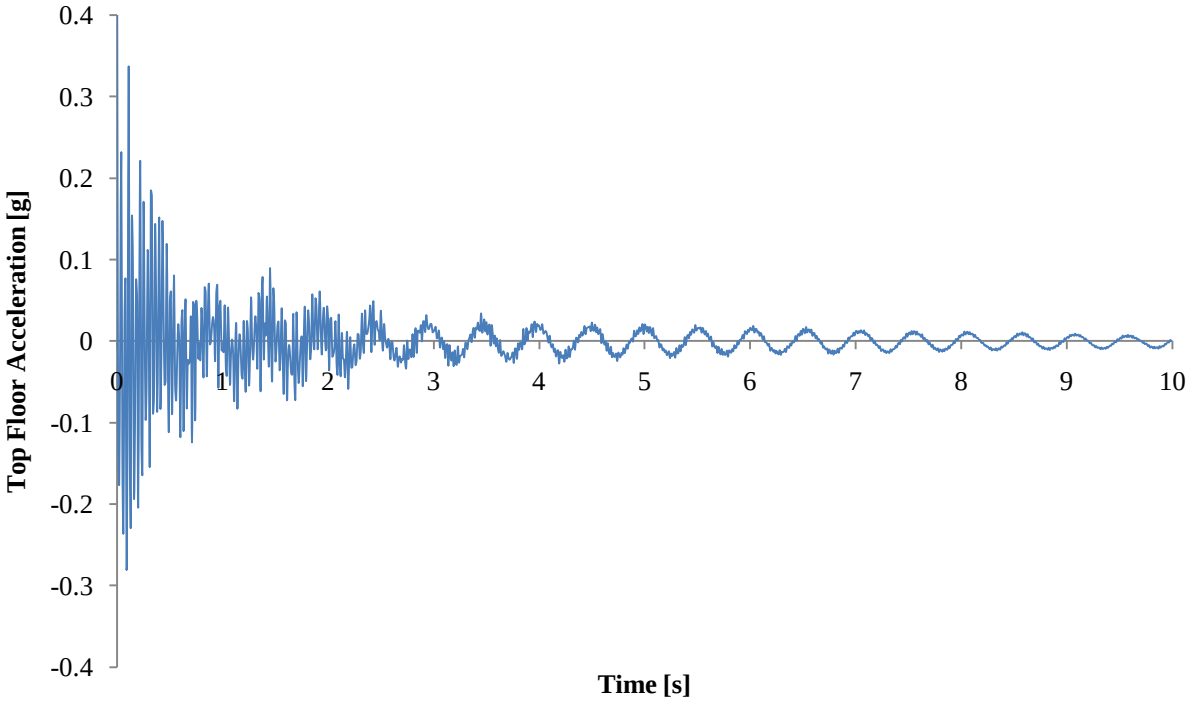

Figure 50: Top floor acceleration from impact

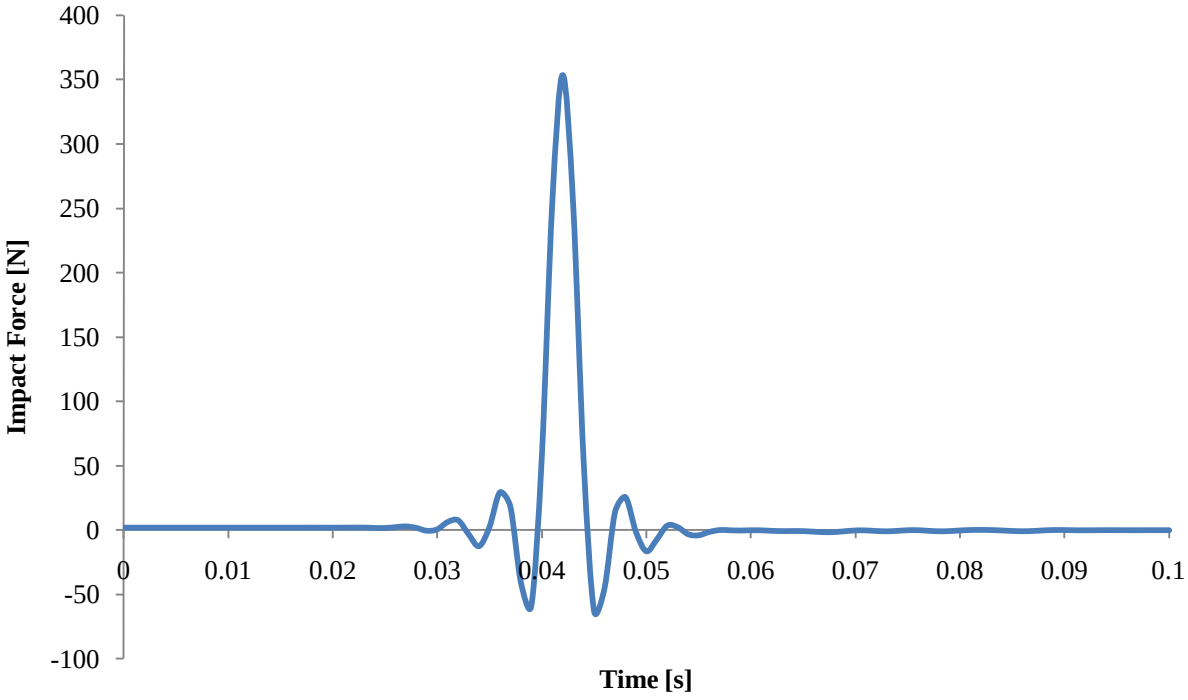

Figure 51: Impact force

Figure 52 shows the FFT magnitude of the measured upper and lower floor accelerations. The lowest modal frequency occurs at 1.855 Hz. This is consistent for all four accelerometer measurements. Hence, the natural frequency of the structure can be identified using either floor of the test structure. It is common practice to measure the top floor of the structure since the top floor exhibits the largest deflections, thereby containing the largest modal energy corresponding to the mode of interest.

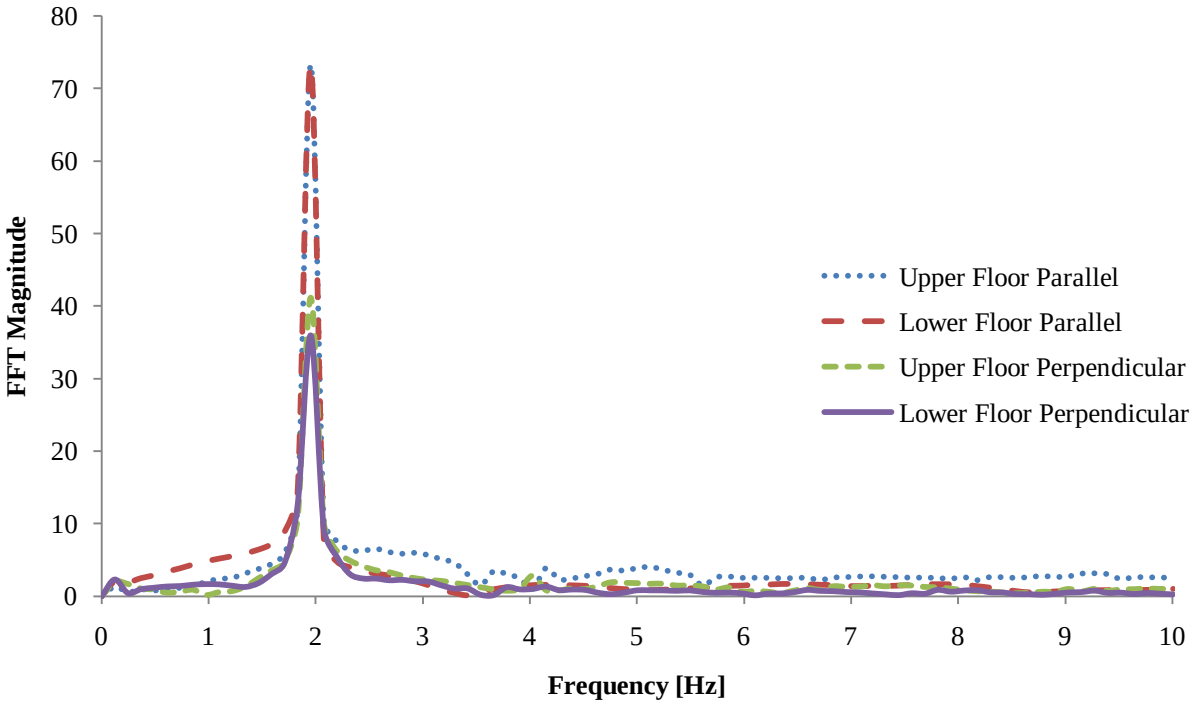

Figure 52: FFT magnitude of impact response (Fs = 1000 Hz and nFFT = 8192)

5. 2 Broadband Forced Excitation Testing and Results

Ideally for broadband testing the structure would be excited by an infinite-bandwidth white noise signal, whose power spectral density is constant over all frequencies. This would ensure that the structure would be excited equally over all frequencies. Unfortunately an infinite-bandwidth white noise signal is purely theoretical. The input excitation is limited not only by the generated signal originating from the dSPACE controller, but by the physical limitations of the shaker itself.

The selected excitation signal was a random excitation with a Gaussian probability distribution. Figure 53 shows the power spectral density estimate of the excitation signal. The power spectral density of the input excitation is reasonably flat over the frequency range. Note that the frequency range is limited by the 100 Hz sampling rate.

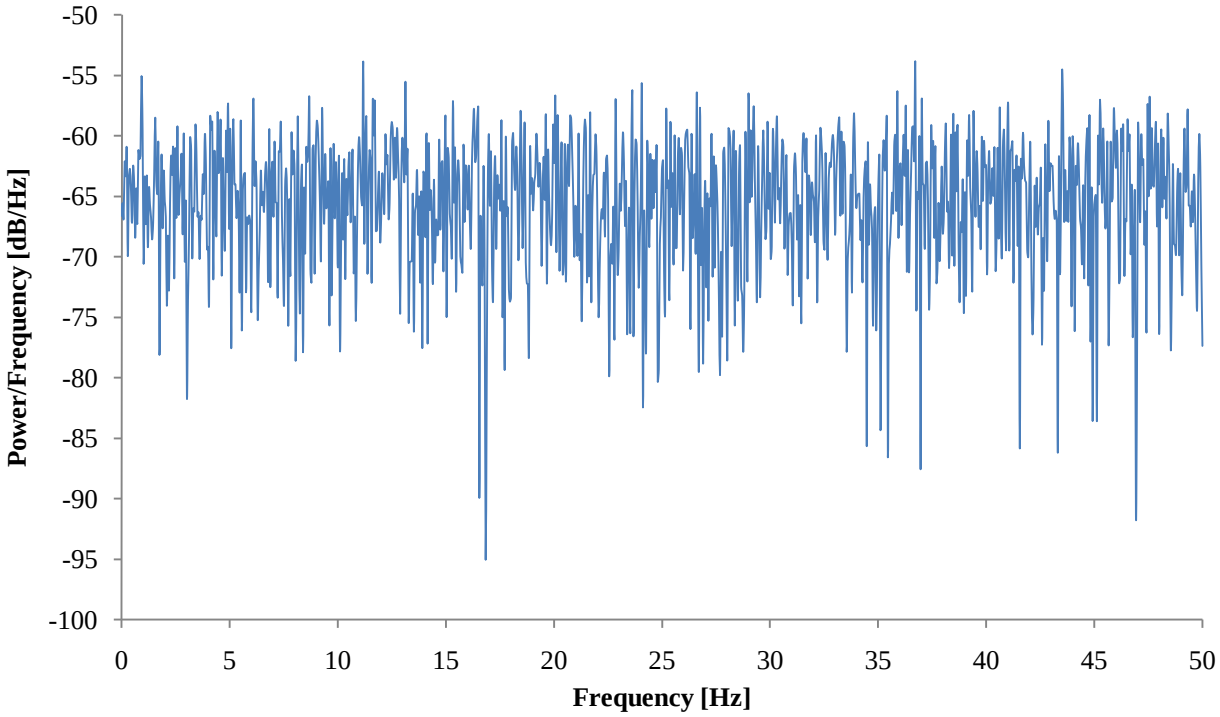

Figure 53: Power spectral density estimate via periodogram window for input excitation signal

The desire is to equally excite a wide range of frequencies while sufficiently exciting the structure. Figure 54 shows the power spectral density for the shaker output for the no load case and when the shaker is driving the structure. The shaker output is measured using a piezoelectric accelerometer mounted to the shaker. Without a load, the power spectral density peaks at 10.205 Hz. With a load attached, the structure-shaker dynamic interactions are obvious. The power spectral density shows peaks located at 2.246 Hz and 27.25 Hz. These frequencies are close to the modal frequencies identified in the impact tests (1.855 Hz and 27.588 Hz). There is no force drop-off at or near the structures natural frequency, as the shaker used is a long-stroke shaker that is capable of driving the structure at the fundamental frequencies. For either the no load case or the structure loading case, the input excitation to the structure is not constant across the spectrum of frequencies. Therefore, identifying the lowest modal frequency based on the input excitation force is required.

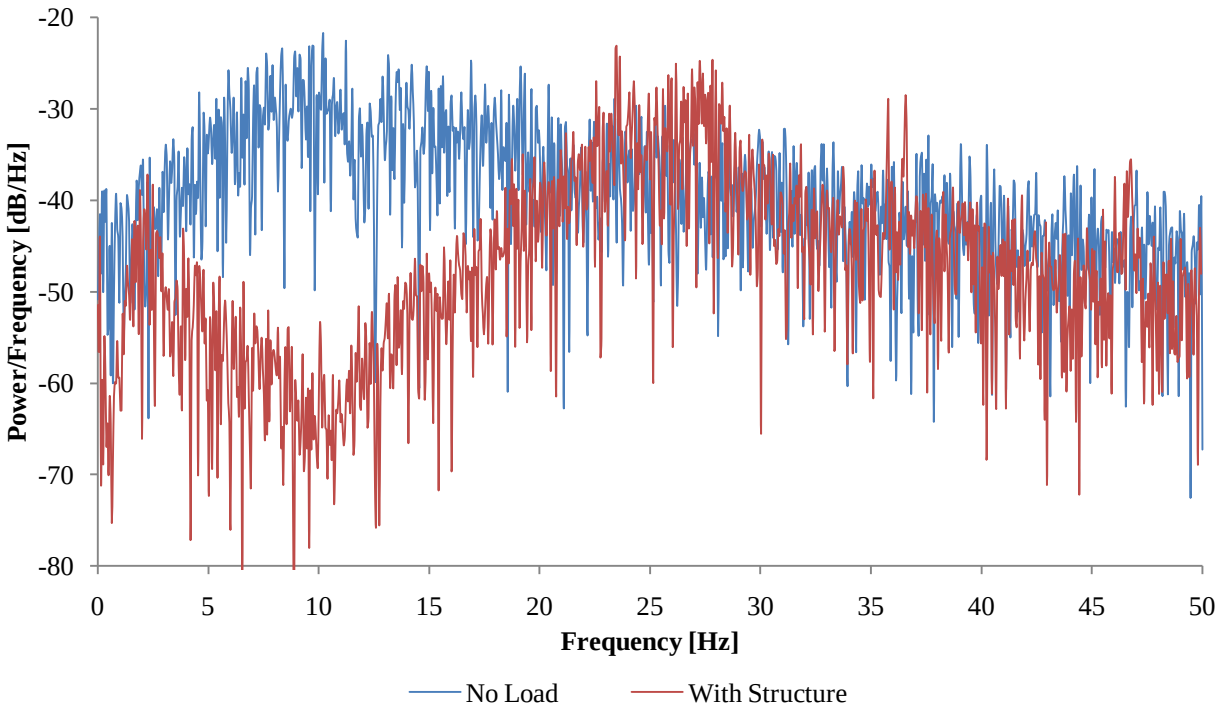

Figure 54: Power spectral density estimate via periodogram window for shaker output

To account for the varying input excitation force along different frequency bands, the identification method is amended. Rather than identifying the modal frequencies based on the periodogram power spectral density estimation, the modal frequencies is identified on the basis of a transfer function between the measured top floor acceleration and the measured input force. The transfer function (Eq. 5-1) is the cross power spectral density of the measured top floor acceleration and the measured input force (P_{yx}) with the power spectral density of the measured input force (P_{xx}). Note that the peak picking algorithm is still used to differentiate modal frequencies.

$$T_{xy}(f) = \frac{P_{yx}(f)}{P_{xx}(f)} \quad \textbf{(5- 1)}$$

Evaluation of the APTMD under broadband excitation is conducted using a similar approach to the optimization method used in Chapter 3. The detuned case is compared to the tuned case under varying external damping levels and tuned frequency ratios. For each testing condition the transfer function estimation between the top floor acceleration measurement and the excitation force measurement are analysed. The performance criterion used to evaluate the optimal

damping and tuning experiment conditions is the maximum peak amplitude of the transfer function estimation over the measured spectrum.

The first test considers the performance when the APTMD is detuned. The detuned test is executed by fixing the tuning platform to the top of the pendulum mass, thus restraining the pendulum mass from moving independently from the structure. The detuned test results are shown in Figure 55. The results indicate two peak frequencies at 1.855 Hz and at 1.953 Hz. Since the lowest peak occurs at 1.855 Hz the APTMD is tuned to this frequency. The resultant adaptive compensation based on the identified natural frequency for a desired tuned frequency ratio of 1 (β = 1) is presented in Figure 56. Measurements were acquired at varying damping levels once the adaptive compensation was complete. A comparison between the tuned (β = 1) and detuned test conditions for varying damping levels is shown in Figure 57. The results reveal that the structural damping at the tuned frequency increases as the external damping coefficient decreases. The response at 1.855 Hz is minimized when the adjustable damper is removed from the pendulum mass. However, the maximum amplitude also occurs when the adjustable damper is removed. This is similar to the results obtained in the simulated system. The optimized damping level for β = 1 is Level 5. Comparing the optimized and detuned test conditions there is a 45.9% decrease in the peak amplitude for the optimized test condition. Furthermore each tuned test condition, with exception to the zero external damping condition, shows an improvement over the detuned case.

The results obtained for tuned frequency ratios ranging from β = 0.95 to β = 0.8 are presented in Figure 58 to Figure 61. A summary of the transfer function estimate peak value for each test condition is summarized in Table 8. The optimal test conditions occur when the APTMD is tuned to 95% of the identified structural natural frequency. This is consistent with the results obtained in the optimization study. The optimized damping condition occurs when the damper valve position is set to Level 5. The optimal valve position identified in the analytical optimization study in Chapter 3 should be Level 7. The performance difference at either valve position is relatively minor and the difference can be attributed to modelling error, and the uncertainty in the behaviour of the adjustable air damper.

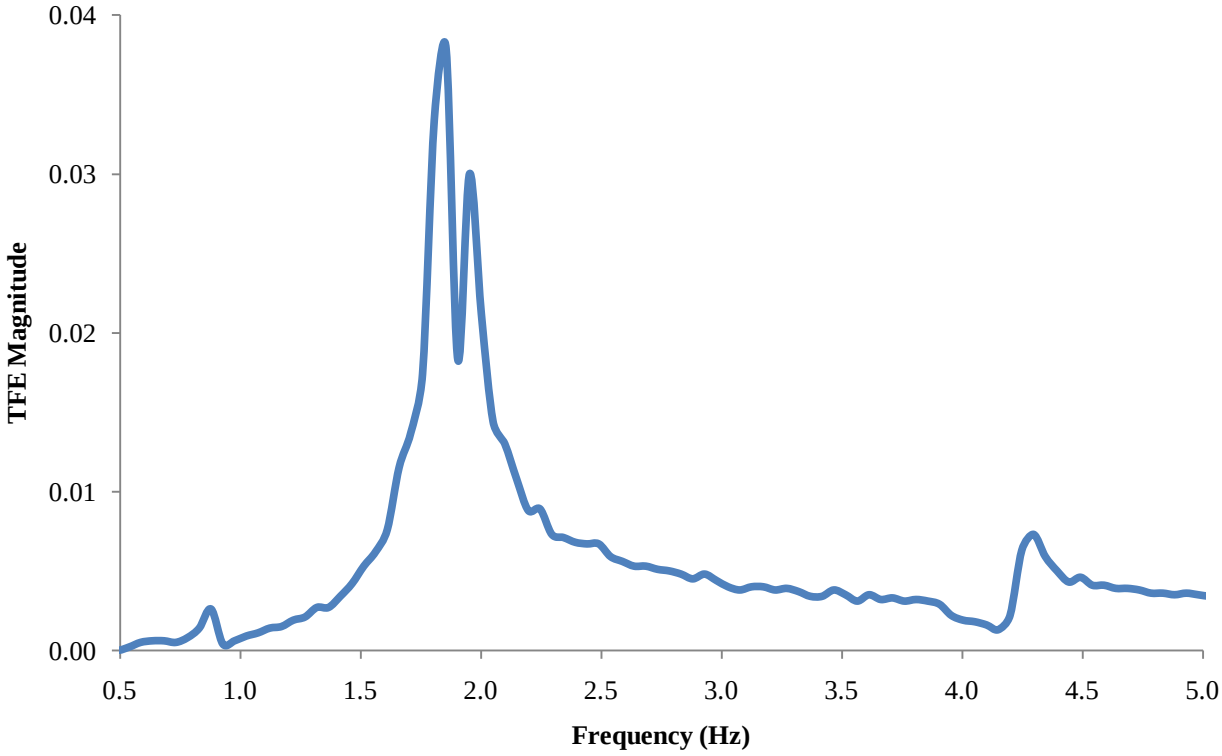

Figure 55: Broadband testing detuned results

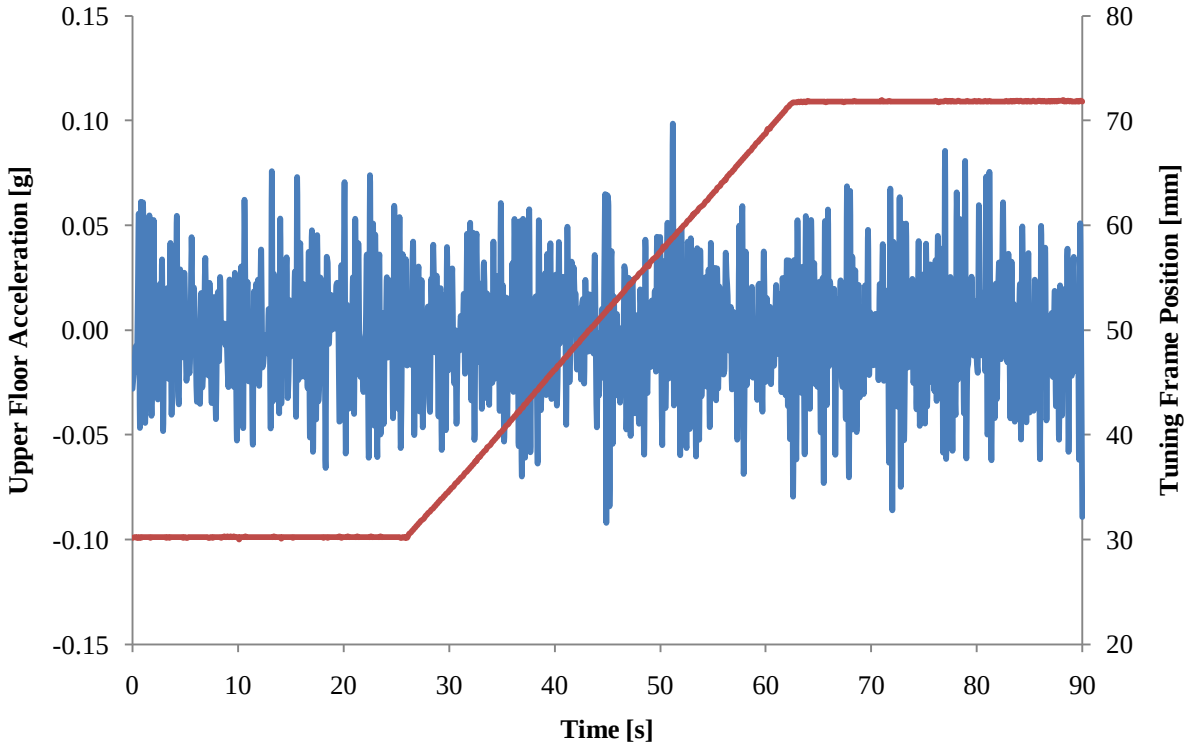

Figure 56: Adaptive compensation for the broadband case

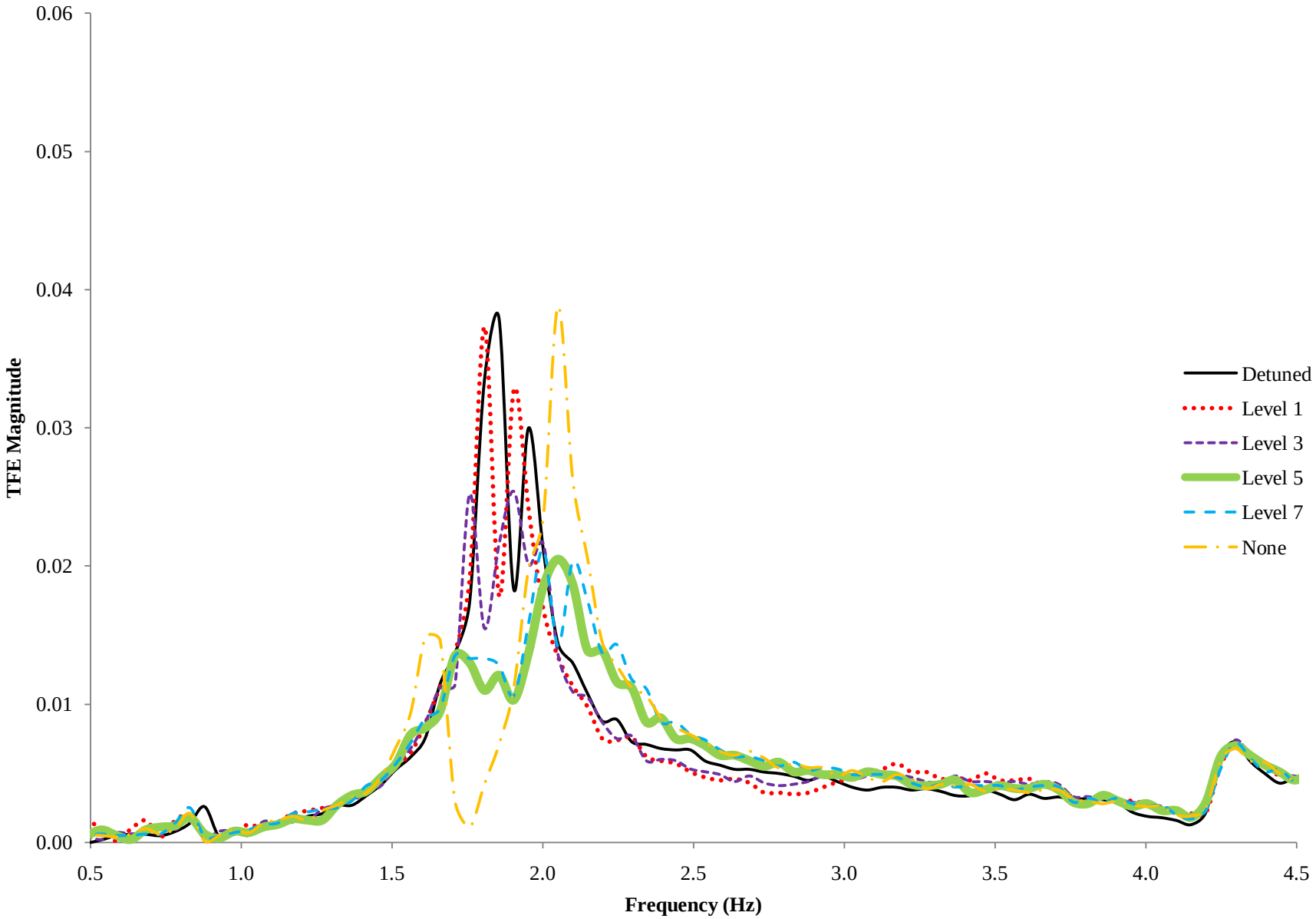

Figure 57: Broadband testing results for β = 1

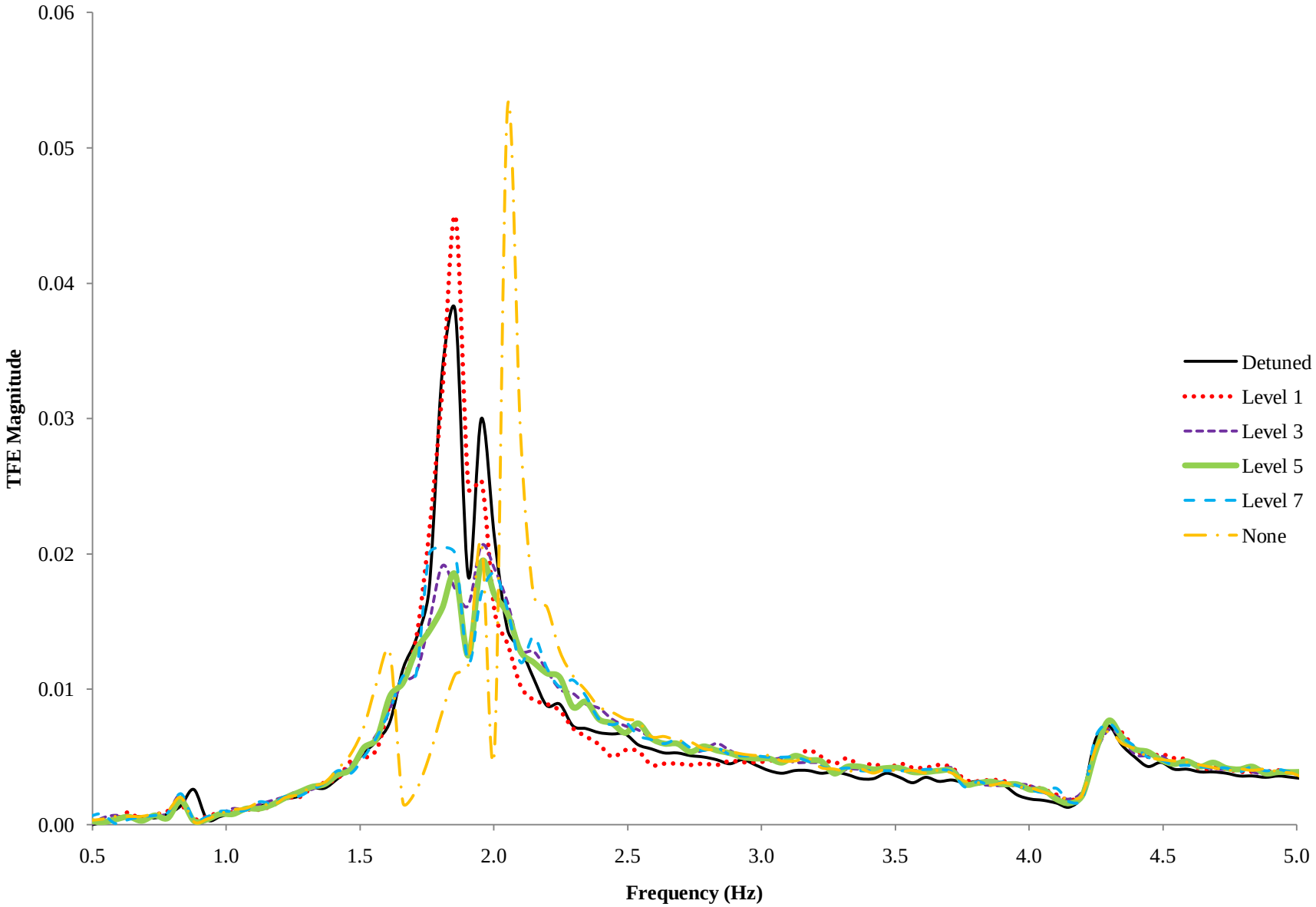

Figure 58: Broadband testing results for β = 0.95

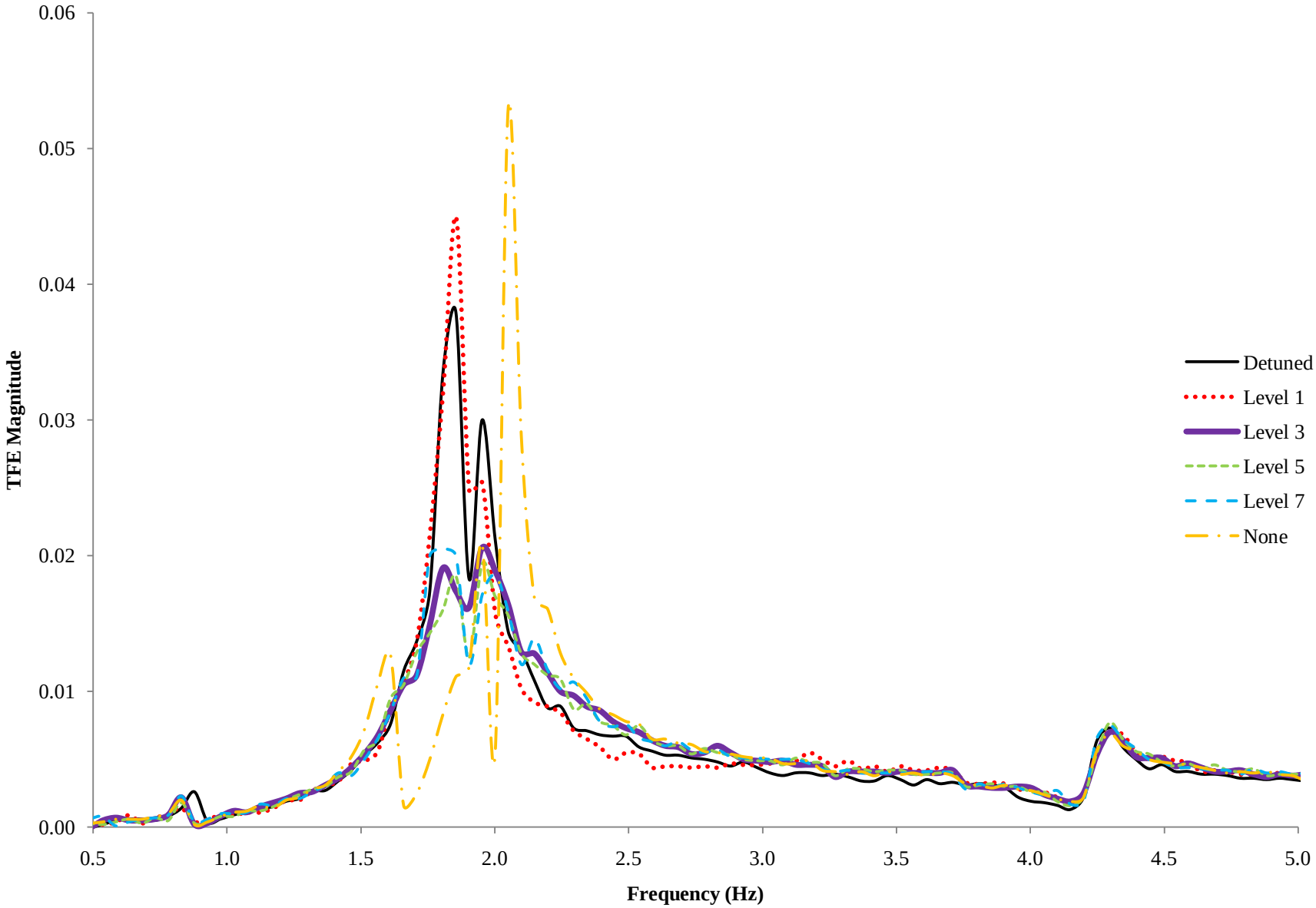

Figure 59: Broadband testing results for β = 0.90

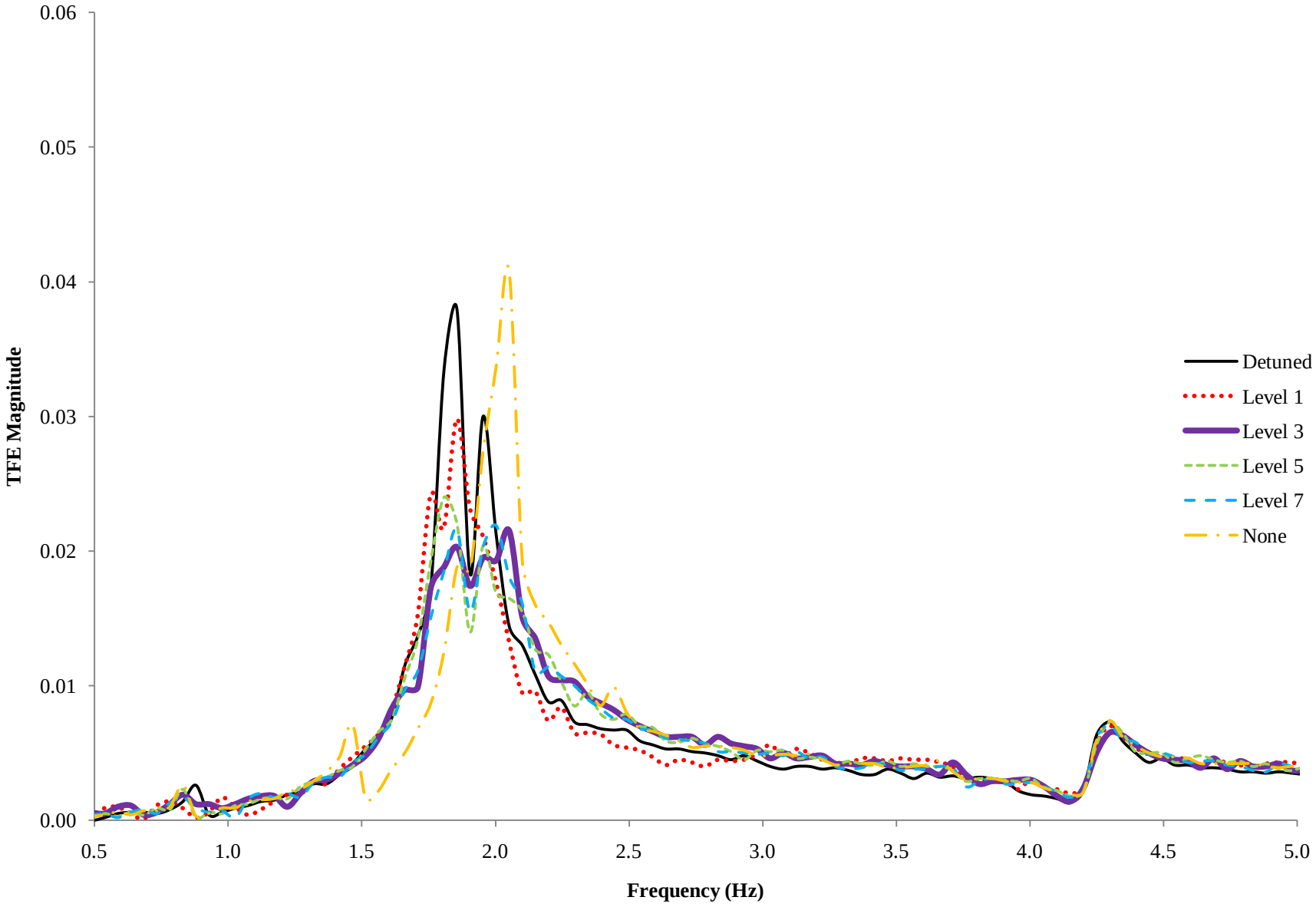

Figure 60: Broadband testing results for β = 0.85

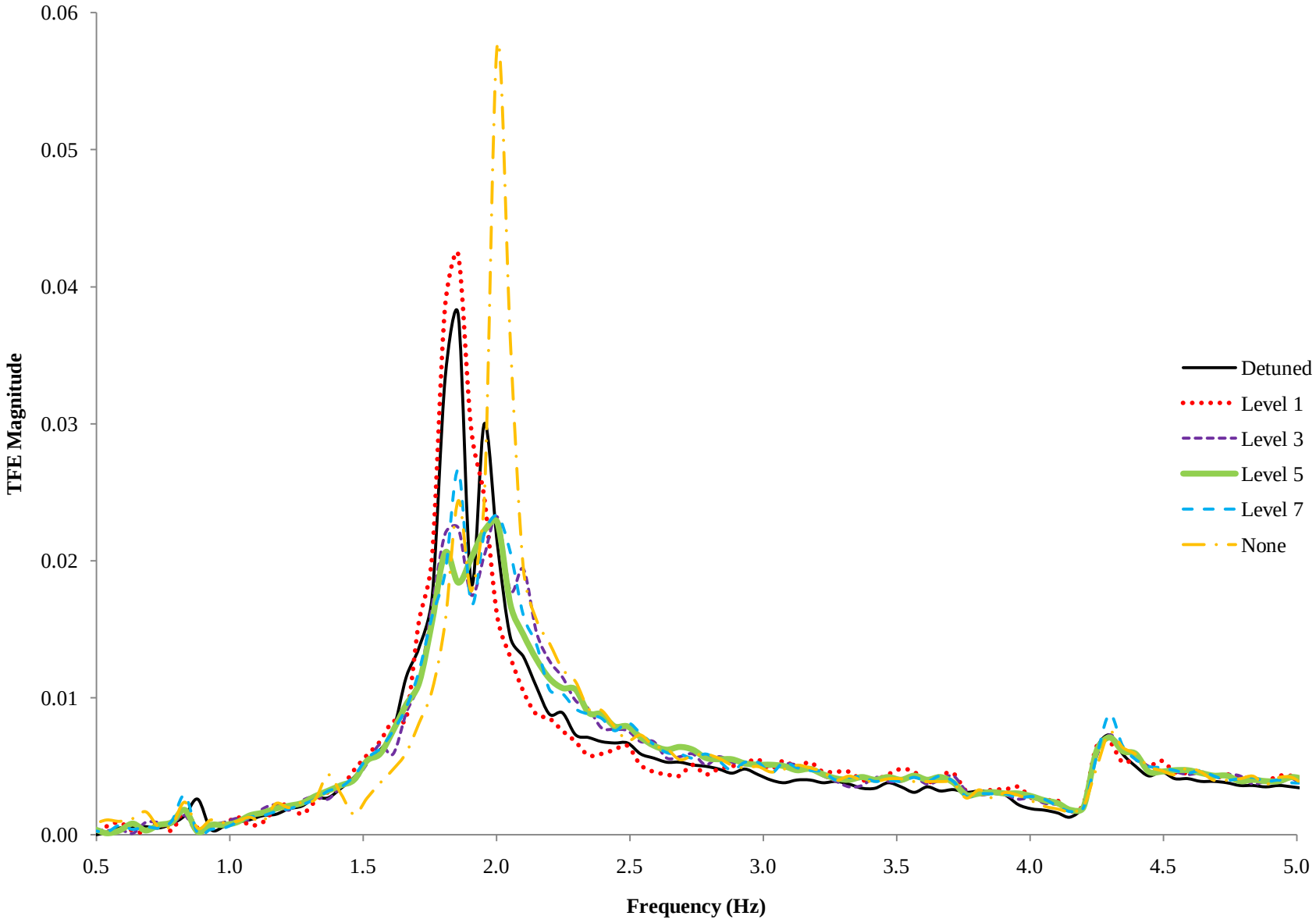

Figure 61: Broadband testing results for β = 0.80

		Tuned Damping Level								
β	**Detuned**	**0**	**1**	**2**	**3**	**4**	**5**	**6**	**7**	**None**
1.000	0.0379	0.0371	0.0373	0.0388	0.0254	0.0206	0.0205	0.0334	0.0212	0.0388
0.975	0.0379	0.0415	0.0418	0.0294	0.0233	0.0247	0.0228	0.0204	0.0239	0.0447
0.950	0.0379	0.0468	0.0449	0.0279	0.0206	0.0294	0.0194	0.0212	0.0205	0.0530
0.925	0.0379	0.0436	0.0409	0.0261	0.0246	0.0326	0.0254	0.0205	0.0212	0.0409
0.900	0.0379	0.0274	0.0321	0.0235	0.0196	0.0363	0.0285	0.0223	0.0221	0.0456
0.875	0.0379	0.0380	0.0349	0.0290	0.0238	0.0276	0.0239	0.0230	0.0247	0.0336
0.850	0.0379	0.0331	0.0298	0.0239	0.0215	0.0318	0.0240	0.0216	0.0219	0.0407
0.825	0.0379	0.0368	0.0375	0.0211	0.0262	0.0323	0.0251	0.0227	0.0204	0.0523
0.800	0.0379	0.0292	0.0424	0.0260	0.0232	0.0248	0.0228	0.0284	0.0266	0.0577

Table 8: Transfer function estimate peak values

5.3 Narrowband Forced Excitation Testing and Results

For narrowband testing, the structure was excited by a harmonic excitation force. Two sets of experiments were performed. First, the APTMD performance with changing excitation frequency was examined. The excitation frequency was varied from 80% to 100% of the identified natural frequency of the structure (1.855 Hz) in increments of 5%. At each frequency, the upper-floor acceleration for the detuned condition was measured. The APTMD was then manually tuned to the natural frequency of the structure. Once at the tuned position the upper floor response was measured. The APTMD performance at various damping valve position are examined.

The results of the first narrow-band experiment are presented in Table 9. The root mean square of the measured upper floor acceleration is used to evaluate the results. Note that the second column for each damping condition represents the performance improvement over the respective detuned test condition. The results show that the upper floor RMS acceleration increases as the excitation frequency approaches the resonant excitation frequency. More importantly, the performance improvement over the detuned case increases significantly as the structure is excited around the tuned natural frequency. Reducing the external damping coefficient by adjusting the damper to the Level 6 valve position produces the largest performance improvements under all excitation frequencies. Figure 62 to Figure 64 illustrates the upper floor

response for varying excitation frequencies at the Level 6 valve position. The results demonstrate an appreciable performance improvement within 10% of the resonant testing condition.

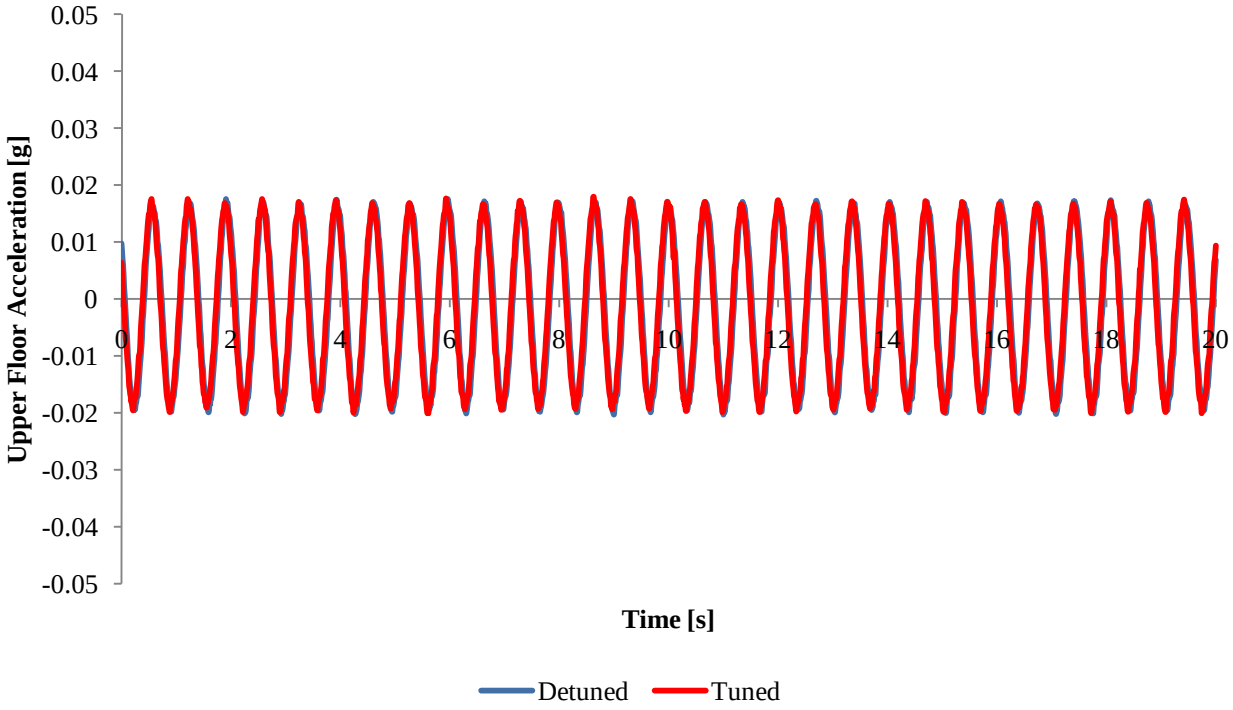

Figure 62: Detuned vs. tuned upper floor acceleration for β = 0.80

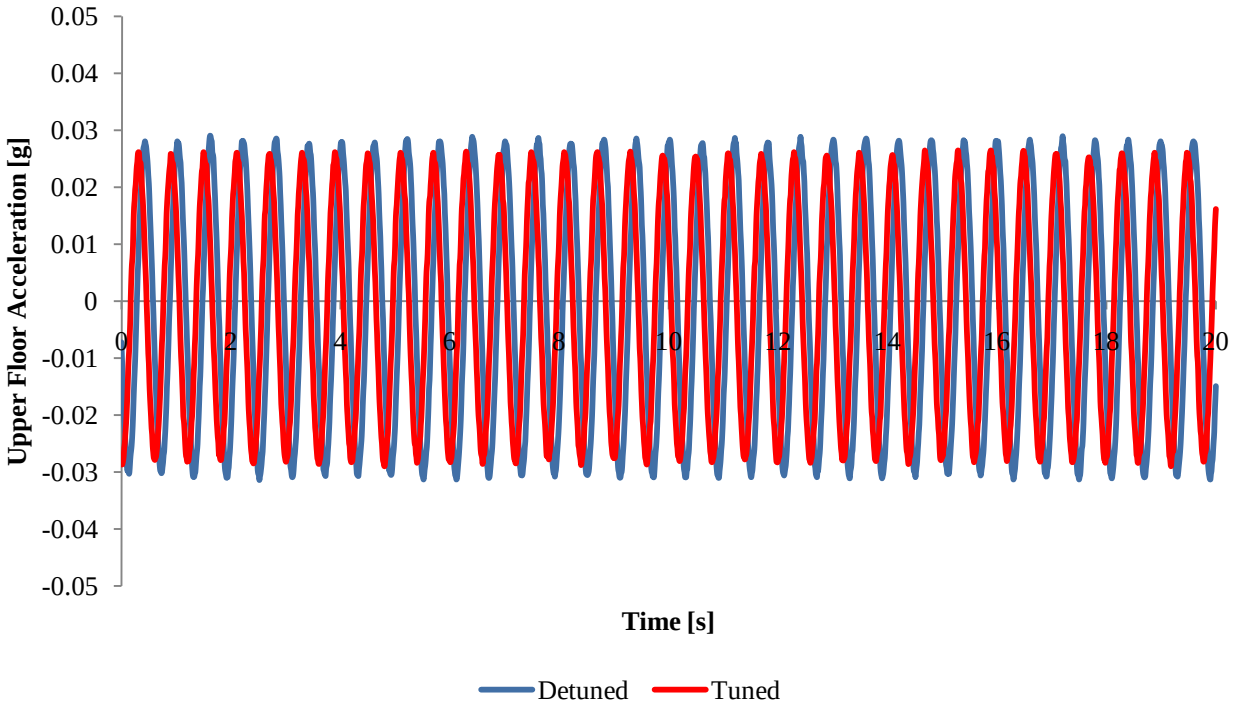

Figure 63: Detuned vs. tuned upper floor acceleration for β = 0.90

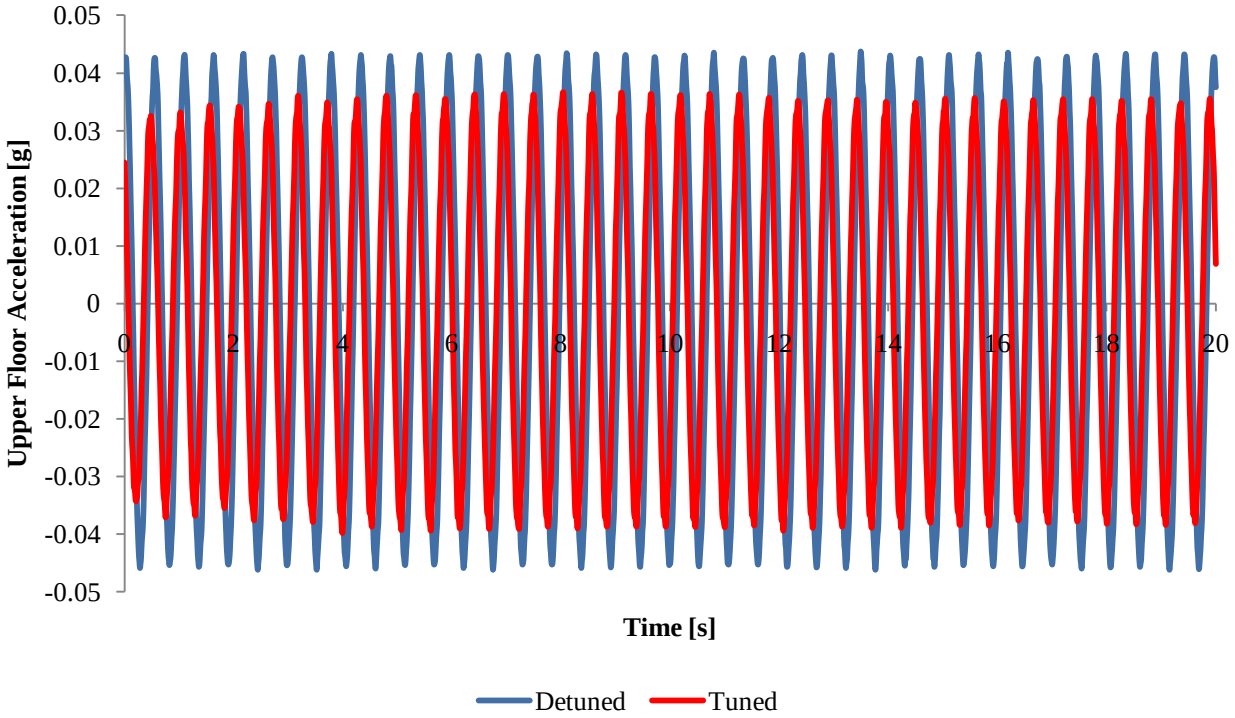

Figure 64: Detuned vs. tuned upper floor acceleration for β = 1.00

	Upper Floor RMS Acceleration [g]												
β	**Detuned**	**Level 3**		**Level 4**		**Level 5**		**Level 6**		**Level 7**		**No Damp**	
0.80	0.0128	0.0127	0.8%	0.0126	1.6%	0.0127	0.8%	0.0126	1.6%	0.0126	1.6%	0.0126	1.6%
0.85	0.0165	0.0161	2.4%	0.0159	3.6%	0.0161	2.4%	0.0159	3.6%	0.0160	3.0%	0.0160	3.0%
0.90	0.0206	0.0196	4.9%	0.0194	5.8%	0.0198	3.9%	0.0190	7.8%	0.0195	5.3%	0.0195	5.3%
0.95	0.0252	0.0234	7.1%	0.0230	8.7%	0.0236	6.3%	0.0221	12.3%	0.0231	8.3%	0.0231	8.3%
1.00	0.0304	0.0279	8.2%	0.0272	10.5%	0.0280	7.9%	0.0257	15.5%	0.0272	10.5%	0.0272	10.5%

Table 9: Upper floor RMS acceleration for varying valve damper positions under changing excitation frequency

The results indicate that APTMD performance is reduced when the structure is excited sufficiently far from the natural frequency. However, the structural response away from the natural frequency will also be reduced. Alternatively, tuning to the natural frequency effectively detunes the APTMD when the excitation frequency moves away from the natural frequency. The results indicate that the smaller the separation between the two frequencies, the greater the APTMD performance.

In the second set of tests, a sequence of successive tuning and detuning scenarios were performed. The structure was excited at the structural natural frequency and the APTMD was

allowed to identify and tune to the excitation frequency. Following this, the APTMD was manually tuned to 80% of the natural frequency. The damper valve position was set to Level 7. The results are presented in Figure 65. The reduction in the response when the APTMD is tuned to the natural frequency over the two detuned conditions is apparent. A similar test was conducted where the APTMD is manually detuned to 90% of the natural frequency. The results are presented in Figure 66. The RMS upper floor acceleration for each test condition is presented in Table 10. The results show a 27.4% and 28.9% improvement between the tuned (β = 1) and detuned test conditions for Test 1 and Test 2, respectively. Comparing the tuned (β = 1) and slightly detuned (β = 0.8 and 0.9) test conditions there is a 17.2% and 7.8% improvement for Test 1 and Test 2, respectively. The results illustrate significant performance improvements for small changes in the tuned conditions.

Test	Upper Floor RMS Acceleration [g]			
	Detuned	**Tuned β = 1.0**	**Tuned β = 0.8**	**Tuned β = 0.9**
1	0.0310	0.0225	0.0273	
2	0.0310	0.0220		0.0244

Table 10: Upper floor RMS acceleration comparison between tuned and detuned test conditions

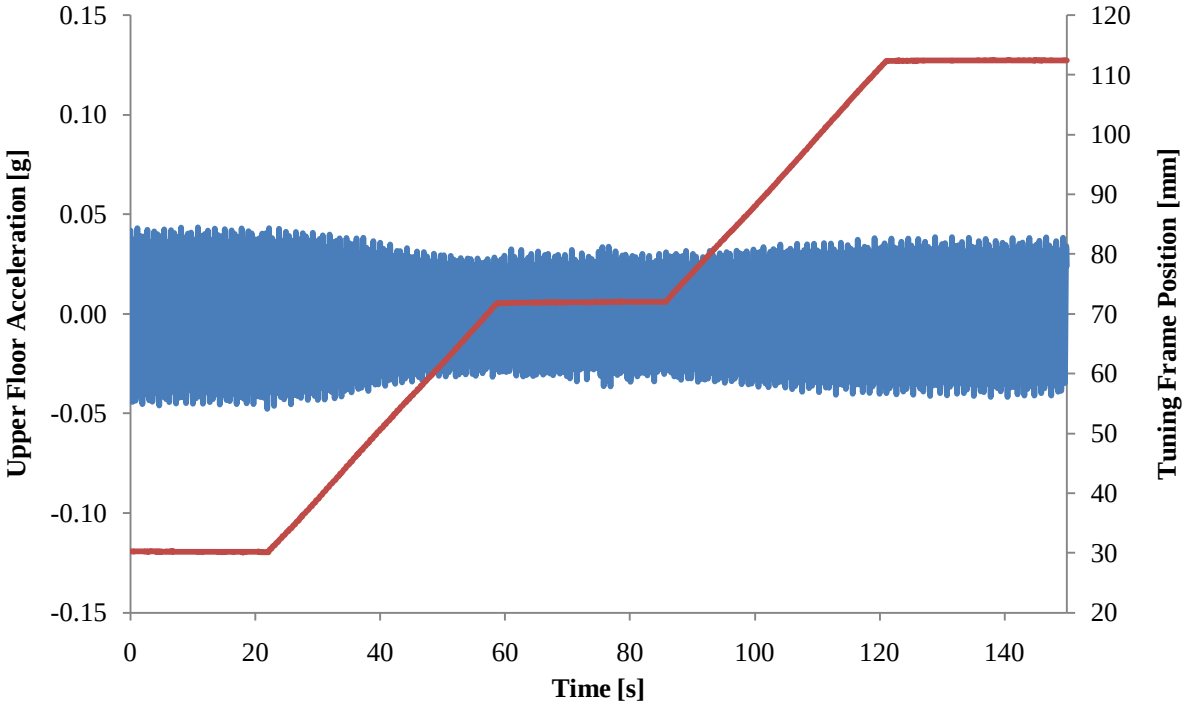

Figure 65: Adaptive compensation for narrowband excitation test 1

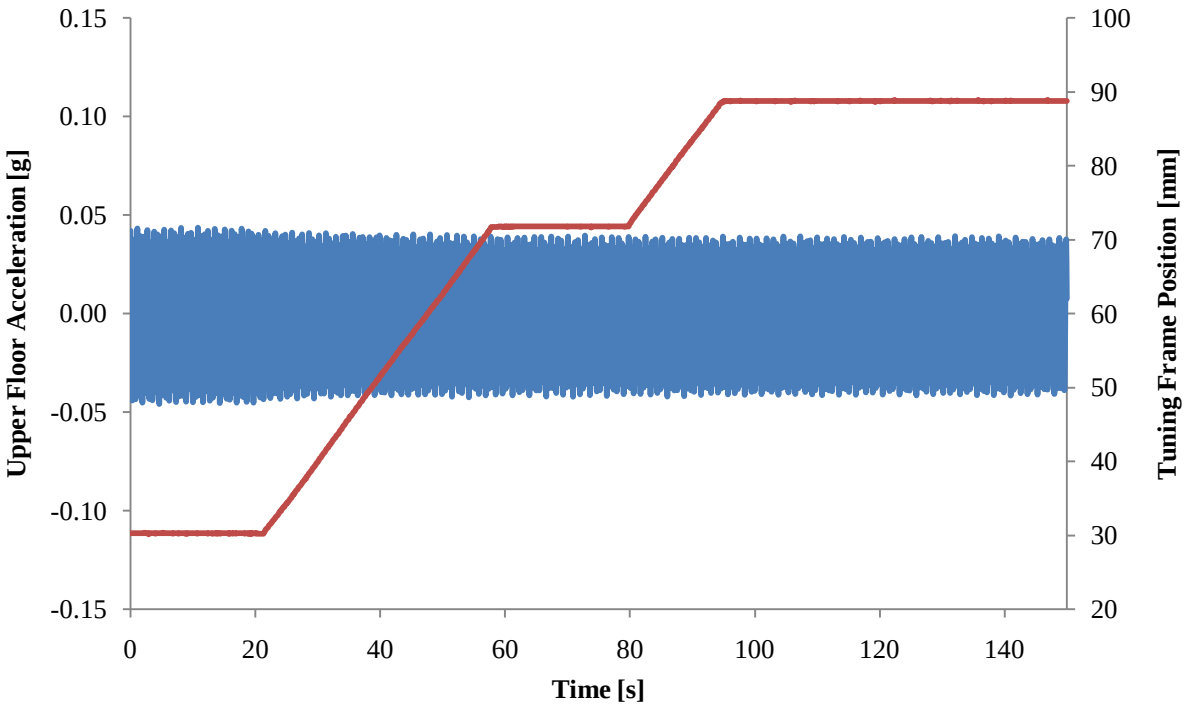

Figure 66: Adaptive compensation for narrowband excitation test 2

Chapter 6: Conclusions and Future Work

The APTMD presented here is a novel TMD system developed to provide the capability to autonomously tune to the structural frequency while providing control of the external damping to the PTMD mass. These capabilities allow the APTMD to adapt to changes in structural characteristics that occur in real structures due to structural modification or deterioration. The prototype tested can readily be scaled to retrofit existing PTMDs or for new design.

To evaluate the performance of the APTMD, the prototype was attached to a test structure and subjected to narrowband and broadband excitations. The objective of these tests was to demonstrate the performance improvements over various detuned conditions when the structure is tuned to the structural natural frequency. The narrowband tests revealed a 7.8% to 17.2% improvement in the measured top floor response when comparing the tuned and off-tuned test conditions. For broadband testing, an optimization analysis was conducted. These tests demonstrated significant improvements achieved by adjusting both the tuning frequency and damping coefficient provided by the external damper. Furthermore they validated the results obtained in the simulated optimization study.

While the experiment results are certainly positive, they are meant to demonstrate the importance of optimizing the TMD tuning parameters to reduce structural vibrations. In comparison to passive TMD systems the APTMD will perform as well or better, depending on the disparity between the optimal TMD tuning parameters and the calibrated TMD parameters. Ultimately the APTMD is designed to be an advanced tool in mitigating structural vibrations by autonomously tuning itself based on the optimal tuning parameters.

The next step is to develop a full scale prototype of the existing prototype APTMD. The scale would be dependent on the size of the test structure. An appropriate testing scale would utilize a 1-metric tonne pendulum mass. Given the difference in volume and mass between the 1.470 kg pendulum mass presented in this thesis and the proposed 1-metric tonne pendulum mass, the full scale prototype APTMD would have to be redesigned. The redesign would be able to support the spatial volume and loads of the significantly larger pendulum mass. For example, linear bearings and a hardened precision shaft can be used to support the larger pendulum loads exerted on the

tuning frame. Larger adjustable dampers would be implemented to provide a longer stroke and greater damping force.

The main design elements of the small-scale prototype APTMD would be used in the full-scale prototype APTMD. The full scale design would utilize a tuning frame hoisted by a cable winch. Since the cable winch hoists the tuning frame and not the pendulum mass, the motor requirements would be modest. A similar motorized control system can be used to control the adjustable valves on a larger damper. If the desired tuning range exceeds the current prototype setup, longer rails and a displacement sensor with a larger measurement range can be used. The modal identification system would remain identical, with exception of an alternative accelerometer to measure lower frequency structural vibrations. In all, the modifications required to scale the size of the prototype APTMD focus primarily on supporting the inertial loads of the pendulum mass.

Full size prototype APTMD testing would provide a more clear idea of the obstacles that may emerge if the existing design is to be utilized in a real structure. The ultimate goal in developing the APTMD is for the technology to become a superior alternative to existing passive TMD technologies.

References

Baker, W.F., Korista, S., and Novak, L.C., 2007. Burj Dubai: Engineering the World's Tallest Building, *The Structural Design of Tall and Special Buildings*, 16(4), pp.361-375

Brownjohn, J.M.W., Carden, E.P., Goddard, C.R., and Oudin, G., 2010. Real-Time Performance Monitoring of Tuned Mass Damper System for a 183 m Reinforced Concrete Chimney, *Journal of Wind Engineering and Industrial Aerodynamics*, 98(3), pp.169-179

Carpineto, N., Lacarbonara, W., and Vestroni, F., 2010. Mitigation of Pedestrian-Induced Vibrations in Suspension Footbridges via Multiple Tuned Mass Dampers, *Journal of Vibration and Controls*, 16(5), pp.749-776

Chang, M.L., Lin, C.C., Ueng, J.M., and Hsieh, K.H., 2010. Experimental Study on Adjustable Tuned Mass Damper to Reduce Floor Vibration Due to Machinery, *Structural Control and Health Monitoring*, 17(5), pp.532-548

Chen, G., and Wu, J., 2001. Optimal Placement of Multiple Tuned Mass Dampers for Seismic Structures, *Journal of Structural Engineering*, 127(9), pp.1054-1062

Chey, M.H., Carr, A.J., Chase, J.G., and Mander, J.B., 2007. Design of Semi-Active Tuned Mass Damper Building Systems using Resettable Devices, *8th Pacific Conference on Earthquake Engineering*, Singapore, Dec 5-7

Chey, M.H., Chase, J.G., and Mander, J.B., Carr, A.J., 2010. Semi-Active Tuned Mass Damper Building Systems: Design, *Earthquake Engineering and Structural Dynamics*, 39(2), pp.119-139

Clark, A.J., 1988. Multiple Passive Tuned Mass Dampers for Reducing Earthquake Induced Building Motion, Proceedings of the 9th World Conference of Earthquake Engineering, 5, pp.779-784

Conner, J.J., 2003. *Introduction to Structural Motion Control*. Pearson Education Inc.

Foreman, R., Kearney, V., and Engle, R., 1967. Numerical Analysis of Crack Propagation in Cyclic-Loaded Structures, *Journal of Basic Engineering*, 89, pp. 459-464

Franklin, G.F., Fowell, J.D., and Emami-Naeini, A., 2009. *Feedback Control of Dynamic Systems*, 6th Ed., Prentice Hall

Gerges, R.R., and Vickery, B.J., 2003. Parametric Experimental Study of Wire Rope Spring Tuned Mass Dampers, *Journal of Wind Engineering and Industrial Aerodynamics*, 91(12), pp.1363-1385

Gerges, R.R., and Vickery, B.J., 2005. Optimum Design of Pendulum-Type Tuned Mass Dampers, *The Structural Design of Tall and Special Buildings*, 14(4), pp.353-368

Haskett, T., Breukelman, B., Robinson, J., and Kottelenberg, J., Tuned Mass Dampers Under Excessive Structural Excitation. *Report of the Motioneering Inc*. Guelph, Ontario, Canada N1K 1B8

Igusa, T., and Xu, K., 1994. Vibration Control Using Multiple Tuned Mass Dampers, *Journal of Sound and Vibrations*, 175(4), pp.491-503

Irwin, A.W., 1978. Human Response to Dynamic Motion of Structures, *The Structural Engineer*, 56(9), pp. 237-244

Johannsson, R., 1993. *System Modeling and Identification*, Prentice Hall.

Kareem, A., Kijewski, T., and Tamura, Y., 2007. Mitigation of Motion of Tall Buildings with Specific Examples of Recent Applications, *Wind and Structures*, 2(3), pp.201-251

Lee, C.L., Chen, Y.T., Chung, L.L., and Wang, Y.P., 2006. Optimal Design Theories and Applications of Tuned Mass Dampers, *Engineering Structures*, 28(1), pp.43-53

Li, C., Li, J., and Qu, Y., 2010. An Optimal Design Methodology of Active Tuned Mass Damper for Asymmetric Structures, *Mechanical Systems and Signal Processing*, 24(3), pp.746-765

Lin, C.C., Lin, G.L., and Wang, J.F., 2010. Protection of Seismic Structures Using Semi-Active Friction TMD, *Earthquake Engineering and Structural Dynamics*, 39(6), pp.635-659

Lin, Y.Y., and Cheng, C.M., 2001. Performance of Multiple Tuned Mass Dampers for Suppressing Buffeting Response and Increasing Flutter Speed of Long-S-Pan Bridges, *Journal of the Chinese Institute of Engineers*, 24(3), pp.273-266

Lourenco, R., Roffel, A.J., and Narasimhan, S., 2009. Adaptive Pendulum Mass Damper for Control of Structural Vibration, *CANSMART Workshop*, Montreal, Quebec, Canada

Matlab, 2007a, *The Mathworks*. Natick, MA, 2007.

Mendis, P., Ngo, T., Haritos, N., Hira, A., Samali, B., and Cheung, J., 2007. Wind Loading on Tall Buildings, *Electronic Journal of Structural Engineering*, 7(Special Issue), pp.41-54

Nagarajaiah, S., and Varadarajan, N., 2005. Short Time Fourier Transform Algorithm for Wind Response Control of Buildings with Variable Stiffness TMD, *Engineering Structures*, 27(3), pp.431-441

Nagarajaiah, S., and Sonmez, E., 2007. Structures with Semiactive Variable Stiffness Single/Multiple Tuned Mass Dampers, *Journal of Structural Engineering*, 133(1), pp.67-77

Nagashima, I., 2001. Optimal Displacement Feedback Control Law for Active Tuned Mass Damper, *Earthquake Engineering and Structural Dynamics*, 30(8), pp.1221-1242.

Nishimura, T., Kobori, T., Sakamoto, M., Koshika, N., Sasaki, and K., Ohrui, S., 1992. Active Tuned Mass Damper, *Smart Materials and Structures*, 1(4), pp.306-311

du Plessis, A. 2010. [online]. Available at: http://en.wikipedia.org/wiki/File:Taipei_101_Tuned_Mass_Damper_2010.jpg [accessed on 22 October 2010]

Powell, C. 2007.Taipei 101. [online]. Available at: http://en.wikipedia.org/wiki/File:Taipei101.portrait.altonthompson.jpg [accessed on 22 October 2010]

Roffel, A.J., Lourenco, R., Narasimhan, S., and Yarusevych, S., 2011. Adaptive Compensation for Detuning in Pendulum Tuned Mass Dampers, *Journal of Structural Engineering*, 137(2), pp.242-251

Sain, T., and Chandra Kishen, J.M., 2007. Prediction of Fatigue Strength in Plain and Reinforced Concrete Beams, *ACI Structural Journal*, 104(5), pp.621-628

Setareh, M, and Hanson, R., 1992. Tuned Mass Dampers to Control Floor Vibrations from Humans, *Journal of Structural Engineering*, 118, pp.741-762

Setareh, M., 2002. Floor Vibration Control Using Semi-Active Tuned Mass Dampers, *Canadian Journal of Civil Engineering*, 29(1), pp.76-84

Setareh, M. Ritchey, J.K., Baxter, A.J., and Murray, T.M., 2006. Pendulum Tuned Mass Dampers for Floor Vibration Control, *Journal of Performance of Construction Facilities*, 20(1), pp.64-73

Setareh, M. Ritchey, J.K., Murray, T.M., Koo J.H., and Ahmadian, M., 2007. Semi-Active Tune Mass Damper for Floor Vibration Control, *Journal of Structural Engineering*, 133(2), pp.242-250

Spencer, B.F., and Sain, M.K., 1997. Controlling Buildings: A New Frontier in Feedback, *Control Systems Magazine*, 17(6), pp.19-35

Sun, L.M., Fujino, Y., Pacheco, B.M., and Chaiseri, P., 1992. Modelling of Tuned Liquid Damper, *Journal of Wind Engineering and Industrial Aerodynamics*, 41, pp.1883-1894

Tamboli, A., Joseph, L., Vadnere, U., and Xu, X., 2008. Tall Buildings: Sustainable Design Opportunities, In: Council on Tall Buildings and Urban Habitat, *CTBUH 8th World Conference,* Dubai, March 3-5

Tedesco, J.W. McDougal W.G. and Ross, C.A., 1999. *Structural Dynamics Theory and Applications*, 1st ed. Addison Wesley Longman Inc.

Viguie, R., and Kerschen, G., 2010. On the Functional Form of a Nonlinear Vibration Absorber, *Journal of Sound and Vibration*, 329(25), pp.5225-5232

Varoto, P.S., and de Oliveira, L.P.R., 2002. On the Force Drop Off Phenomenon in Shaker testing in Experimental Modal Analysis, *Shock and Vibration*, 9, pp. 165-175

APPENDIX A: Identification of System Parameters

To evaluate the optimal PTMD parameters for the SDOF structure model, the stiffness of the structure and damping coefficients for the structure and PTMD must be known. The selected values are based on the two-storey test structure. Note that the two floors are lumped into a single mass with an equivalent weight of 314.79 N. The pendulum mass has a weight of 14.41 N.

The estimated structural stiffness is determined by evaluating the damped natural frequency of the free response of the structure. The free response of the top floor, as represented in Figure A. 1, is measured by mounting accelerometers in orthogonal directions on the top floor of the structure and impacting the middle floor with a rubber mallet. The measured damped natural frequency is 1.855 Hz. The relationship between the damped natural frequency and the structural stiffness is shown in Eq. A-1. The resultant structural stiffness is 3713 N/m.

The structural damping ratio is evaluated by fitting an exponentially decaying curve with a decaying constant equal to the product of the natural frequency and damping ratio of the structure. The measured structural damping ratio is 0.024. Eq. A-2 is used to derive the damping coefficient. The calculated structural damping coefficient is 15.28 N/(m/s).

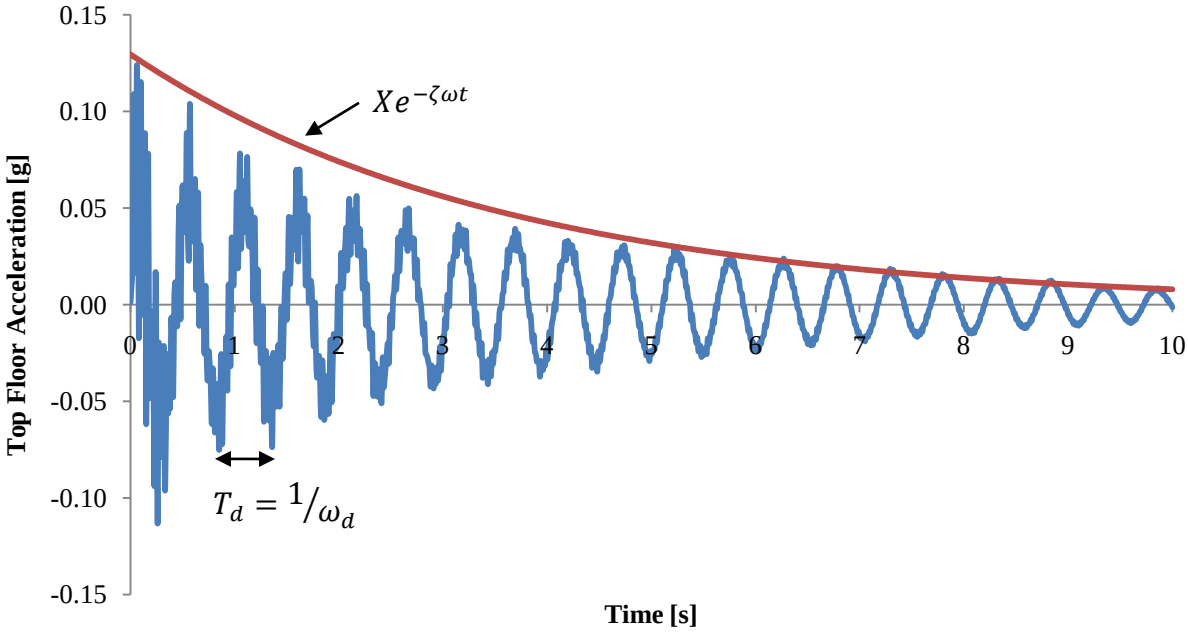

Figure A. 1: Free response of two storey structure

$$k = \frac{M\omega_d}{1-\xi^2} \tag{A- 1}$$

$$b = b_{cr}\xi = 2m\omega\xi \tag{A- 2}$$

The free response of the pendulum mass is used to evaluate the friction coefficient at the pendulum pivot. The free response is measured by displacing the pendulum mass and measuring its resultant motion with a laser displacement sensor. The free response is shown in Figure A. 2. By fitting an exponentially decaying curve and applying Eq. A-3, the resultant friction coefficient is 0.0072 Nms.

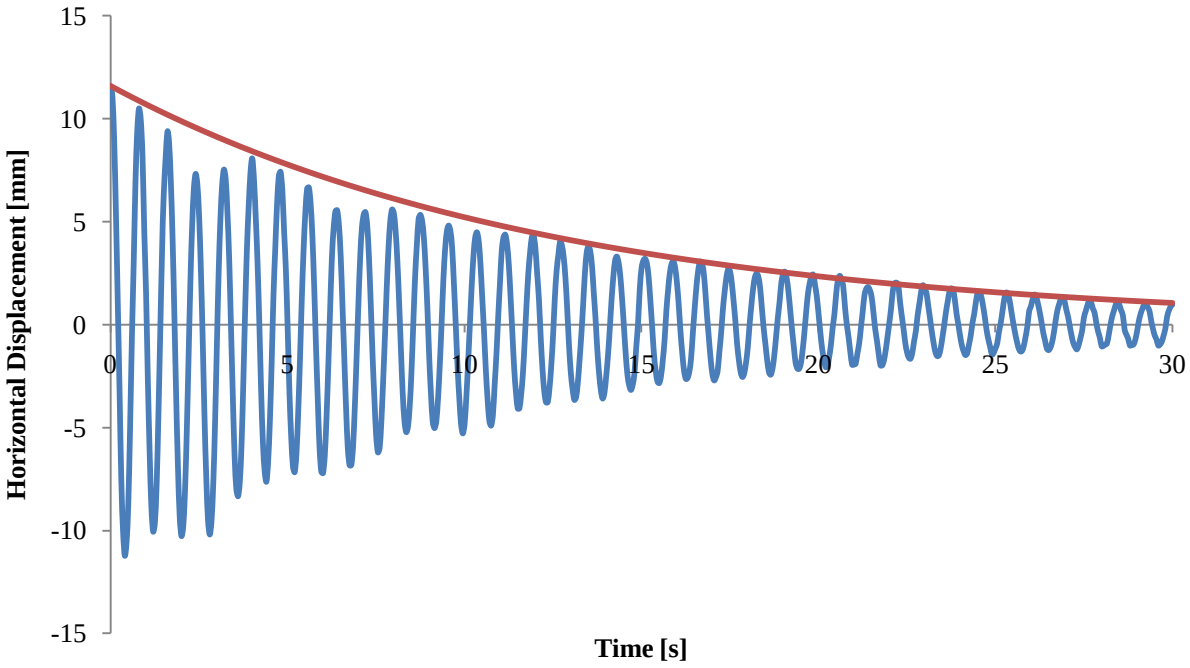

Figure A. 2: Free response of PTMD pendulum mass

$$\xi = \frac{\frac{c}{L}}{2m\sqrt{gL}} \tag{A- 3}$$

APPENDIX B: Optimization Algorithm

Optimization simulations were performed using MATLAB ver7.4.0 (R2007a). The optimization algorithm calculates the structural displacement amplification factor X for every possible combination of $\beta, \xi_d,$ and $\bar{m}$ within their respective range. The output is two $l \times k$ matrix, where l is the length of the value range for $\bar{m}$ and k is the length of the value range for ξ_d. The first matrix (represented by `temp`) contains the minimum peak X for the range of β values for each combination of $\xi_d,$ and $\bar{m}$. The second matrix (represented by `index_B`) contains the corresponding β value which results in the minimized peak. The optimized conditions is identified by the minimum peak value contained within `temp`.

```
clear all;
a = 0:0.001:3; %Range of values for structural excitation frequency ratio
E = 0.024; %Damping ratio of structure
m = 0:0.001:0.2; %Range of values for mass ratio
B = 0.75:0.001:1.25; %Range of values for tuned frequency ratio
Ed = 0:0.001:0.2;

temp = 1000*ones(length(m),length(Ed));
index_B = -1*ones(length(m),length(Ed));

for l = 1:length(m)
    for k = 1:length(Ed)
        for i = 1:length(B)
            for j = 1:length(a)
                %structure mass amplification factor calculation
                X(j)                    =                    sqrt((B(i)^2-
a(j)^2)^2+(2*Ed(k)*a(j)*B(i))^2)/sqrt((-B(i)^2*a(j)^2*m(l)+(1-
a(j)^2)*(B(i)^2-a(j)^2)-4*E*Ed(k)*B(i)*a(j)^2)^2+4*(E*a(j)*(B(i)^2-
a(j)^2)+Ed(k)*B(i)*a(j)*(1-a(j)^2*(1+m(l))))^2);
            end
            %determine if min peak for each combination of m and Ed
            if max(X(:)) <= temp(l,k)
                temp(l,k) = max(X(:));
                index_B(l,k) = B(i);
            end
        end
    end
end
```

APPENDIX C: Component Datasheets

Portescap 42M048C1B-Z36 Bipolar Stepper Motor Datasheet

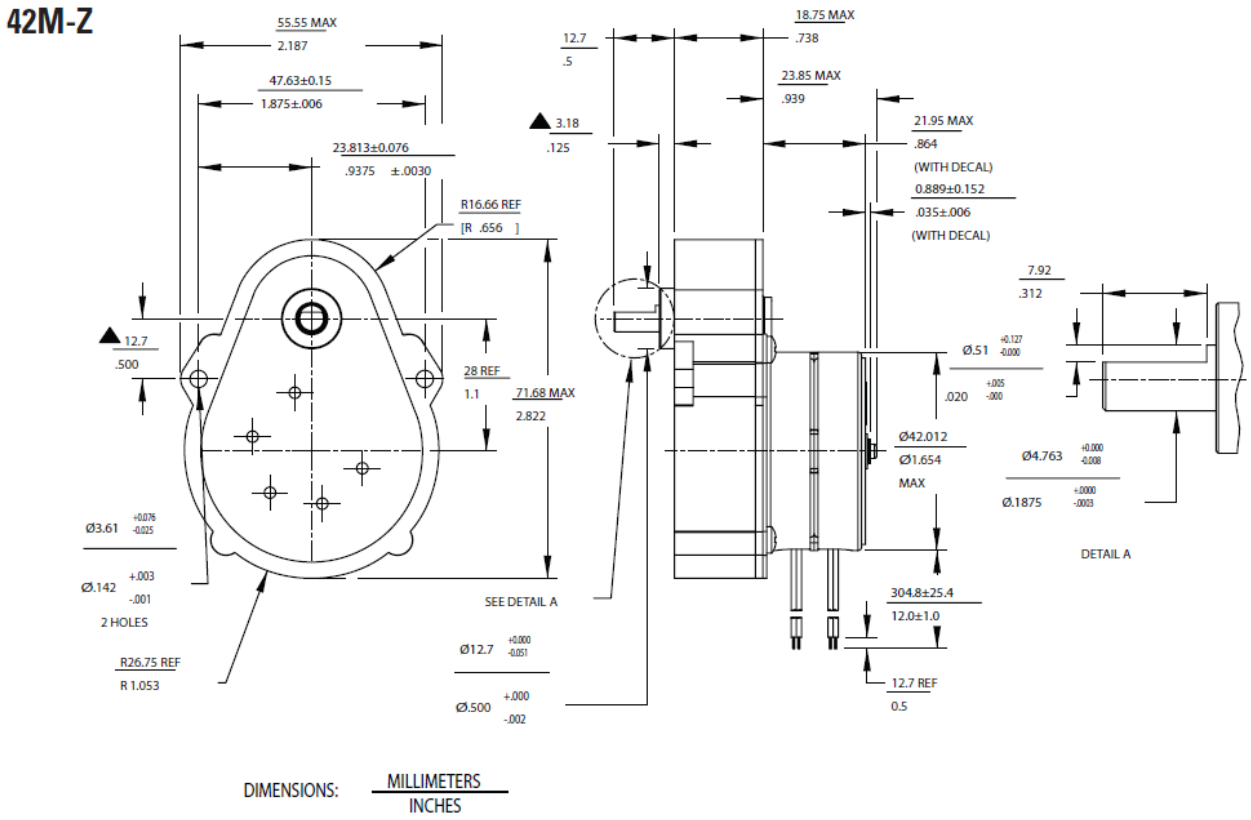

Figure C. 1: Portescap 42M048C1B-Z36 drawing

Rated voltage	5 vdc
Rated current per phase	0.55 A
Holding torque	84 mNm
Steps per revolution	48
Step angle	7.5 ± 0.5°

Table C. 1: Portescap 42M048C1B specifications

Gear ratio	50:1
Efficiency	65.0 %
Output step angle	0.15°
Output speed at 240 PPS	6 rpm
Running torque at 240 PPS	854 mNm

Table C. 2: Portescap 42M048C1B-Z36 geared specifications

Portescap 42M048C2B-R21 Bipolar Stepper Motor Datasheet

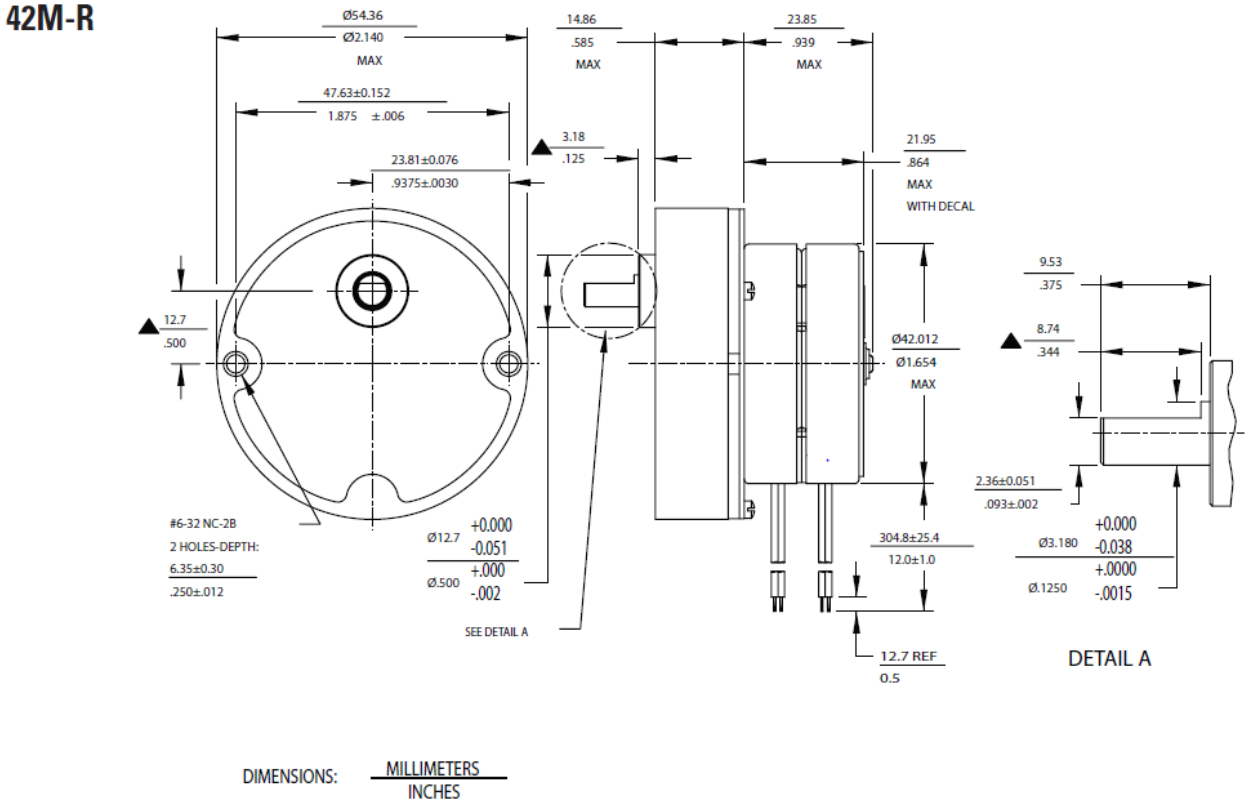

Figure C. 2: Portescap 42M048C2B-R21 drawing

Rated voltage	12 vdc
Rated current per phase	0.23 A
Holding torque	84 mNm
Steps per revolution	48
Step angle	7.5 ± 0.5°

Table C. 3: Portescap 42M048C2B specifications

Gear ratio	10:1
Efficiency	80.0 %
Output step angle	0.75°
Output speed at 240 PPS	30 rpm
Running torque at 240 PPS	211 mNm

Table C. 4: Portescap 42M048C2B-R21 geared specifications

Airpot 2K160 Dashpot Datasheet

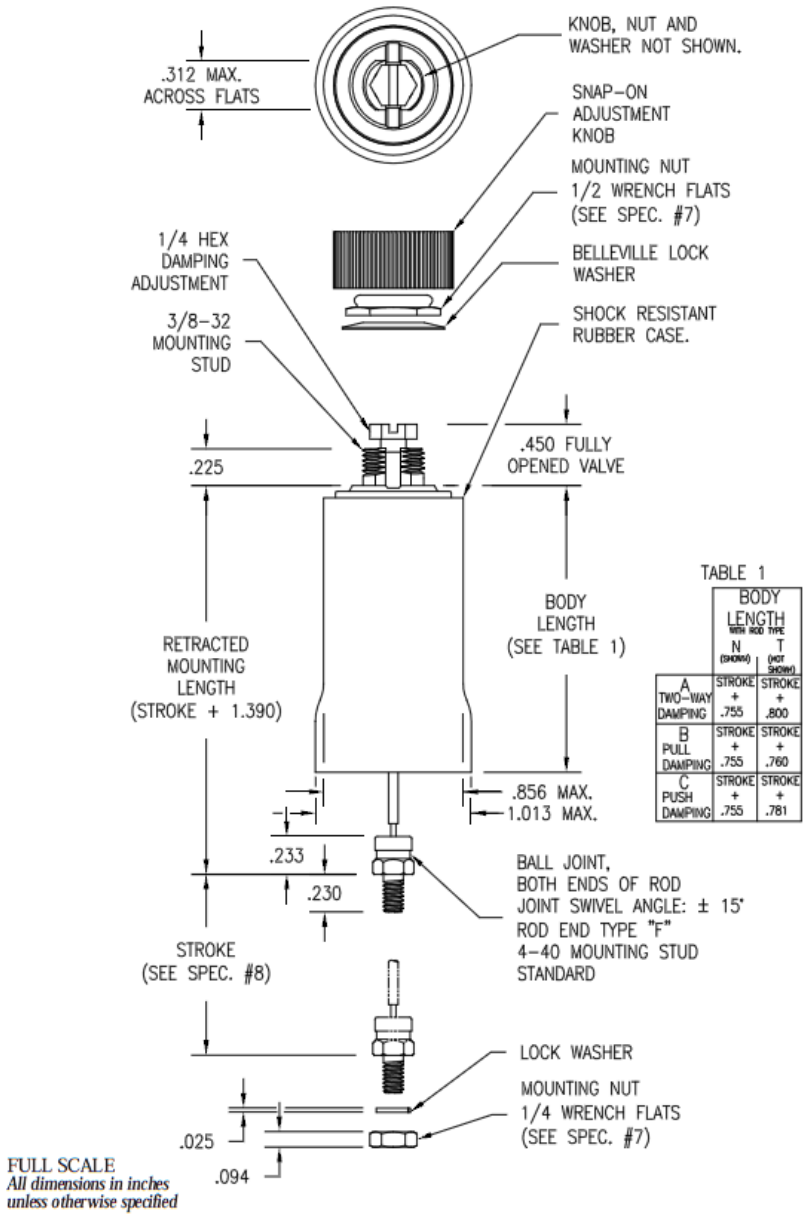

Figure C. 3: Airpot 2K160 dashpot drawing

Bore diameter	15.93 mm
Damping coefficient	0-1.75 N/(mm/s)
Pull damping force	18 N max
Push damping force	13 N max
Friction coefficient	0.2
Full stroke	3 in (7.62 cm)

Table C. 5: Airpot 2K160 specifications

Hoskin CP24MHT80 Laser Position Transducer

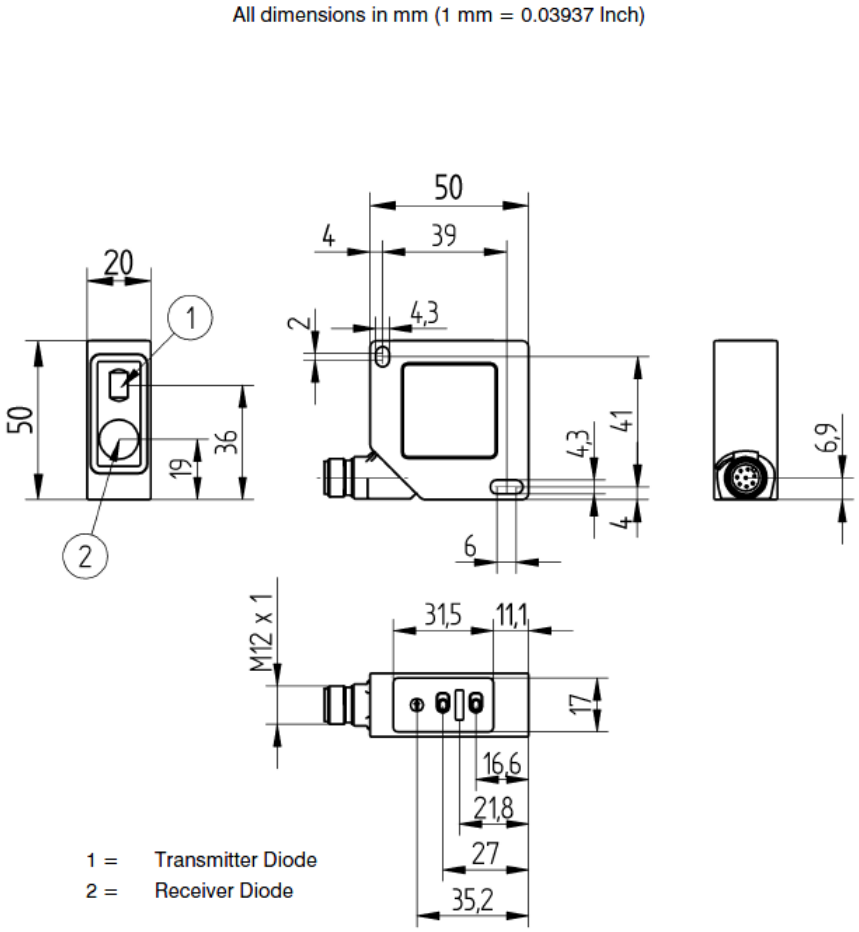

Figure C. 4: Hoskin CP24MHT80 drawing

Working range	40-160 mm
Linearity	0.1 %
Light source	Laser (red)
Wavelength	660 nm

Table C. 6: Hoskin CP24MHT80 optical specifications

Supply voltage	18-30 vdc
Current consumption	< 80 mA
Response time	0.66 ms
Cut-off frequency	750 Hz
Analog output	0-10 v
Full Stroke	3 in (7.62 cm)

Table C. 7: Hoskin CP24MHT80 electrical specifications

Micro-Epsilon WPS-150-MK30-P25 Draw Wire Sensor

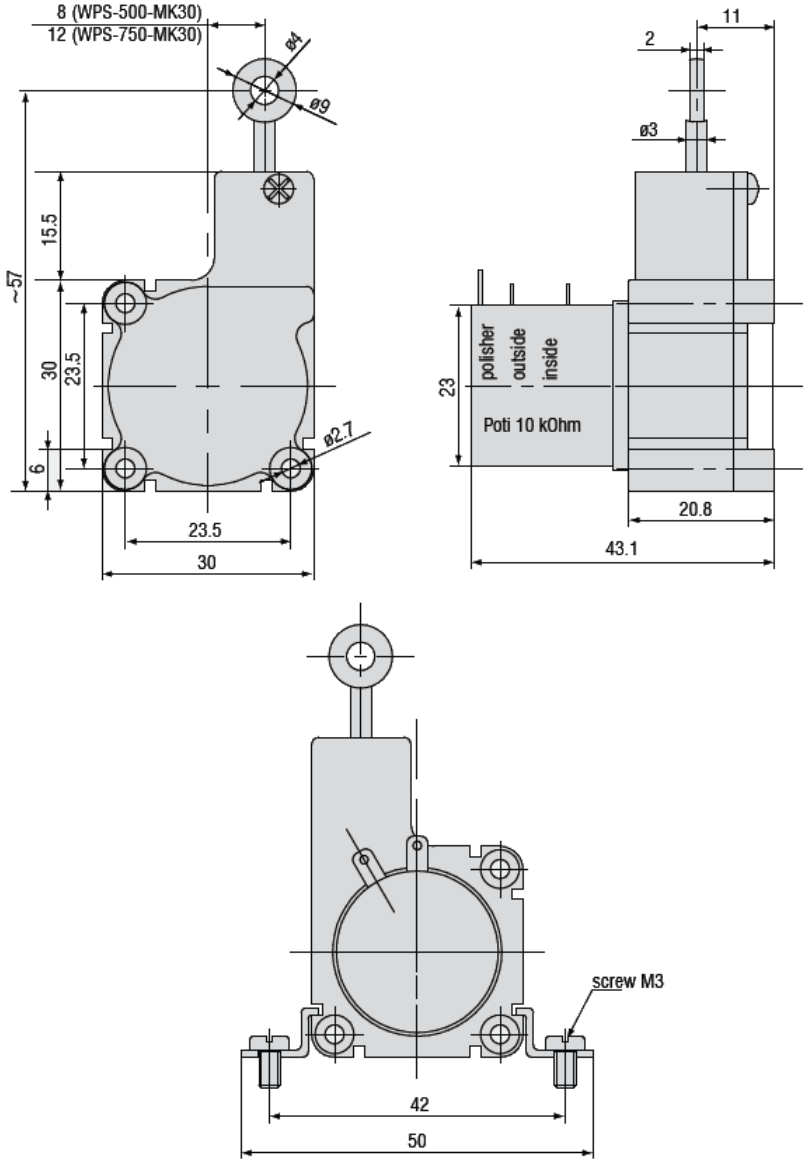

Figure C. 5: Micro-Epsilon MPS-150-MK30-P25 draw wire sensor drawing

Measurement range	150 mm
Resolution	0.1 mm
Linearity	±0.25% FSO
Wire retraction force	Approx. 1 N
Max Acceleration	5 g

Table C. 8: Micro-Epsilon MPS-150-MK30-P25 draw wire sensor specifications

Hamlin 55100 Mini Flange Mount Hall Effect Sensor

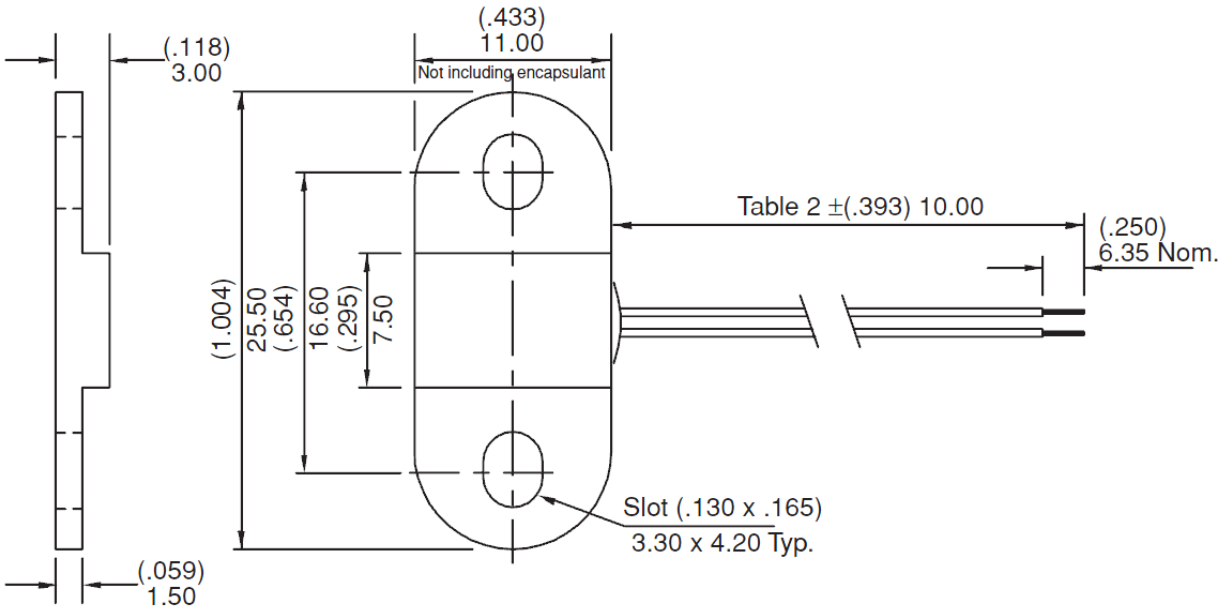

Figure C. 6: Hamlin 55100 Hall Effect sensor drawing

Supply Voltage	-15 to 28 vdc
Switching speed	10 kHz
Maximum vibration	50 g
Sensitivity Gauss (57)	18.5 mm

Table C. 9: Hamlin 55100 Hall Effect sensor specifications

Dytran 1050V1 Force Sensor

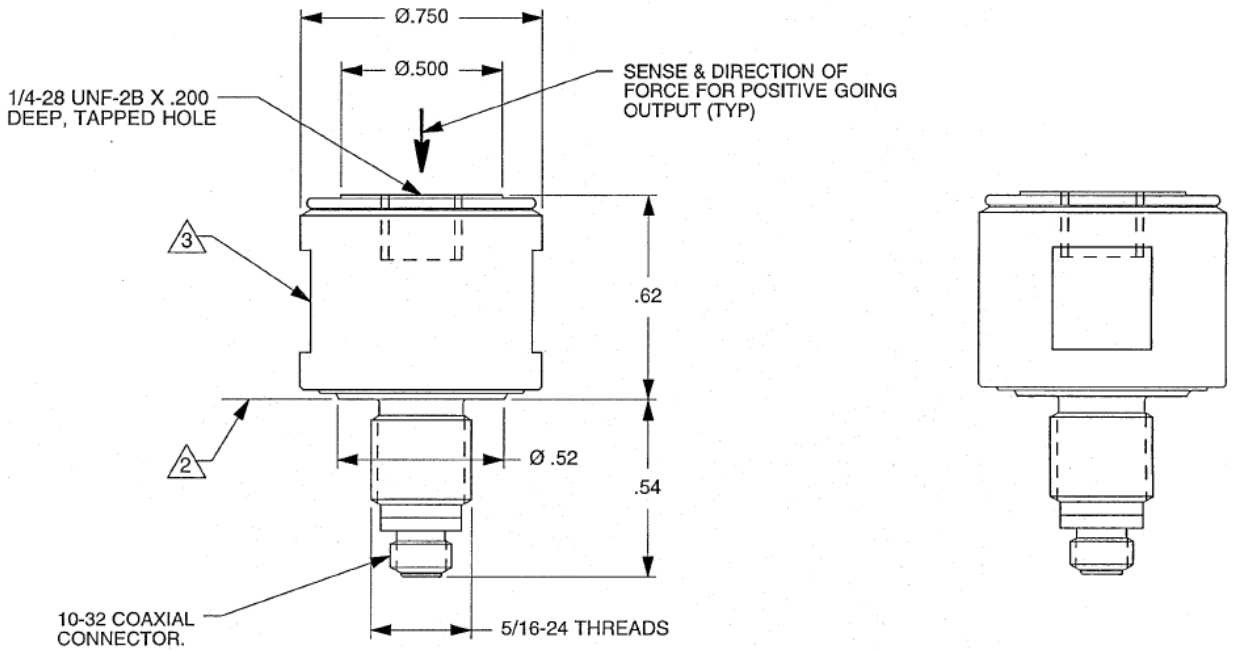

Figure C. 7: Dytran 1050V1 force sensor drawing

Sensitivity	463.8 mV/LbF
Compression range	0 to 10 LbF
Tension range	0 to 10 LbF
Linearity	± 1 % FS
FS output voltage (nom)	5 V
Maximum vibration	± 5000 g

Table C. 10: Dytran 1050V1 force sensor specifications

PCB Piezotronics 333B40 Accelerometer

Figure C. 8: PCB 333B40 accelerometer

Sensitivity (±10%)	500 mV/g
Measurement range	± 10 g pk
Frequency range	0.5 – 3000 Hz
Broadband resolution	0.00005 g rms
Non-linearity	≤ 1 %

Table C. 11: PCB 333B40 accelerometer performance specifications

Overload limit	± 5000 g pk
Temperature range	-18 to 66°C

Table C. 12: PCB 333B40 accelerometer environmental specifications

Excitation voltage	18 - 30 vdc
Constant current excitation	2 to 20 mA
Discharge Time Constant	1.0 to 2.5 sec

Table C. 13: PCB 333B40 accelerometer electrical specifications

APS 113-AB Shaker

Figure C. 9: APS 113-AB

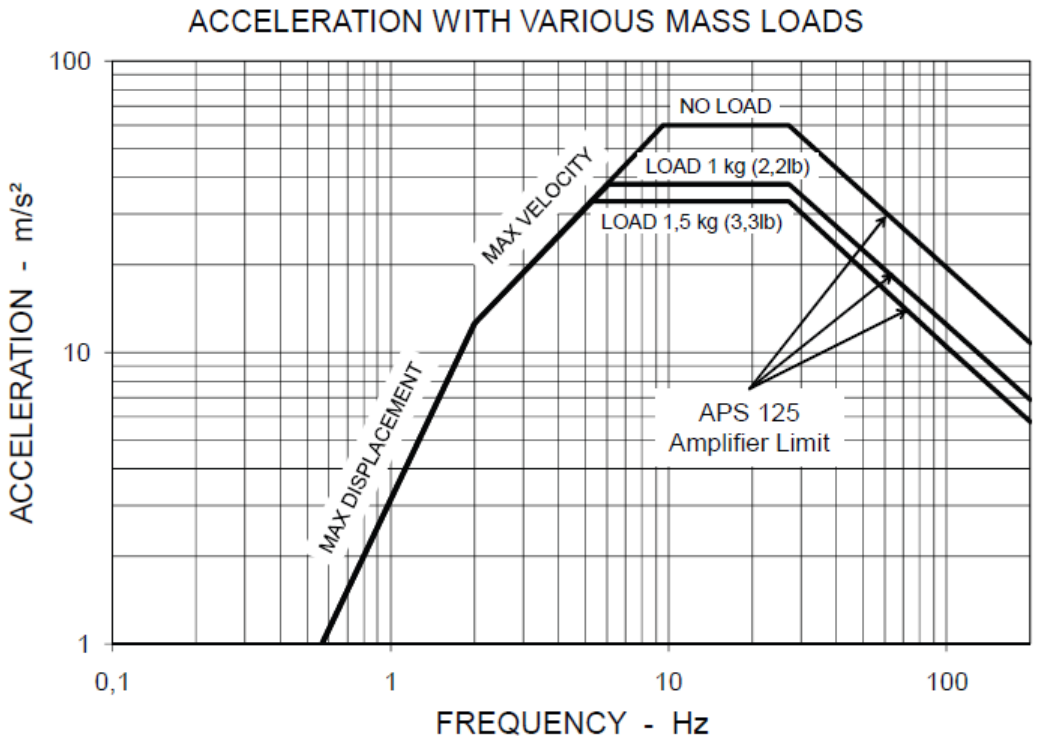

Figure C. 10: APS 113-AB Performance

Force (sine peak)	133 N
Stroke (peak – peak)	158 mm
Frequency range	0 to 200 Hz
Armature weight	2.7 kg
Shaker weight	36 kg

Table C. 14: APS 113-AB specifications

APPENDIX D: Experiment Drawings and Images

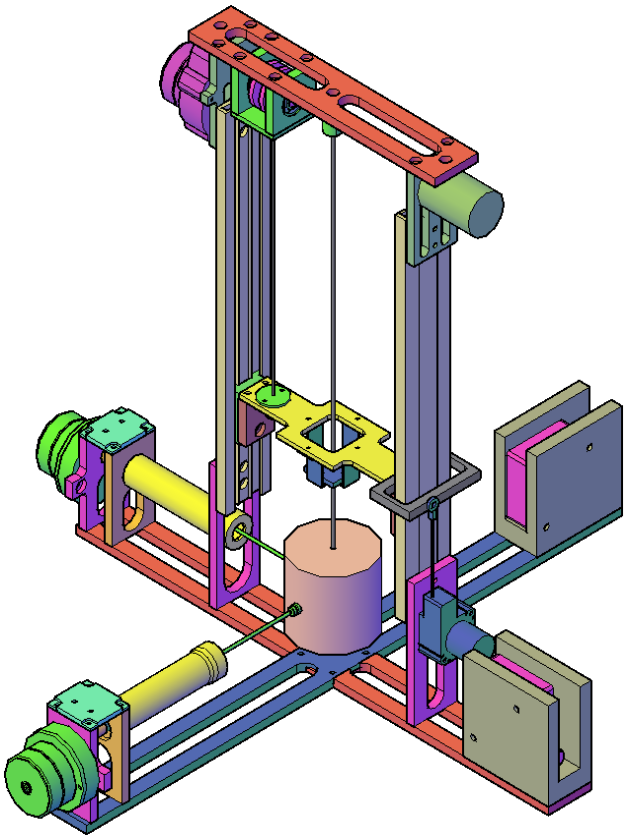

Figure D. 1: Isometric perspective of prototype APTMD

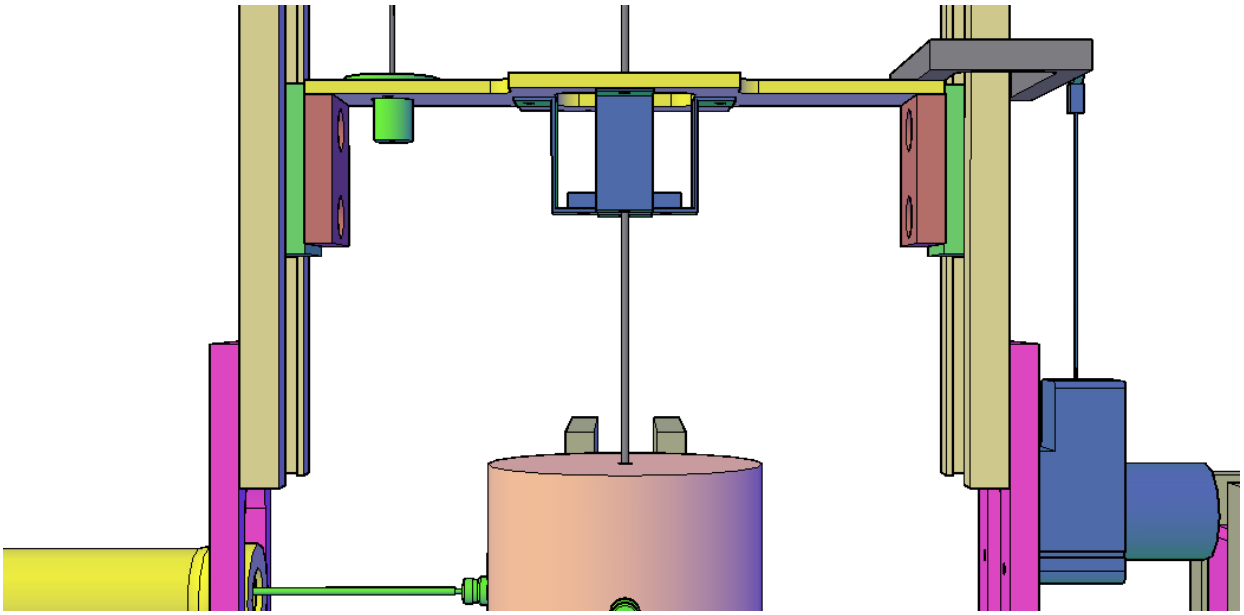

Figure D. 2: Tuning frame of prototype APTMD

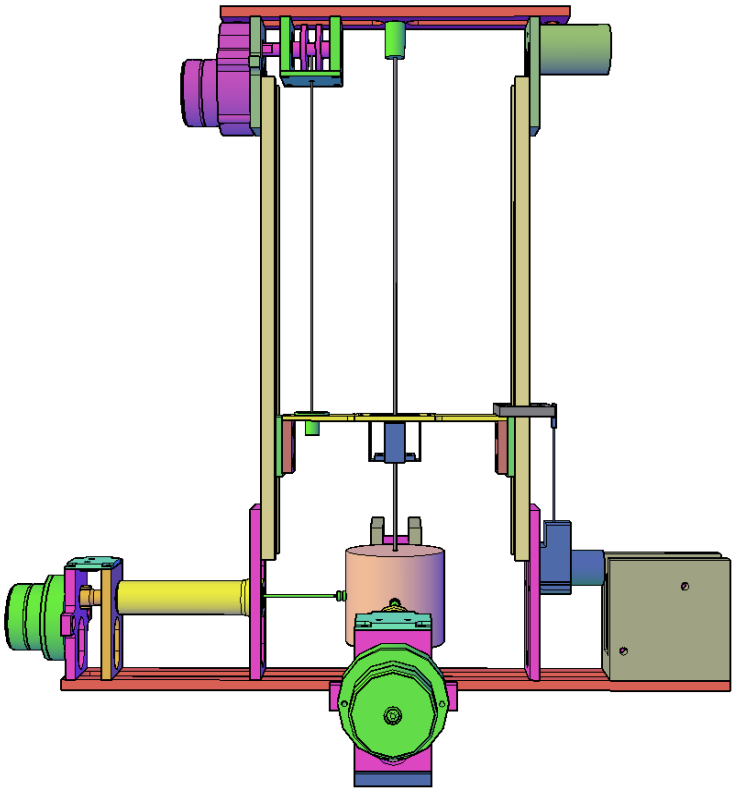

Figure D. 3: Side perspective of prototype APTMD

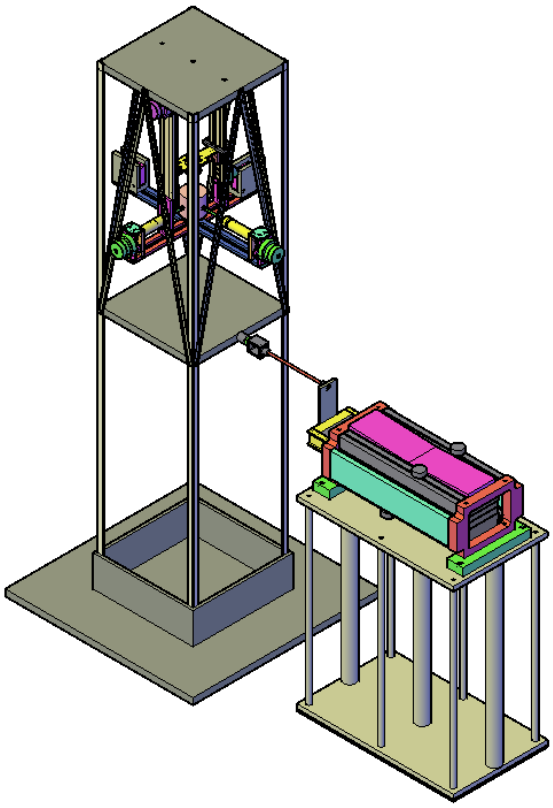

Figure D. 4: Isometric perspective of prototype APTMD mounted to test structure

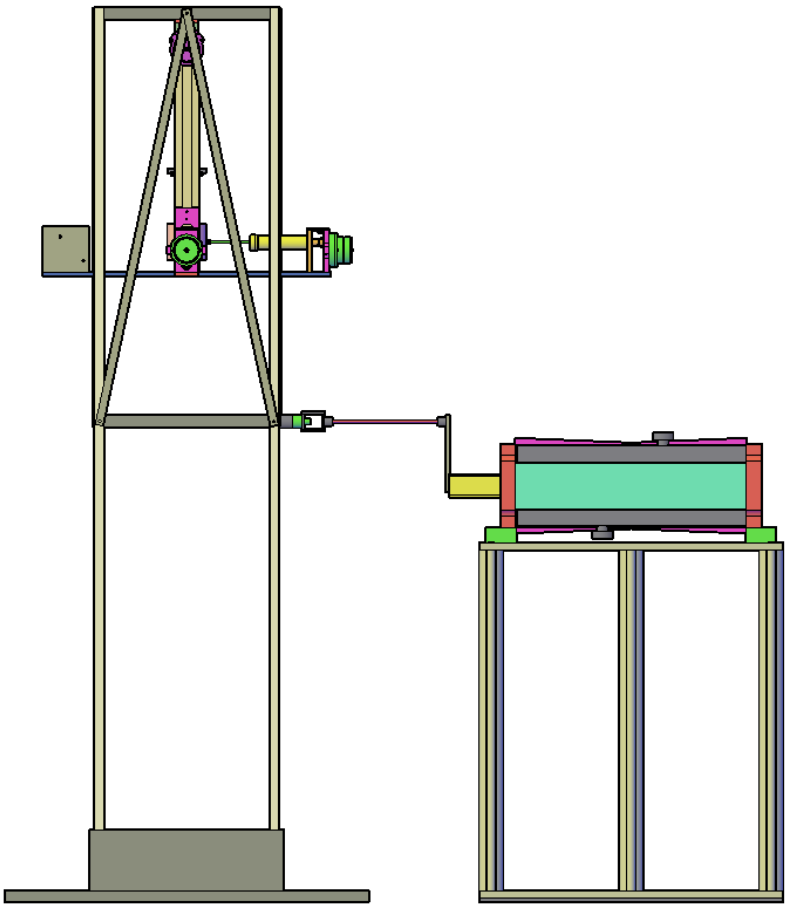

Figure D. 5: Side perspective prototype of APTMD mounted to test structure

APPENDIX E: Experiment Images

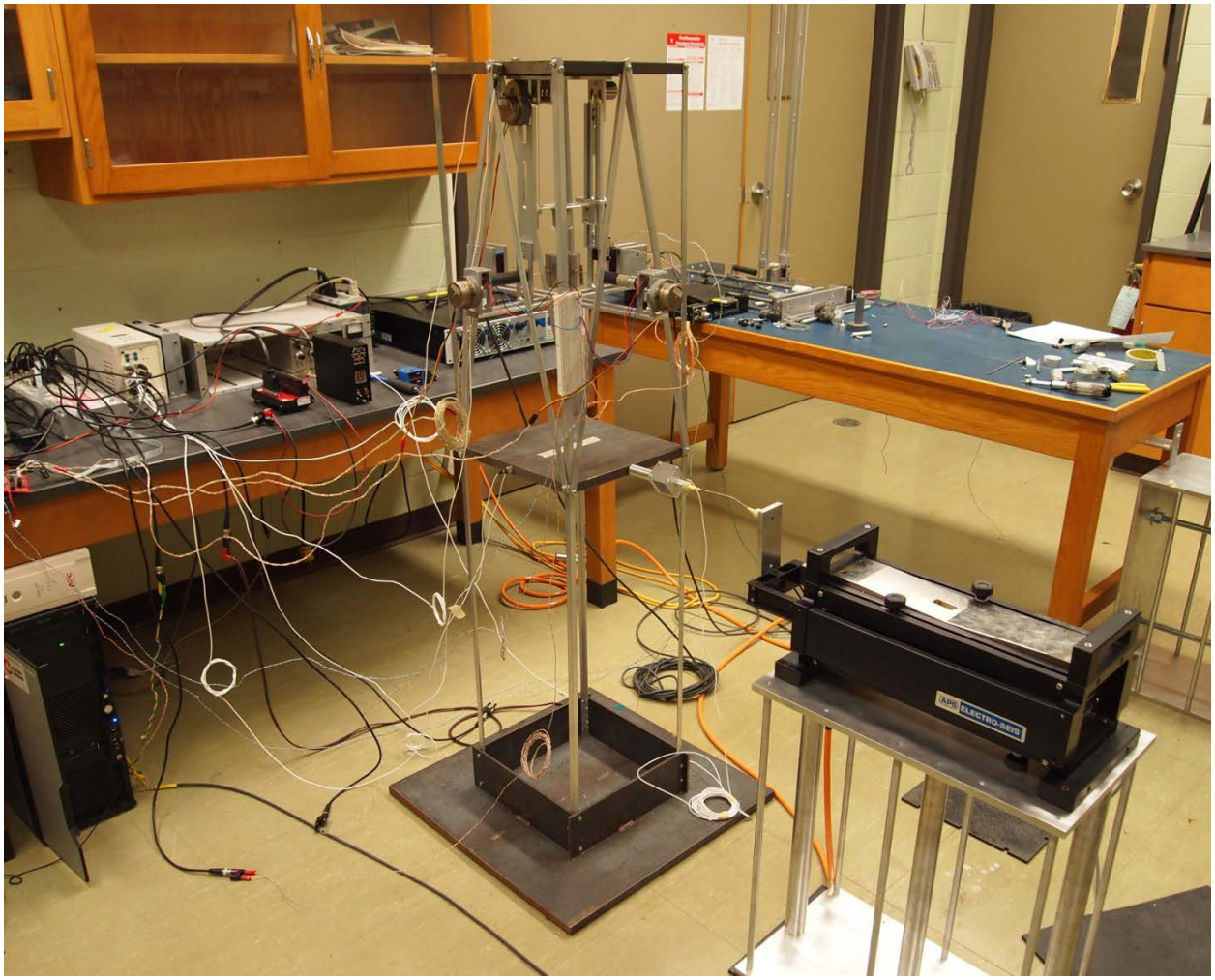

Figure E. 1: Experiment setup

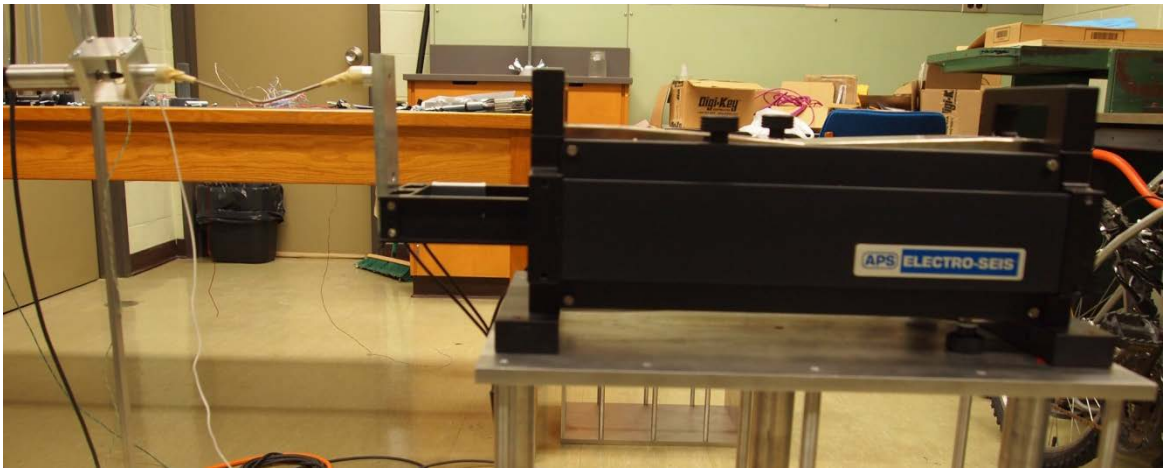

Figure E. 2: Shaker

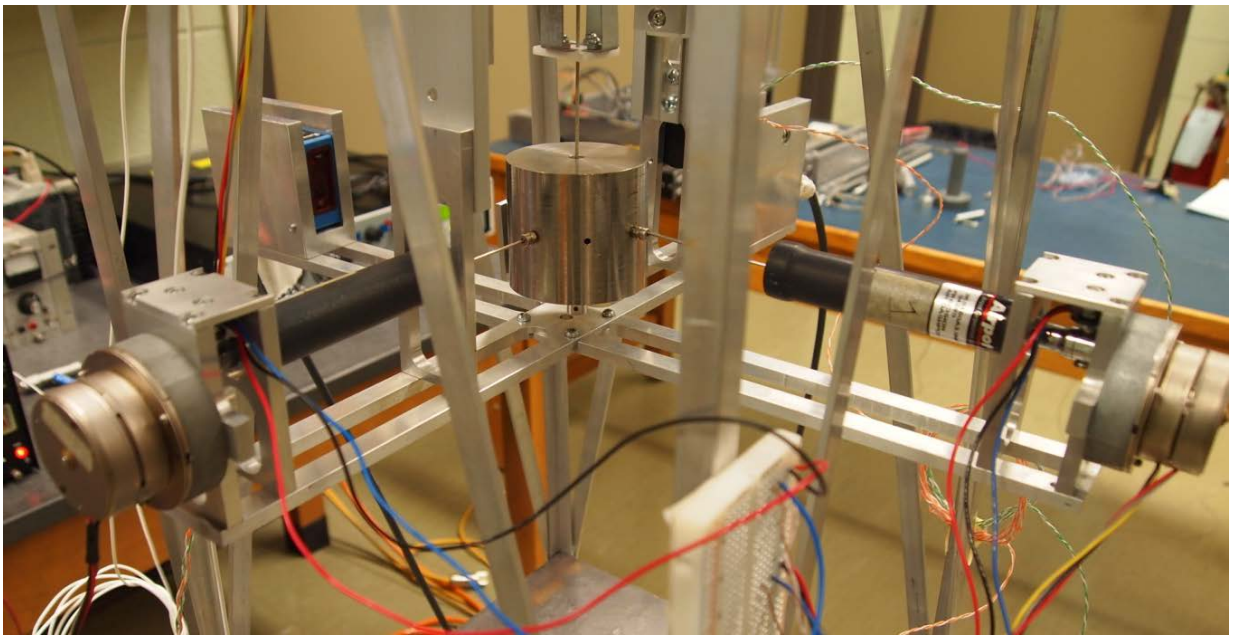

Figure E. 3: Damping assembly

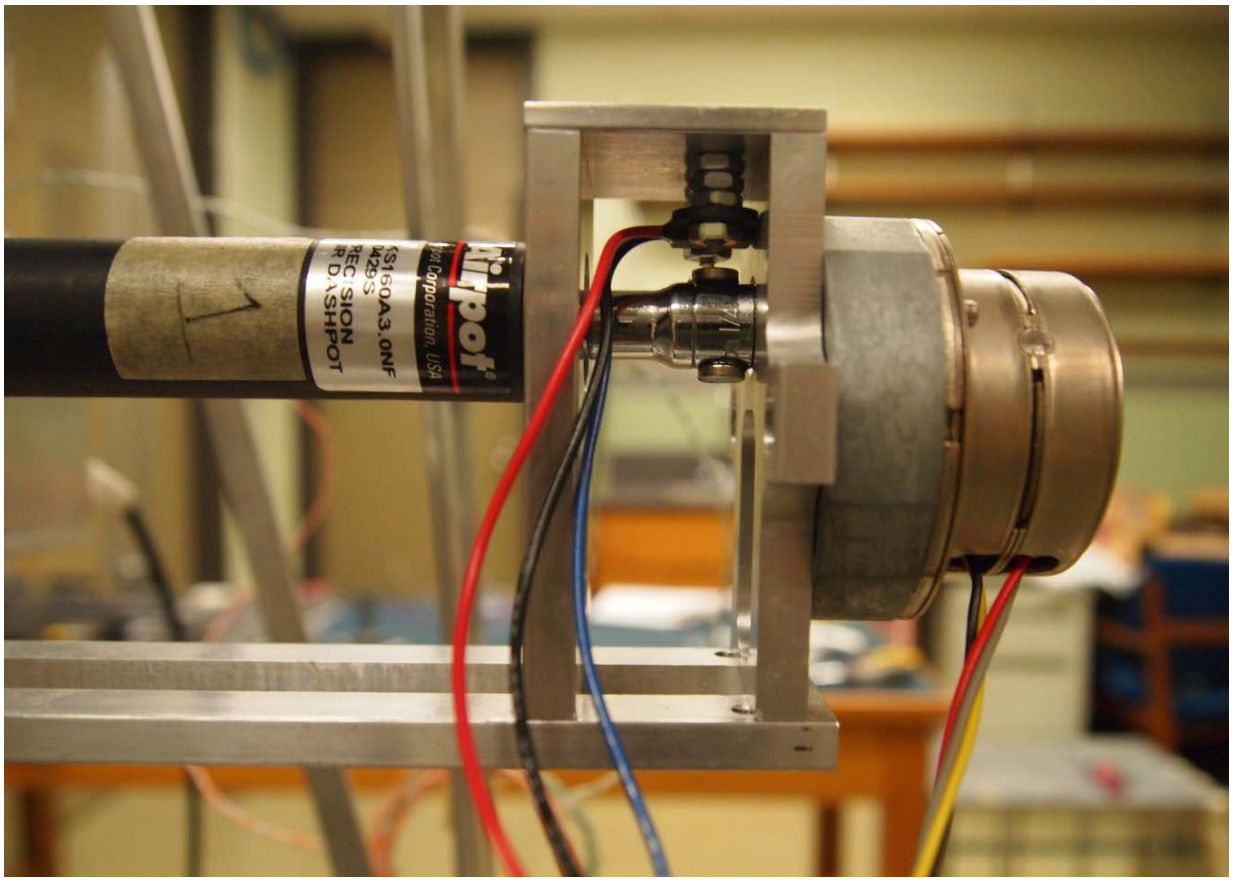

Figure E. 4: Damping control

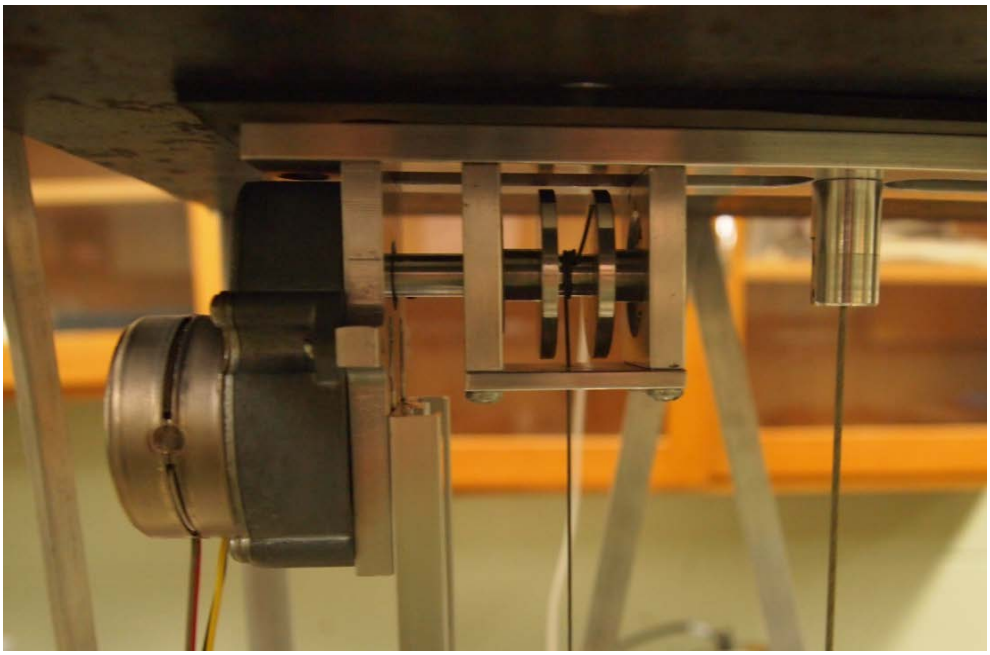

Figure E. 5: Cable winch and stepper motor

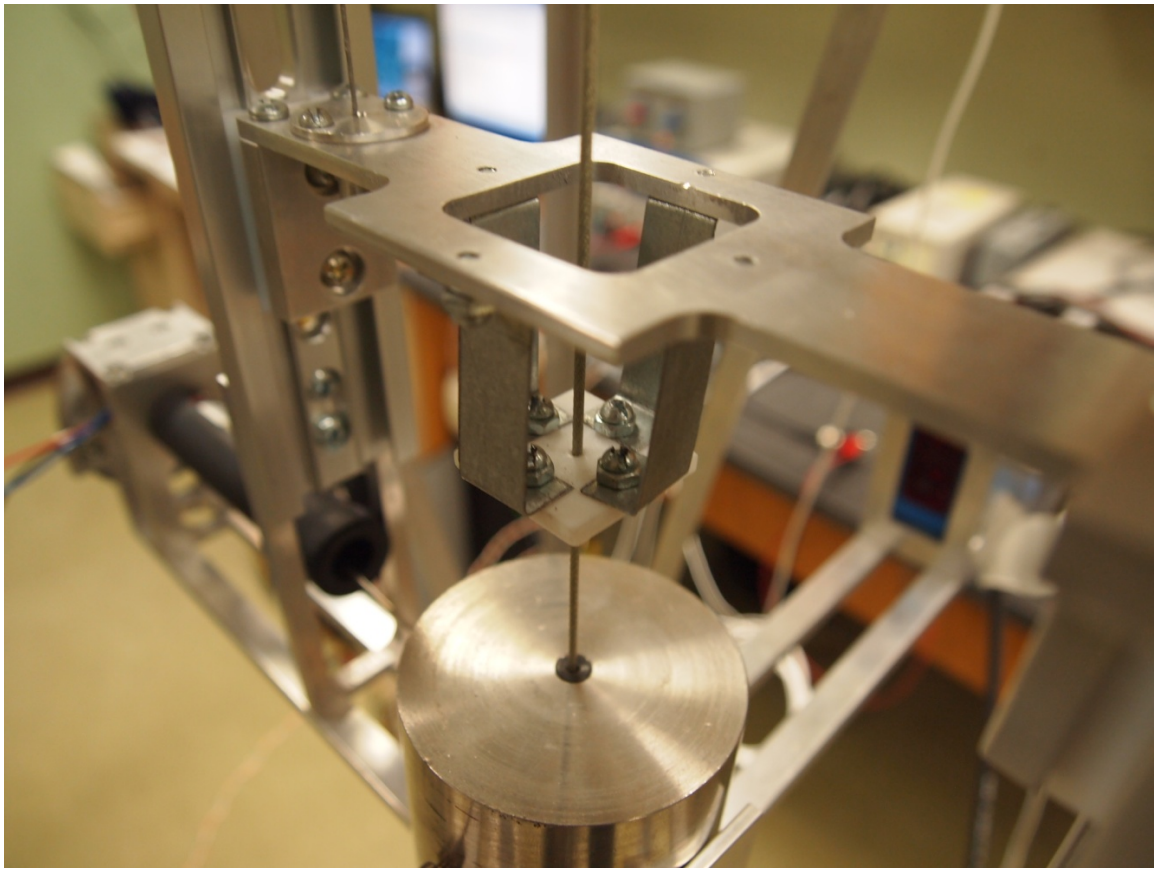

Figure E. 6: Tuning assembly

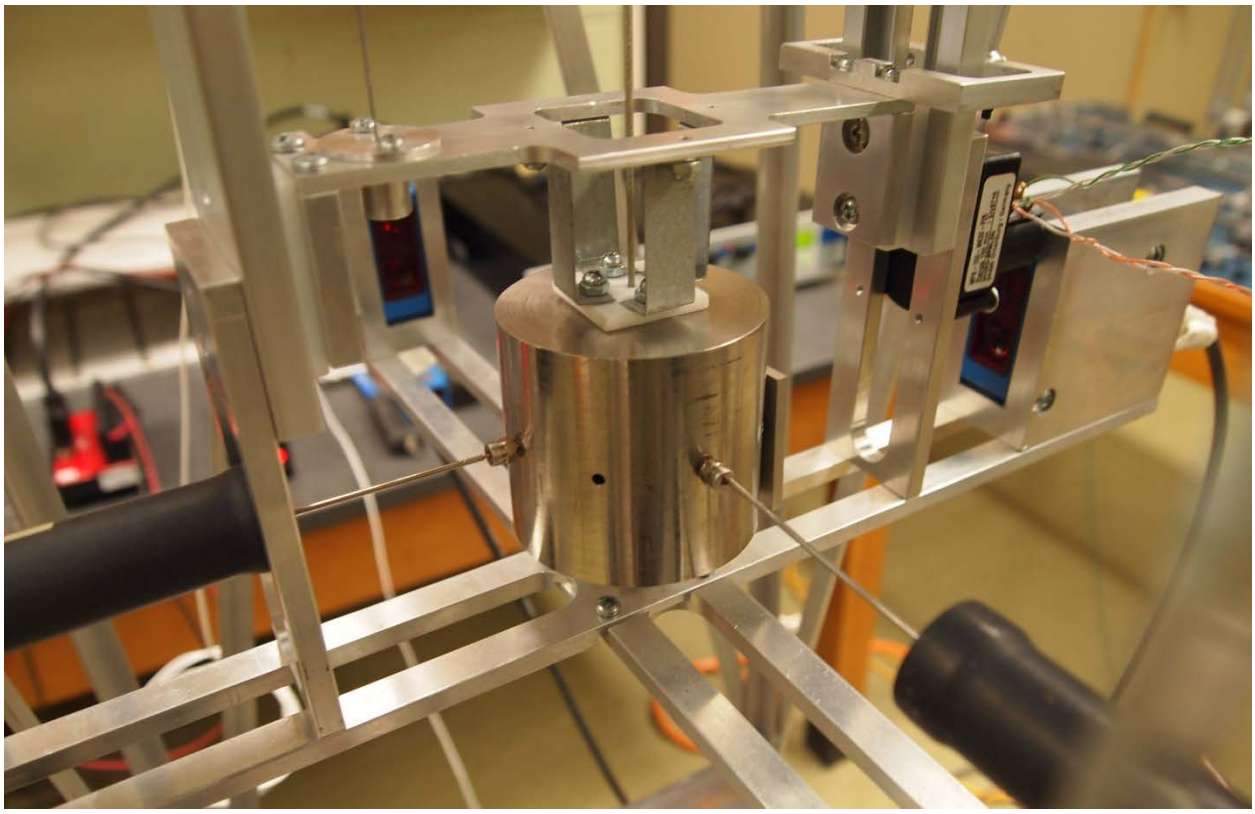

Figure E. 7: Pendulum mass at detuned position

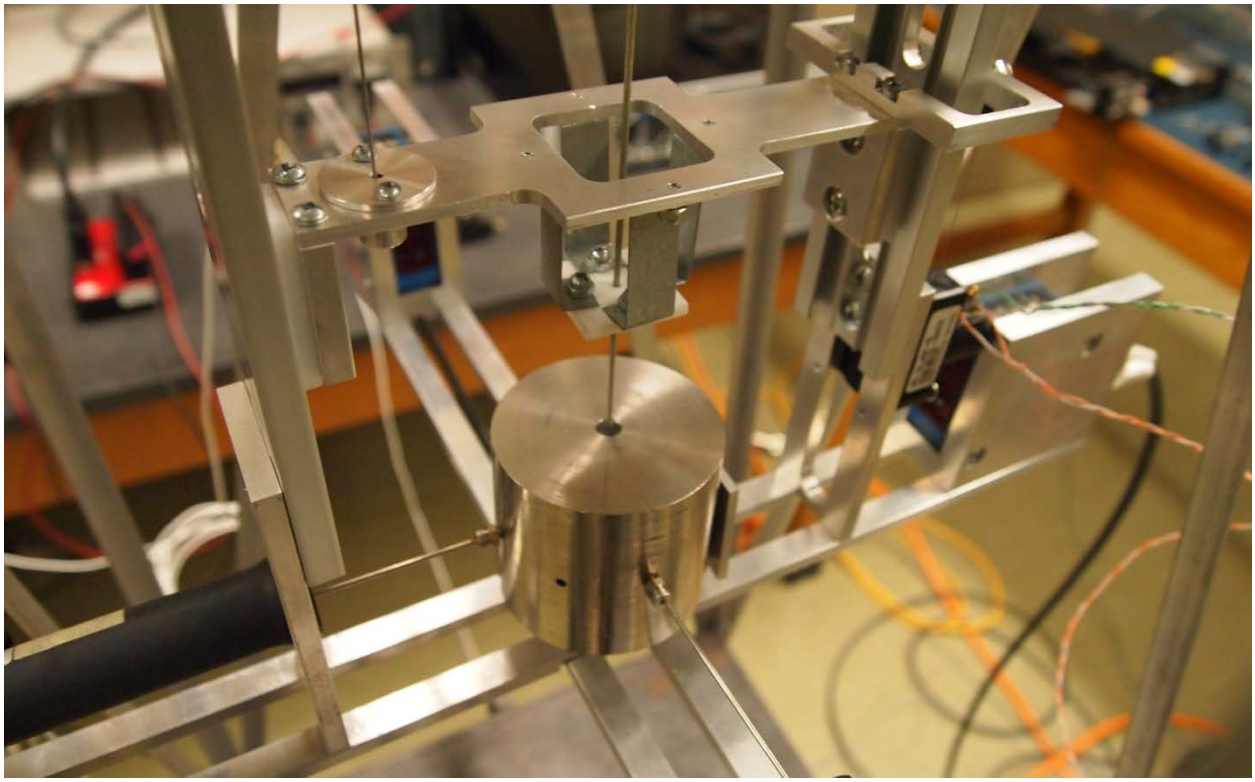

Figure E. 8: Pendulum mass at tuned position

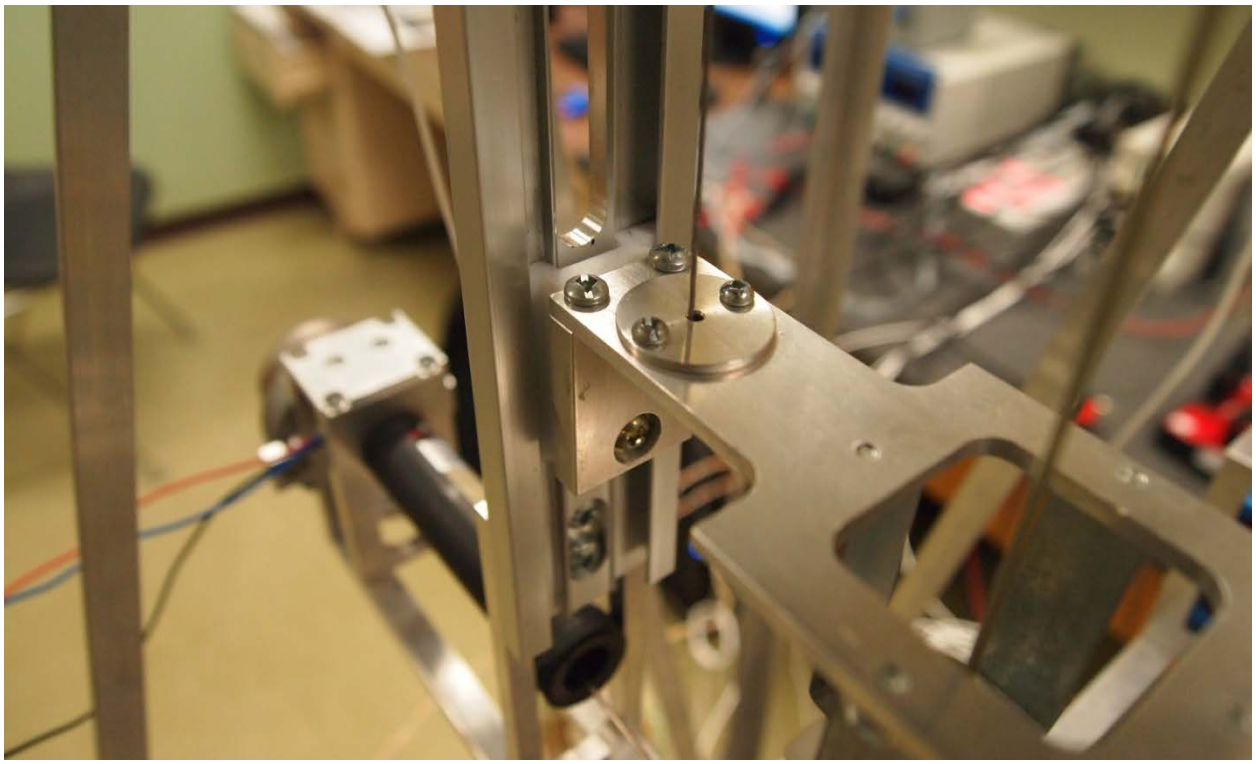

Figure E. 9: Low friction rail and guide block

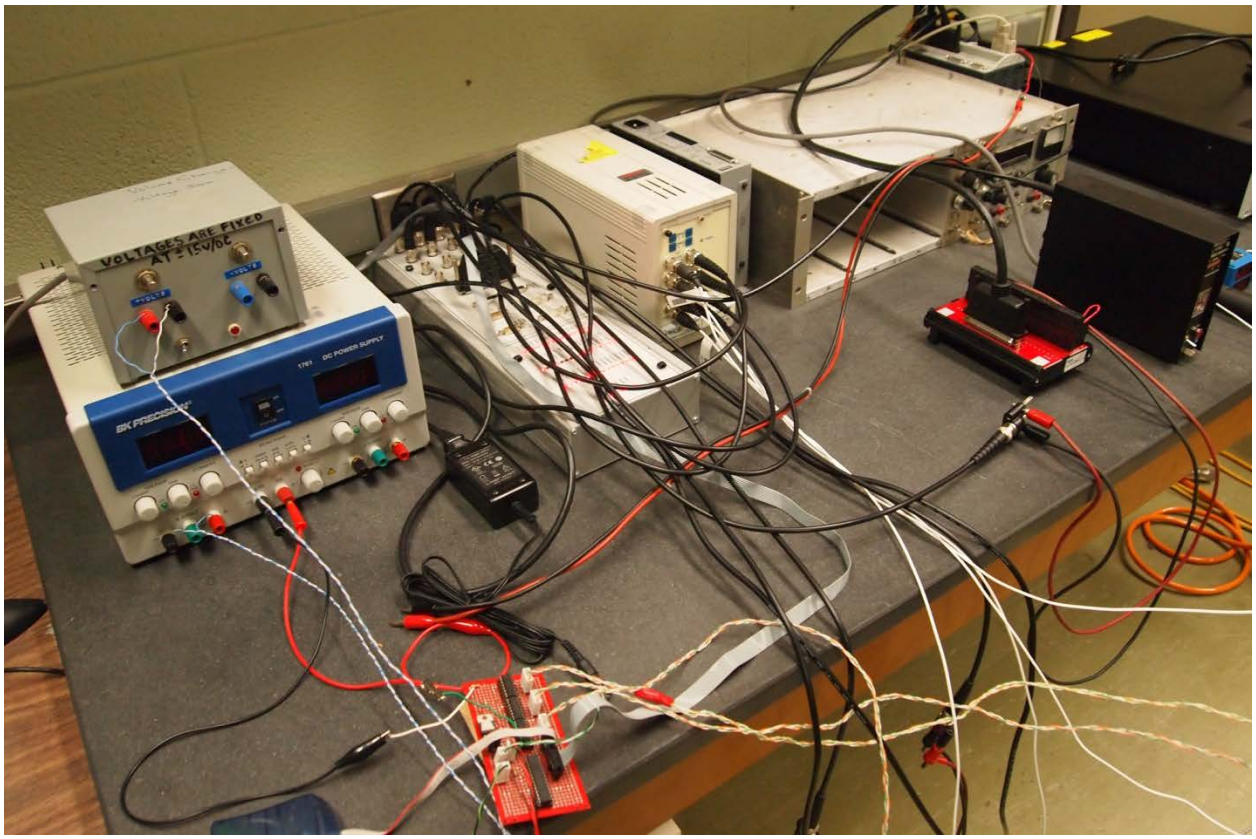

Figure E. 10: Experiment hardware

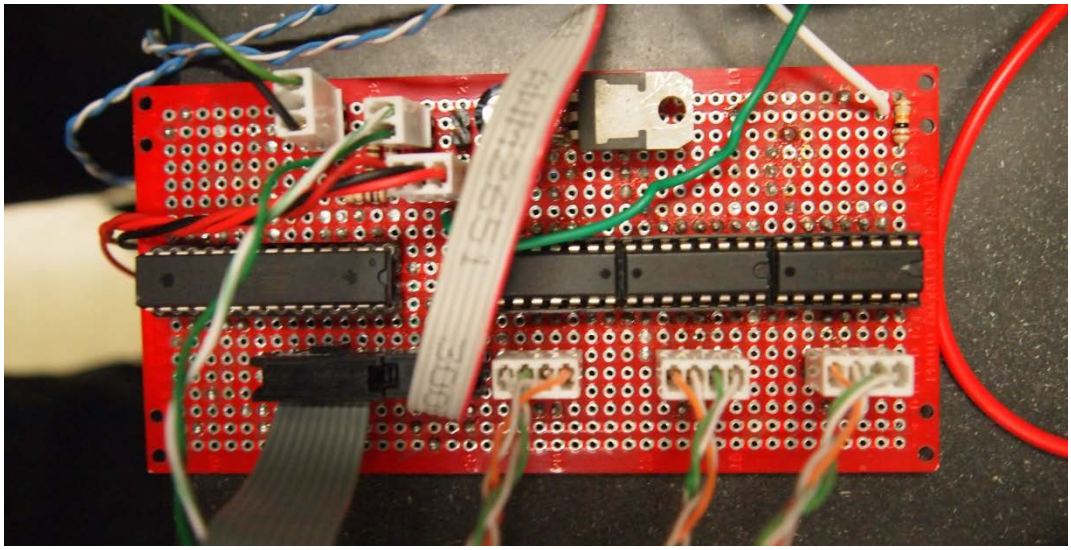

Figure E. 11: Stepper motor controller

Figure E. 12: Stinger assembly

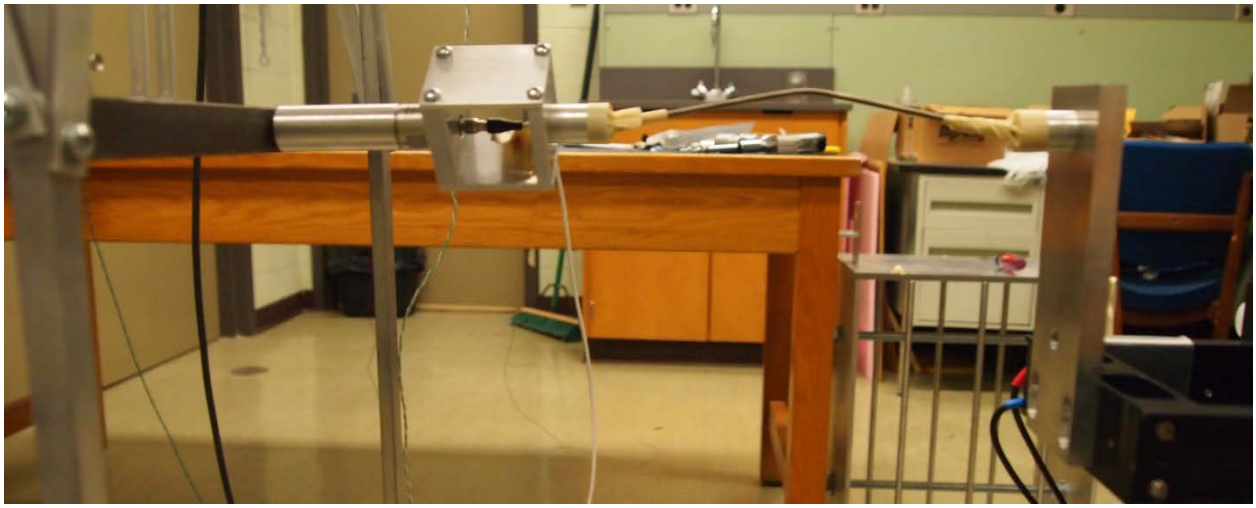

Figure E. 13: Stinger assembly after excessive load

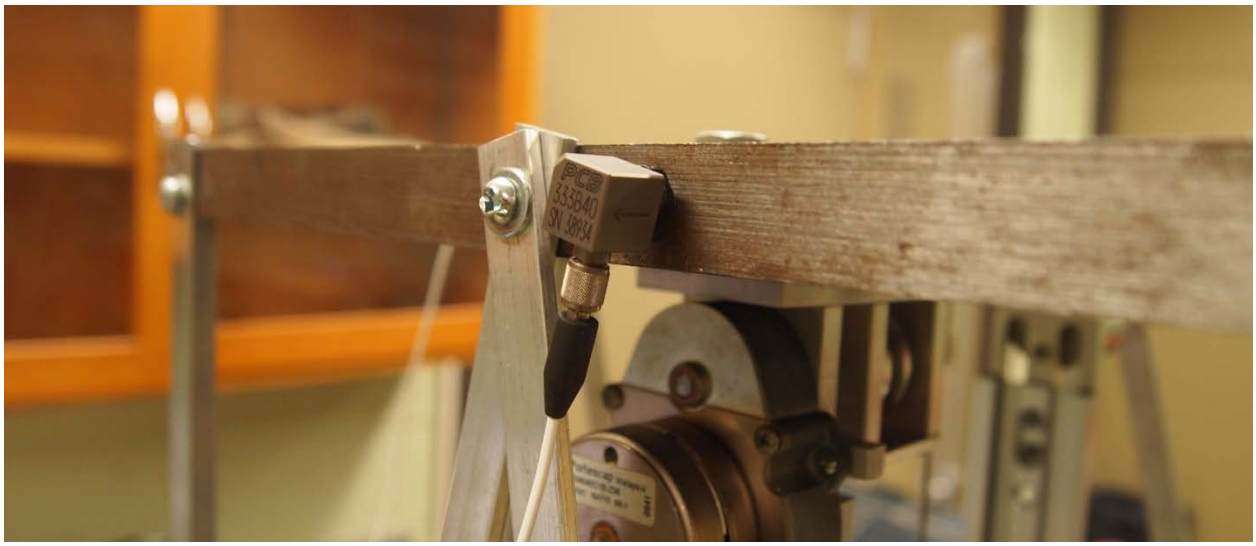

Figure E. 14: Structure accelerometers

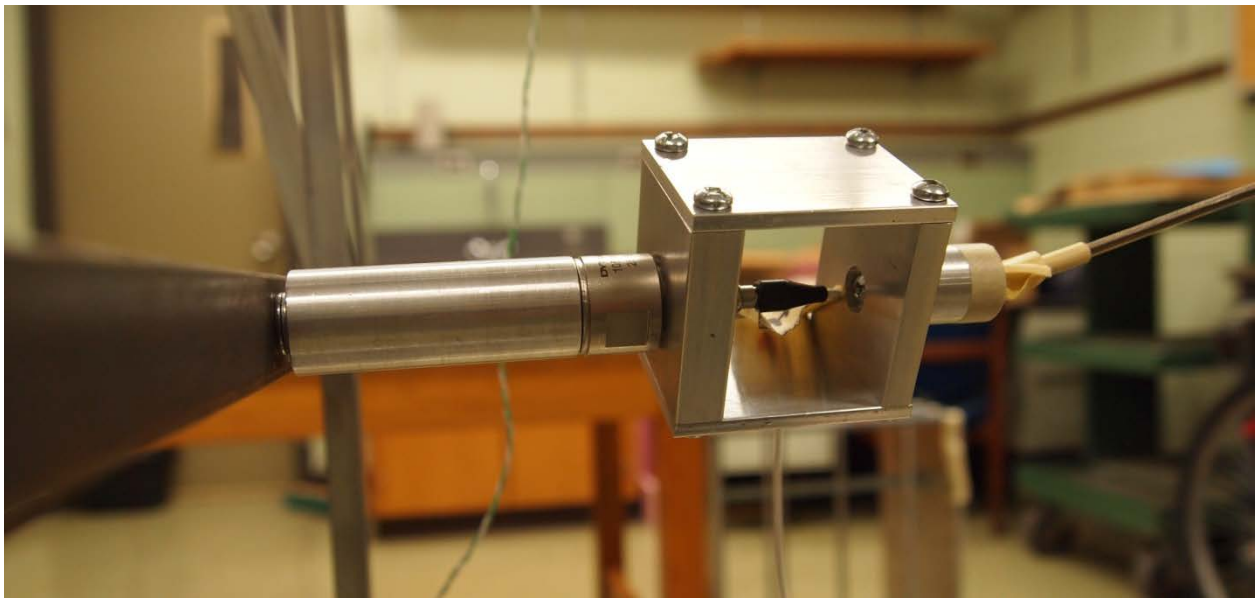

Figure E. 15: Force transducer

APPENDIX F: Peak Frequency Identification

The peak frequency identification algorithm accepts a 2048 point symmetric periodogram estimation for frequencies ranging from 0 Hz to 100 Hz. The output of the algorithm is the three lowest modal frequencies and their respective amplitudes.

```
%this function determines the mimimum peak frequency
function    [min_freq,mag_min_freq,freq2,mag2,freq3,mag3,mean_fft]        =
find_frequency(data,excitation)

nFFT = 2048; %number of points in the fast fourier transform
Fs = 100; %sampling rate of data
freq = Fs/nFFT*(0:nFFT-1); %frequency vector

seg_size = 4; %size of segment in 1/Hz(T)
L = uint32(length(freq)); %total number of data points within data and
frequency vector
max_freq = freq(L); %highest frequency
N = idivide(L,max_freq*seg_size,'floor'); %number of data points within
segment frequency

Freq = zeros(1,Fs*seg_size*N);
Data = zeros(1,Fs*seg_size*N);
%remove the first 0.5Hz of data since the accelerometers are unable to read
below 0.5Hz
%freq and data vectors contain Fs*segment_size segments (200)
Freq = freq(1,seg_size/2*N+2:Fs*seg_size*N+seg_size/2*N+1);
Data = data(1,seg_size/2*N+2:Fs*seg_size*N+seg_size/2*N+1);

threshold = zeros(1,Fs*seg_size); %threshold value is used to determine the
existance of a relative maxima within each segment
max_mag = zeros(1,Fs*seg_size); %vector holds the maximum magnitude within
each segment, default set to threshold value
pos = ones(1,Fs*seg_size); %vector holds integer value representing
position of local maxima within data vector (FFT vector)
peak = zeros(Fs*seg_size,2);

weighting = 0.75;
start = seg_size/2*N+2;
stop = Fs*seg_size*N+seg_size/2*N+1;
mData = mean(data(start:stop));
%create threshold vector, threshold is average over 2 segments
for i = 1:(Fs*seg_size-1)
    temp = 0;
    for j = start+(i-1)*N:start+(i+1)*N-1
        temp = temp + data(j);
    end
    threshold(1,i) = mData + abs(temp/(2*N))*weighting;
end
```

```
temp = 0;
for j = start+(Fs*seg_size-1)*N:start+Fs*seg_size*N-1
    temp = temp + data(j);
end
threshold(1,Fs*seg_size) =mData+abs(temp/N)*weighting;

max_mag = threshold;

%determine local maxima for each segment
for i=1:(Fs*seg_size)
    for j = 1:N
        if data(start-1+(i-1)*N+j)>max_mag(i)
            pos(i)=start-1+(i-1)*N+j;
            max_mag(i)=Data(start-1+(i-1)*N+j);
        end
    end
end

%algorithm determines local maxima
%index local maximas by frequencies, resultant matrix peak contains the
%peaks in order from lowest frequency to highest frequency and their
respective magnitude

index = 1;
if max_mag(1)>threshold(1,1)&& max_mag(1)>max_mag(2)
    peak(index,1) = max_mag(1);
    peak(index,2) = freq(1,pos(1));
    index = index + 1;
end

for i = 2:(Fs*seg_size-1)
    if        max_mag(i)>threshold(1,i)&&        max_mag(i)>max_mag(i+1)&&
max_mag(i)>max_mag(i-1)
        peak(index,1) = max_mag(i);
        peak(index,2) = freq(pos(i));
        index = index + 1;
    end
end

min_freq = peak(1,2);
mag_min_freq = peak(1,1);
freq2 = peak(2,2);
mag2 = peak(2,1);
freq3 = peak(3,2);
mag3 = peak(3,1);
mean_fft = mData;
```